https://doi.org/10.15388/vu.thesis.976
https://orcid.org/0000-0001-9412-9240

VILNIUS UNIVERSITY
CENTER FOR PHYSICAL SCIENCES AND TECHNOLOGY

Ignas Bitinaitis

Magnetron Sputtered Metal - Dielectric Optical Coatings for Sensing and Space Applications

DOCTORAL DISSERTATION

Technological Sciences,
Material Engineering (T 008)

VILNIUS 2026

The dissertation was prepared between 2021 and 2025 at Center For Physical Sciences and Technology. The research was supported by Research Council of Lithuania.

Academic Supervisor – Dr. Alexandr Belosludtsev (Center for Physical Sciences and Technology, Technological Sciences, Material engineering – T 008).

This doctoral dissertation will be defended in a public meeting of the Dissertation Defence Panel:

Chairman – Dr. Gediminas Račiukaitis (Center for Physical Sciences and Technology, Technological Sciences, Material Engineering – T 008).
Members:
Asoc. Prof. Dr. Renata Butkutė (Center for Physical Sciences and Technology, Technological Sciences, Material Engineering – T 008),
Prof. Dr. Giedrius Laukaitis (Kaunas University of Technology, Natural Sciences, Physics – N 002),
Prof. Dr. Juris Purāns (University of Latvia, Technological Sciences, Material Engineering – T 008).
Asoc. Prof. Dr. Tomas Šalkus (Vilnius University, Technological Sciences, Material Engineering – T 008)

The dissertation shall be defended at a public meeting of the Dissertation Defence Panel at 13:00 on 8 September 2026 in conference room A140 (Savanorių ave) of the FTMC.
Address: Savanoriu ave. 231, LT-02300, Vilnius, Lithuania
Tel. +370 645 15557; e-mail: office@ftmc.lt

https://doi.org/10.15388/vu.thesis.976
https://orcid.org/0000-0001-9412-9240

VILNIAUS UNIVERSITETAS
FIZINIŲ IR TECHNOLOGIJOS MOKSLŲ CENTRAS

Ignas Bitinaitis

Metalo - dielektrinių plonų dangų formavimas ir tyrimai optinių sensorių ir kosmoso optikos taikymams

DAKTARO DISERTACIJA

Technologijos mokslai,
Medžiagų inžinerija (T 008)

VILNIUS 2026

Disertacija rengta 2021–2025 metais Fizinių ir technologijos mokslų centre. Mokslinius tyrimus rėmė Lietuvos mokslo taryba.

Mokslinis vadovas – dr. Alexandr Belosludtsev (Fizinių ir technologijos mokslų centras, technologijos mokslai, medžiagų inžinerija – T 008).

Gynimo taryba:

Pirmininkas – dr. Gediminas Račiukaitis (Fizinių ir technologijos mokslų centras, technologijos mokslai, medžiagų inžinerija – T 008);

Nariai:

Doc. dr. Renata Butkutė (Fizinių ir technologijos mokslų centras, technologijos mokslai, medžiagų inžinerija – T 008);

Prof. dr. Giedrius Laukaitis (Kauno technologijos universitetas, gamtos mokslai, fizika – N 002);

Prof. dr. Juris Purāns (Latvijos Universitetas, technologijos mokslai, medžiagų inžinerija – T 008).

Doc. dr. Tomas Šalkus (Vilniaus Universitetas, technologijos mokslai, medžiagų inžinerija – T 008);

Disertacija ginama viešame Gynimo tarybos posėdyje 2026 m. rugsėjo mėn. 8 d. 13:00 val. FTMC Fizikos instituto salėje A140. Adresas: Savanorių pr. 231, LT-02300 Vilnius, Lietuva), tel. +370 645 15557; el. paštas: office@ftmc.lt

TABLE OF CONTENTS

INTRODUCTION

Since first cave paintings humans started applying thin graphite films to change reflected light properties. Nowadays, thin films of graphite as well as noble metals, particularly silver and chromium, represent cornerstone materials in modern optics, electronics, and advanced manufacturing technologies. Silver, renowned for its exceptional optical properties including the highest reflectivity across the visible and near-infrared spectrum and superior plasmonic characteristics, finds extensive applications in high-performance mirrors, transparent conductors, and sensing devices. Chromium, with its unique combination of mechanical durability, chemical stability, and distinctive optical response, serves critical roles in protective coatings, optical filters, and adhesion layers.

The controlled deposition and characterization of these materials present significant scientific and technological challenges. The formation mechanisms of ultrathin metallic films involve processes of nucleation, island growth, coalescence, and percolation, each influencing the final optical, electrical, and mechanical properties. Understanding and controlling these processes requires characterization techniques capable of providing real-time insights into film evolution and final properties.

This dissertation addresses fundamental questions in thin-film materials science, optical engineering, and advanced manufacturing technologies. The work advances from fundamental investigations of ultrathin film growth and optical characterization to the development of functional metal–dielectric structures for biosensing, optical filtering, space optics, and high-power laser applications. Particular attention is devoted to aluminium alloying effects on silver film stability, effective medium approximation modelling of ultrathin metallic layers, and chromium-based multilayer structures supporting sub-milliradian Fano resonances. The developed materials, characterization approaches, and optical architectures contribute to the advancement of next-generation optical systems and sensors requiring high performance, stability, and environmental durability.

AIMS OF THE THESIS

Objective of the Dissertation

To investigate thin metal layers physical and optical properties - their reflection and transmittance behaviour depending on layer thickness, material purity (doping), integration into multilayer structure. Implement findings in practical applications for space optics, laser systems and sensors.

Dissertation research objectives

1. Investigate formation stages of ultrathin sputtered silver films using in-situ and ex-situ methods, compare their sensitivity and reproducibility.
2. To investigate influence of aluminium doping in silver thin films - optical response, surface morphology, and resistance to ion-induced degradation simulating space environment.
3. To investigate and improve surface optical quality of selective laser melted actively cooled mirror structures through the application of high-reflective Ag–Al mixed coatings and controlled polishing with different grit sizes.
4. Design, fabrication, and experimental characterisation of planar chromium-based metal–dielectric multilayer stacks that support sharp angular and spectral filtering via Fano-type resonances.
5. Design, fabrication, and experimental characterisation of planar silver-based metal–dielectric multilayer stacks for plasmon waveguide resonance and Total Internal Reflection Ellipsometry (TIRE) sensors.

Scientific novelty and practical value

1. It was shown that transmittance Broadband Monitoring (BBM) of the growing silver layer allows reliable in-situ estimation of minimum thickness when film becomes continuous.
2. Silver films with 8 % of aluminium admixing shows significant decrease in surface roughness, while maintaining high reflectivity properties of pure silver films in Visual - Infrared (VIS-IR) range.

3. It was shown that effective combination of selective laser melting, polishing and magnetron sputtering technologies allows to achieve efficient manufacturing of complex-shape high reflectivity metal mirrors.
4. For the first time it is shown that chromium's Fano resonances provides platform for advanced optical filters.
5. For the first time it is shown how silver-based planar metal–multilayer–dielectric stacks support waveguide mode and improve the sensitivity of Total Internal Reflection Ellipsometry (TIRE) for biosensors.

Statements of defence

1. Enhanced optical sensor sensitivity up to 8.5×10^{-7} RIU, reaching four times of classical gold sensors, can be obtained through optimization of transparent silver layer thickness integrated into dielectric multilayer structure. The transition of silver film to a continuous state on dielectric substrates can be identified using in-situ optical monitoring in the wavelength near Localised Surface Plasmon Resonance (LSRP) peak.
2. High-reflectance protected metal mirrors can be effectively fabricated by selective laser melting base structure, followed by precision polishing and tailored reflective coating deposition. In the VIS–IR range, silver coating with 8% aluminium doping offers optimal performance, with improved ion bombardment resistance of 20 keV H^- ions up fluences of 1.8×10^{16} cm^{-2} and lower surface roughness of R_a = 2.3 nm.

Approbation

Scientific publications ***directly related*** *to the topic of the dissertation:*

A. Alexandr Belosludtsev, Anna Sytchkova, Naglis Kyžas, **Ignas Bitinaitis**, Rimantas Simniškis, Ramutis Drazdys, "Ultrathin sputtered silver films protected by ALD alumina: Comparison of in-situ investigation with ex-situ resistance and ellipsometric measurements", Vacuum, Volume 195, 2022, 110669. https://doi.org/10.1016/j.vacuum.2021.110669.

B. Alexandr Belosludtsev, **Ignas Bitinaitis**, Julijanas Želudevičius, Vitalij Kovalevskij, Sabereh T. Rastkar, Anna Sytchkova, "Proton resistance of high reflective silver-aluminium mirrors for space applications", Advances in Space Research, 2026, doi: 10.1016/j.asr.2026.06.103

C. **Ignas Bitinaitis**, Karolis Stravinskas, Sergejus Borodinas, Genrik Mordas, Alexandr Belosludtsev "Reflectivity improvement of lightweight active cooled metal mirrors manufactured by additive manufacturing". Optical Materials, Volume 169, 2026, 117570. doi: 10.1016/j.optmat.2025.117570.

D. Svitlana Ilchenko, Alexandr Belosludtsev, **Ignas Bitinaitis**, Volodymyr Panasyuk, Volodymyr Taranenko. "Fano-resonant filtering by planar chromium-based multilayer stacks", Optics Letters, 2025, Volume 50, 7019–7022. doi: 10.1364/OL.569973.

E. Tomas Rakickas, **Ignas Bitinaitis**, Victor Reshetnyak, Edita Voitechovič, Alexandr Belosludtsev "Total internal reflection ellipsometry for multilayer plasmon waveguide resonance sensors", Sensors and Actuators B: Chemical, Volume 452, 2026, 139454. doi: 10.1016/j.snb.2026.139454.

Conference presentations:

1. **Ignas Bitinaitis**. "Comparison of in-situ and ex-situ investigations of ultrathin sputtered silver film growth". FizTeCh 2021, Vilnius, Lithuania, 20–21 October 2021 (poster presentation).
2. **Ignas Bitinaitis**, Anna Sytchkova, Naglis Kyžas, Rimantas Simniškis, Ramutis Drazdys, Alexandr Belosludtsev. "Detailed investigations from nanoscale to bulk of silver film growth". Open Readings 2022, Vilnius, Lithuania, 15–18 March 2022 (poster presentation).
3. **Ignas Bitinaitis**, Anna Sytchkova, Naglis Kyžas, Rimantas Simniškis, Ramutis Drazdys, Alexandr Belosludtsev. "Sputtered silver film growth investigation". FizTeCh 2022, Vilnius, Lithuania, 19–20 October 2022 (poster presentation).
4. **Ignas Bitinaitis**, Alexandr Belosludtsev, Edvinas Petraitis, Anna Sytchkova. "AgAl mixed films for space applications". Open Readings 2023, Vilnius, Lithuania, 18–21 April 2023 (poster presentation).

5. J. Judek, R. Mroczyński, C. Jastrzębski, M. Ożga, A. Seweryn, B. Witkowski, M. Godlewski, A. Belosludtsev, **I. Bitinaitis**. "Metody pasywacji materiałów 2D na przykładzie grafenu CVD". XIV Konferencja Naukowa Technologia Elektronowa (ELTE 2023), Ryn, Poland, 18–21 April 2023.
6. **Ignas Bitinaitis**. "Aluminium doped silver films for space applications". FizTeCh 2023, Vilnius, Lithuania, 18–19 October 2023 (oral presentation).
7. **Ignas Bitinaitis**, Alexandr Belosludtsev, Gunnar Suchaneck, Sitao Wang, Gerald Gerlach, Nikolai Sobolev. "Reactive multitarget magnetron sputtering of Sr_2FeMoO_6 films". Advances in Optical Thin Films VI, SPIE Optical Systems Design, Strasbourg, France, 7–11 April 2024 (poster presentation). DOI: 10.1117/12.3029571.
8. **Ignas Bitinaitis**. "Reactive magnetron sputtering of Sr_2FeMoO_6 film". FizTeCh 2024, Vilnius, Lithuania, 15–17 October 2024 (poster presentation).
9. Edita Voitechovič, Tomas Rakickas, **Ignas Bitinaitis**, Victor Reshetnyak, Anatoly Suprun, Liudmyla Shmeleva, Alexandr Belosludtsev. "On the Way of Development of Versatile Optical Sensor for the Monitoring of the Biological Molecule Interactions by the Surface Plasmon Resonance Imaging (SPRI)". 4th Baltic Biophysics Conference (BBC 2024), Kaunas, Lithuania, 3–4 October 2024 (poster presentation).
10. Alexandr Belosludtsev, **Ignas Bitinaitis**, Anna Sytchkova, Vitalij Kovalevskij. "Investigation of metal mirrors for space communication applications". 41st International Scientific Conference of the Institute of Solid State Physics, University of Latvia, Riga, Latvia, 3–7 March 2025 (oral presentation).
11. Edita Voitechovič, Tomas Rakickas, **Ignas Bitinaitis**, Victor Reshetnyak, Anatoly Suprun, Liudmyla Shmeleva, Alexandr Belosludtsev. "Development of optical sensor for surface plasmon resonance imaging and test for biological interactions". 10th Symposium on Optical Coatings for Laser Applications (OCLA 2025), Vilnius, Lithuania, 8 May 2025 (poster presentation).
12. Alexandr Belosludtsev, Tomas Rakickas, Edita Voitechovič, **Ignas Bitinaitis**, Viktor Reshetnyak, Anatoly Suprun, Liudmyla Shmeleva. "Development of plasmon-waveguide resonance sensor for

investigation of biological interactions". School on Biophotonics, Alghero, Italy, 9–13 June 2025 (poster presentation).

13. Alexandr Belosludtsev, **Ignas Bitinaitis**, Karolis Stravinskas, Anna Sytchkova. "Investigation of silver-aluminium mixed mirrors for space communication applications". CEWQO29: The 29th Central European Workshop on Quantum Optics, Vilnius, Lithuania, 23–27 June 2025 (poster presentation).
14. Anatoly Suprun, Viktor Reshetnyak, Liudmyla Shmeleva, Alexandr Belosludtsev, Tomas Rakickas, Edita Voitechovič, **Ignas Bitinaitis**. "Direct calculation of resonance characteristics at surface plasmon resonance for complex layered structures of sensor chip". NANO-2025: 13th International Conference on Nanotechnologies and Nanomaterials, Bukovel, Ukraine, 20–23 August 2025 (poster presentation).
15. Anna Sytchkova, Alexandr Belosludtsev, **Ignas Bitinaitis**, Karolis Stravinskas, Vitalij Kovalevskij. "Deep space proton radiation resistance of enhanced silver mirrors". 2025 IEEE International Conference on Space Optical Systems and Applications (ICSOS 2025), Kyoto, Japan, 28–31 October 2025 (oral presentation).
16. **Ignas Bitinaitis**, Alexandr Belosludtsev, Karolis Stravinskas, Vitalij Kovalevskij, Anna Sytchkova. "Investigation of silver-aluminium mixed mirrors for space applications". LFNK'46 (46th Lithuanian National Physics Conference), Kaunas, Lithuania, 8–10 October 2025 (poster presentation).
17. Alexandr Belosludtsev, Tomas Rakickas, Edita Voitechovič, **Ignas Bitinaitis**, Viktor Reshetnyak, Anatoly Suprun, Liudmyla Shmeleva. "Development of metal dielectric multilayer coating for high sensitive biological interactions sensor". Advanced Materials and Technologies: 27th International Conference-School, Palanga, Lithuania, 25–29 August 2024 (poster presentation).
18. Alexandr Belosludtsev, **Ignas Bitinaitis**, Karolis Stravinskas, Vitalij Kovalevskij, Anna Sytchkova. "Silver-aluminium high mirrors for space communication applications". International Conference on Quantum Photonics Development in the Baltic Region, Riga, Latvia, 11–13 February 2026.
19. Alexandr Belosludtsev, **Ignas Bitinaitis**, Vitalij Kovalevskij, Karolis Stravinskas, Titas Tamošauskas "Reflectivity improvement of

lightweight additive manufactured metal mirrors for space applications". Advances in Optical Thin Films IX, SPIE Optical Systems Design, Strasbourg, France, 13–16 April 2026. DOI: 10.1117/12.3100004.

20. Alexandr Belosludtsev, **Ignas Bitinaitis**, Vitalij Kovalevskij, Karolis Stravinskas, Anna Sytchkova "Metal high reflective mirrors for space applications". Developments in Optics and Communications (DOC) and OptoMeeting (OPTO), Riga, Latvia, 1–3 July 2026 (poster presentation).
21. Alexandr Belosludtsev, **Ignas Bitinaitis**, Vitalij Kovalevskij, Sabereh T. Rastkar, Anna Sytchkova "Metal high reflective mirrors for space applications". Advanced Materials and Technologies: 28th International Conference-School, Palanga, Lithuania, 24–28 August 2026 (poster presentation).

Author's personal and co-authors' contribution

The author personally carried out most of the experiment depositions, measurements, measurement analysis, analysis descriptions and modelling.

The thesis supervisor Dr. A. Belosludtsev contributed to the experimental plan, deposition optimisation, valuable suggestions and comments during the research and preparation of the thesis.

All co-authors of the publications contributed to the preparation of the publications concept ideas, texts and valuable comments and insights.

DISSERTATION OVERVIEW

This dissertation is presented as a collection of five scientific articles [A-E] which have been published to leading high-quality international journals. The articles summarize the key findings achieved during my doctoral research starting from September 2021.

RESEARCH OVERVIEW

1. THICKNESS-DEPENDENT PHYSICAL PROPERTIES OF THIN METALLIC FILMS.

1.1 Thin film growth mechanisms and morphology evolution

Physical properties of thin metallic layers differ substantially from those of bulk materials, particularly in the thickness range below 100 nm, where the film morphology, atomic arrangement, and electron transport become strongly dependent on the growth mechanism and substrate interaction. In ultrathin films, the optical, electrical, and mechanical behaviour is governed not only by intrinsic material properties, but also by nucleation dynamics, surface diffusion, crystallographic structure, and the continuity of the deposited layer. As a result, the transition from isolated metallic clusters to a continuous conducting film represents one of the most critical stages in thin film formation.

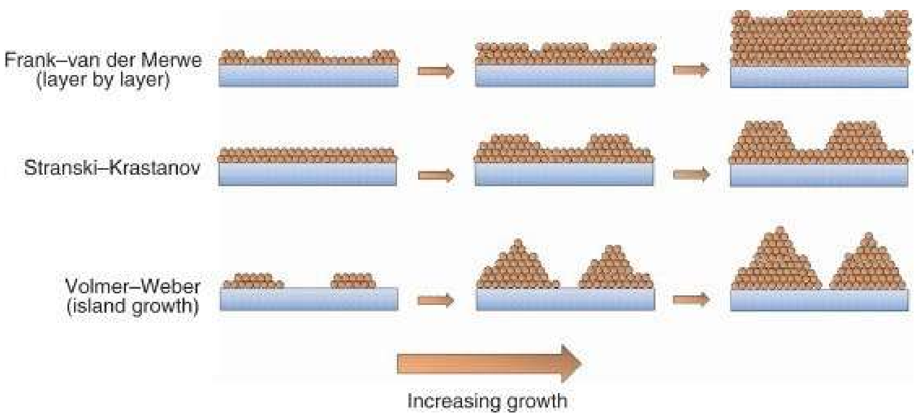

Figure 1. Layer growth modes [1]

Growth of metallic films on dielectric substrates is typically described by three principal growth modes: Frank–van der Merwe (layer-by-layer), Volmer–Weber (island growth), and Stranski–Krastanov (layer-plus-island) growth (Figure 1) [2]. The dominant growth mechanism is determined by the balance between substrate surface energy, cohesive energy of deposited atoms, and interface energy between the film and substrate. Noble metals such as silver and gold deposited on oxide or glass substrates generally follow the Volmer–Weber growth mode because the cohesive energy between metal atoms exceeds their adhesion to dielectric surfaces. Under these conditions, deposited atoms initially form separated three-dimensional islands which gradually coalesce into a continuous layer with increasing thickness. This behaviour is particularly important for optical coatings and plasmonic structures because film continuity directly determines optical losses, conductivity, and plasmon propagation characteristics.

Silver remains one of the most extensively investigated thin film materials due to its exceptionally high reflectance and low optical losses in visible and near-infrared wavelengths [A, B]. However, ultrathin silver layers below 15 nm thickness exhibit strong tendency toward island-type growth on dielectric substrates where during initial deposition stages, isolated nanoparticles and metallic clusters dominate the morphology, resulting in discontinuous electrical conductivity and enhanced optical scattering. As the deposition proceeds, neighbouring islands begin to merge during the coalescence stage, eventually reaching the percolation threshold where conductive pathways form across the substrate surface.

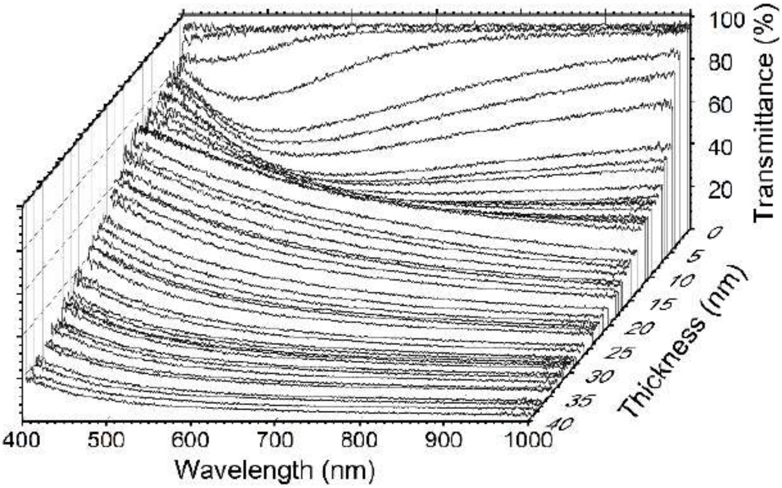

Figure 2. Transmittance spectra evolution during silver film growth on fused silica substrate, recorded real-time in-situ.

In publication [A] it was demonstrated that sputtered silver films deposited on fused silica substrates become electrically percolated at approximately 6 nm thickness, while formation of a fully continuous layer occurs near 12 nm [A]. The study further showed that selective-wavelength broadband optical monitoring allows reliable in-situ identification of both coalescence and percolation stages, which is critical for high-precision fabrication of ultrathin optical coatings (Figure 2) [A]. Such monitoring becomes particularly important for reliable and repeatable fabrication of plasmonic and resonant optical structures, where sub-nanometer thickness variations may significantly alter optical response of final optical sensor or structure.

1.2 Continuity transition and electromagnetic behaviour

The transition from discontinuous to continuous morphology produces rapid changes in optical response due to evolution of collective electron behaviour and dielectric properties of the growing film. Such thickness-dependent optical variations can be monitored in situ using transmission or ellipsometric measurements, providing valuable information about film coalescence and continuity development [A]. While electrical resistance measurements typically exhibit a sharp transition at the percolation threshold, optical monitoring demonstrates a substantially smoother and more continuous response during thin film growth (Figure 3). This gradual optical evolution provides improved sensitivity for evaluation of film continuity, morphological uniformity, and coalescence behaviour throughout the deposition process.

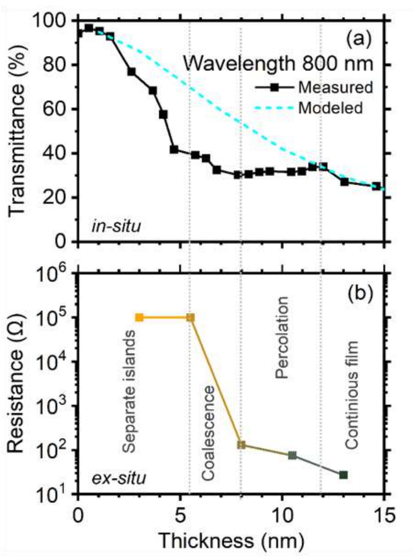

Figure 3. Transmittance (a), LSPR Maximum position and (b) resistance values evolution with the silver film thickness. The dotted vertical lines indicate three various stages of the growing film.

Ellipsometric investigations of ultrathin silver layers revealed that optical continuity may emerge earlier near the film surface than at the substrate interface, suggesting vertically non-uniform film evolution during growth [A]. Such behaviour indicates that ultrathin metallic films near the percolation threshold cannot always be accurately described using homogeneous isotropic models.

1.3 Crystallographic structure, roughness, and alloying effects

Atomic structure and crystallographic arrangement further influence thin film evolution. Metals with face-centered cubic (FCC) crystal structures, such as Ag and Al, possess high atomic packing density and relatively high surface mobility during deposition. Elevated adatom mobility promotes island growth and larger grain formation, particularly under low-defect deposition conditions. However, excessive grain growth may increase surface roughness and optical scattering. In high-reflectivity optical systems, nanometer-scale roughness becomes particularly critical because surface irregularities introduce scattering losses and phase distortions.

Optimization of thin film microstructure through alloying represents one of the strategies for controlling morphology and optical quality of ultrathin metallic coatings. Silver–aluminium mixed films provide one example of controlled modification of nucleation behaviour and structural evolution [B]. Incorporation of aluminium suppresses excessive grain coalescence and promotes smoother film morphology while maintaining high reflectance. Reduced surface roughness decreases optical scattering losses and improves structural uniformity, which is particularly important for high-reflectivity optical systems and resonant multilayer structures.

1.4 Thickness-dependent behaviour in resonant and optical sensor applications

While noble metals such as silver are primarily optimized for high reflectance and low optical losses, other metallic thin films may be intentionally utilized for their absorptive and damping properties in resonant optical structures. In contrast to silver, chromium exhibits substantially different growth behaviour on dielectric substrates and is capable of forming relatively uniform and continuous ultrathin films at thicknesses of only a few nanometers. Such growth characteristics are particularly important in resonant multilayer systems where precise control of absorption, electromagnetic coupling, and interface uniformity is required. Although chromium possesses significantly higher optical losses and lower conductivity compared to silver, its dielectric response and stable ultrathin morphology enable formation of highly selective resonant states when integrated into metal–dielectric multilayer architectures.

In chromium-based planar structures, thin metallic layers support hybrid Tamm–waveguide modes and narrow Fano-type resonances with angular selectivity reaching sub-milliradian widths [D]. The optical response of such structures depends critically on chromium thickness because the balance between absorption, coupling efficiency, and resonance confinement is highly thickness-sensitive. Thin chromium layers provide sufficient electromagnetic coupling while simultaneously maintaining controlled damping necessary for stable resonance formation.

In plasmonic biosensors, the thickness of metallic films determines the excitation efficiency and propagation characteristics of surface plasmon and waveguide modes. Classical surface plasmon resonance sensors commonly employ gold films with thicknesses near 50 nm because thinner layers exhibit excessive damping while thicker layers suppress plasmon excitation efficiency [E]. In multilayer plasmon waveguide resonance structures employing silver-based coatings, thickness optimization becomes even more critical due to the strong interaction between plasmonic and dielectric waveguide modes [E]. Experimental investigations of multilayer plasmon waveguide resonance structures combined with total internal reflection ellipsometry demonstrated significantly improved biosensor sensitivity and phase interrogation performance compared to conventional single-layer plasmonic sensors [E]. The observed sensitivity enhancement originates from optimized confinement of electromagnetic fields inside the multilayer structure, which strongly depends on precise control of thin film thicknesses and interface quality.

2. THICKNESS-DEPENDENT OPTICAL PROPERTIES OF THIN METALLIC FILMS.

2.1 Optical response of ultrathin metallic films

Optical response of metals originates primarily from the interaction between free conduction electrons and incident electromagnetic radiation. In bulk metals, this interaction is commonly described by the Drude model [3], where optical properties depend on plasma frequency and electron scattering rates. In ultrathin films, however, the electron mean free path becomes comparable to film thickness, causing enhanced electron scattering at surfaces and grain boundaries. This additional scattering modifies both the real and imaginary parts of the dielectric permittivity, resulting in increased absorption losses and reduced reflectivity compared to bulk materials. Consequently, optical constants of thin metallic layers cannot be treated as thickness-independent material parameters.

In addition to intrinsic electron scattering effects, optical behaviour of ultrathin metallic layers becomes strongly influenced by nanoscale morphology, film continuity, roughness, grain boundaries, and interface quality. As film thickness decreases toward the nanometer scale, classical bulk optical behaviour gradually transitions toward regimes dominated by localized plasmonic phenomena, non-uniform electron transport, and effective medium behaviour [4]. Under such conditions, optical response depends not only on intrinsic dielectric properties of the material, but also on structural evolution occurring during thin film growth. These thickness-dependent optical phenomena become particularly important in noble metal thin films intended for plasmonic and high-reflectivity optical applications.

Silver exhibits the highest reflectivity among all metals in the visible and near-infrared spectral regions due to its low absorption and highly negative real dielectric permittivity. For this reason, silver films are widely used in high-performance mirrors, plasmonic devices, and optical coatings. Nevertheless, ultrathin silver layers demonstrate strong thickness-dependent optical behaviour associated with discontinuous island growth during initial deposition stages [A, B].

2.2 Optical properties near the percolation threshold

At thicknesses below the percolation threshold, isolated metallic islands dominate the morphology and support localized surface plasmon resonances.

In this regime, incident light excites collective electron oscillations confined within individual nanoparticles or clusters, producing strong absorption and scattering losses (Figure 4). As a result, ultrathin discontinuous silver layers may exhibit relatively low reflectivity and non-monotonic transmission spectra despite the intrinsically high optical quality of bulk silver.

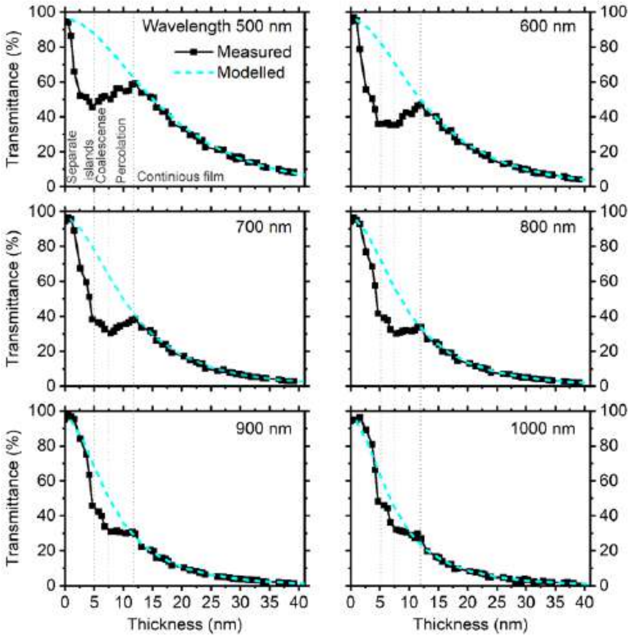

Figure 4. Real-time in-situ transmittance values measured during silver growth at various wavelengths from 500 nm to 1000 nm. Measured and modeled transmittance values are shown.[A]

As film thickness increases, neighbouring islands begin to merge and form conductive pathways. This coalescence process substantially alters the optical response because localized plasmon resonances gradually transform into collective metallic behaviour characteristic of continuous films. Broadband optical monitoring of sputtered silver layers demonstrated that transmission spectra evolve rapidly during the continuity transition, indicating strong sensitivity of optical properties to nanoscale morphological changes [A]. Around the percolation threshold, small thickness variations of less than one nanometer may produce abrupt changes in transmission, reflectance, and ellipsometric phase response. Such sensitivity makes ultrathin metallic films highly attractive for optical sensing applications while simultaneously creating significant fabrication challenges.

The optical behaviour of discontinuous films is often described using effective medium approximation models, where the metallic layer is treated as a composite medium consisting of metal clusters embedded in dielectric surroundings [5]. In this approach, the effective dielectric permittivity depends on metal filling fraction, island geometry, and cluster distribution. However, near the percolation threshold conventional effective medium models frequently fail to accurately reproduce experimental spectra because the film morphology becomes highly non-uniform and electrically anisotropic. Ellipsometric investigations of ultrathin silver films revealed that optical continuity may emerge earlier near the film surface than at the substrate interface, suggesting vertically inhomogeneous film evolution during growth [A]. Such behaviour demonstrates that optical response in ultrathin films cannot always be represented by homogeneous isotropic layers. Yet by monitoring material specific wavelength related to local surface plasmon resonance and comparing its transmittance to effective thickness models it is possible to precisely determine film growth stages and thinnest possible continuous layer thickness. This approach significantly improves thin film deposition repeatability and precision compared to commonly used thin film resistance measurements for coating continuity determination.

2.3 Resonant optical phenomena in thin metallic films

Material type strongly influences thickness-dependent optical properties because different metals possess distinct electronic structures and dielectric functions. Noble metals such as silver and gold exhibit relatively low optical losses due to weak interband absorption in the visible spectral region, enabling efficient plasmon excitation and high reflectivity [6]. In contrast, transition metals including chromium, titanium, and nickel exhibit significantly higher absorption caused by strong interband electronic transitions. Consequently, chromium layers display lower reflectance but enhanced damping of electromagnetic modes, which can be advantageous in resonant multilayer optical systems.

In publication [D] chromium-based multilayer structure demonstrates how controlled optical losses may be utilized for advanced spectral filtering. In planar metal–dielectric stacks containing thin chromium films, interference between waveguide and surface modes generates narrow Fano-type resonances characterized by asymmetric spectral profiles and extremely sharp angular selectivity. The optical properties of these structures depend critically on chromium thickness because excessive absorption suppresses resonance formation while insufficient absorption weakens mode confinement. Thin chromium layers therefore operate in a balance regime where optical damping and resonant coupling are simultaneously optimized. Such structures demonstrate that highly absorbing metals may provide unique optical functionality when integrated into properly engineered multilayer systems.

As discussed previously, nanometer-scale roughness introduces diffuse scattering losses that reduce specular reflectance and broaden resonant spectral features. In high-reflectivity optical coatings, roughness-induced scattering may become comparable to intrinsic absorption losses, particularly in multilayer systems requiring coherent interference effects. Grain boundaries and crystallographic defects additionally contribute to optical damping through enhanced electron scattering. Therefore, optimization of deposition parameters, substrate preparation, and post-processing techniques is essential for achieving high optical quality in ultrathin metallic films.

2.4 Thickness optimization in optical systems

Optimization of deposition parameters, substrate preparation, and post-processing procedures therefore becomes essential for achieving stable optical performance. Alloying represents one approach for improving morphological and optical stability of thin metal layers. Silver–aluminium mixed films exhibit reduced surface roughness compared to pure silver coatings while maintaining high reflectance across visible and infrared wavelengths [B]. The addition of aluminium modifies nucleation dynamics and suppresses excessive grain growth, producing smoother and more homogeneous films. Improved structural uniformity reduces optical scattering and enhances environmental durability. Furthermore, aluminium incorporation improves resistance to proton-induced degradation relevant to space optical applications, where metallic mirrors are exposed to radiation, atomic oxygen, and thermal cycling [B].

In plasmonic and biosensing applications, thickness optimization determines electromagnetic field localization and sensor sensitivity. Surface plasmon resonance occurs when incident light couples to collective oscillations of free electrons at a metal–dielectric interface. Efficient excitation requires precise matching of optical momentum and is highly sensitive to metal thickness [7]. Excessively thin films exhibit discontinuous morphology and insufficient electron density, whereas excessively thick layers suppress evanescent field penetration and increase optical losses. Multilayer plasmon waveguide resonance structures employing silver layers and dielectric stacks overcome some of these limitations by combining plasmonic and waveguide confinement mechanisms [E]. Such structures support enhanced electromagnetic localization and sharper resonances compared to conventional single-metal-layer sensors. Experimental investigations demonstrated that optimized multilayer architectures substantially improve phase sensitivity in total internal reflection ellipsometry configurations [E].

Optical interference effects become increasingly important when film thickness approaches the wavelength scale divided by the refractive index. In multilayer thin film systems, constructive and destructive interference between reflected waves enables engineering of spectral transmission and reflection characteristics. Thin metallic layers often serve simultaneously as reflective, absorptive, and coupling elements in such systems. Their optical behaviour therefore depends not only on intrinsic dielectric properties but also on interactions with neighbouring dielectric layers, interface quality, and coherence conditions. Small deviations in thickness may shift resonance positions, broaden spectral features, or significantly reduce device efficiency.

3. THIN METAL LAYERS MATERIAL PURITY AND DOPING

3.1 Influence of material purity on thin film properties

Optical and physical properties of thin metallic layers are highly sensitive to material purity, atomic-scale defects, and the presence of intentionally introduced impurities or dopants. In thin films, where thicknesses are often comparable to electron mean free paths and characteristic diffusion lengths, even relatively small compositional variations may significantly alter crystallization dynamics, electron transport, optical absorption, surface morphology, and environmental stability. As a result, material purity becomes one of the key parameters governing the performance of thin film optical systems, particularly in applications requiring low optical losses, high reflectivity, long-term stability, or controlled plasmonic behaviour.

In pure metallic films, optical response is primarily determined by the density and mobility of free conduction electrons. High-purity metals generally exhibit lower electron scattering rates, leading to reduced optical absorption and improved reflectivity. This effect is particularly important for noble metals such as silver, which possesses the lowest optical losses in the visible and near-infrared spectral ranges among commonly used metals. High reflectivity of silver originates from its high free-electron density and weak interband absorption within the visible spectrum. However, the optical advantages of pure silver are accompanied by several technological limitations, including poor adhesion to dielectric substrates, susceptibility to oxidation and sulfur contamination, strong grain growth tendencies, and relatively low environmental stability.

The influence of impurities on thin films possess a high surface-to-volume ratio and non-equilibrium microstructures formed during deposition. Impurity atoms introduced during growth may segregate at grain boundaries, alter surface diffusion rates, or modify nucleation dynamics. Consequently, small dopant concentrations may produce disproportionately large changes in morphology and optical behaviour. In sputtered thin films, impurity incorporation often affects grain size, roughness, crystallographic orientation, and defect density, all of which contribute directly to optical scattering and absorption losses.

3.2 Doping-induced modification of morphology and optical response

Doping is frequently employed as a strategy for balancing competing material properties that cannot be simultaneously optimized in pure films. While high-purity silver provides maximum reflectance, alloying with secondary elements may improve mechanical durability, thermal stability, radiation resistance, and surface smoothness with only moderate reduction in optical performance. Silver–aluminium mixed films represent one such example where controlled impurity incorporation enables substantial improvement of morphological stability and environmental resistance [B].

Addition of aluminium modifies the film growth process by reducing excessive grain coalescence and suppressing formation of large surface features. As a result, Ag–Al coatings exhibit lower roughness and improved microstructural homogeneity compared to pure silver layers while maintaining high reflectance across visible and infrared spectral regions (Figure 5) [B].

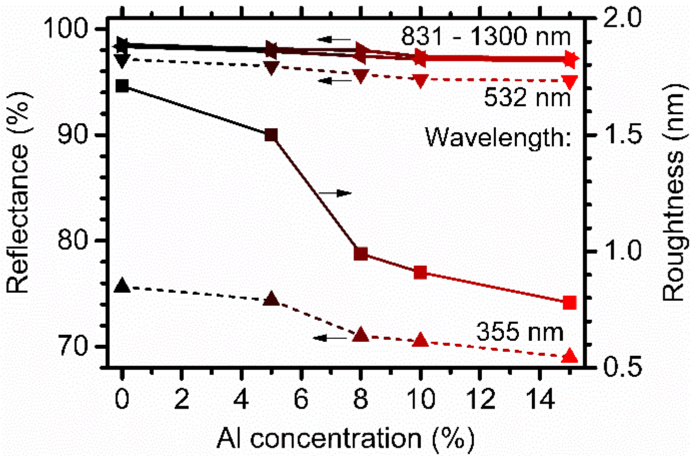

Figure 5. Dependence of reflectance at various wavelengths and roughness values on the Ag-Al mixed films with 0 - 15 % Al concentration [B].

The optical effects of doping originate from several interconnected mechanisms. First, impurity atoms increase electron scattering inside the metallic lattice, reducing electrical conductivity and modifying the complex dielectric function. Increased scattering primarily affects the imaginary part of dielectric permittivity, leading to higher absorption losses and reduced plasmon propagation lengths. Second, dopants may alter the crystalline structure and grain morphology, indirectly influencing optical scattering at surfaces and grain boundaries. Third, alloying can modify oxidation kinetics and chemical stability, affecting long-term optical performance under environmental exposure.

In plasmonic and optical coating applications, material composition must therefore be carefully optimized to balance optical performance and structural stability. While increased impurity concentration generally enhances electron scattering and optical damping, moderate alloying may simultaneously improve film homogeneity, reduce roughness, and suppress degradation processes. Consequently, controlled doping represents a practical approach for tailoring thin film properties to specific optical applications while maintaining acceptable reflectance and environmental durability.

3.3 Doping effects near the percolation threshold

The relationship between purity and morphology is especially pronounced in ultrathin metallic films near the percolation threshold. During initial growth stages, impurity atoms may significantly modify island nucleation density and coalescence kinetics. Increased nucleation density generally produces smaller grains and smoother surfaces, whereas reduced nucleation promotes larger island formation and increased roughness. Since optical properties in ultrathin films strongly depend on continuity and surface morphology, dopant-induced changes in growth dynamics directly influence reflectance and transmission spectra.

Study of sputtered silver layers demonstrated that morphological evolution during coalescence strongly affects ellipsometric response and broadband transmission behaviour [A]. Such sensitivity indicates that even small compositional variations may shift the continuity threshold and modify effective optical constants.

3.4 Environmental, thermal, and radiation stability

Environmental stability represents another major challenge for thin metallic coatings. Pure silver films readily degrade under atmospheric exposure due to sulfur contamination, oxidation, and diffusion-related structural changes. These processes increase optical absorption and reduce reflectance over time. Doping may substantially improve resistance to such degradation mechanisms. Aluminium incorporation into silver layers enhances structural stability by forming more chemically robust microstructures and reducing surface diffusion activity [B]. Proton irradiation experiments simulating space environment conditions further demonstrated improved resistance of Ag–Al coatings to radiation-induced degradation compared to pure silver mirrors [B]. Such behaviour is particularly important for aerospace optics, where thin metallic layers are exposed to energetic particles, ultraviolet radiation, and extreme thermal fluctuations.

Material purity also affects thermal and mechanical stability of thin films. Pure metallic layers with large grains often develop internal stress gradients during deposition and thermal cycling, potentially leading to cracking, delamination, or roughness evolution. Controlled incorporation of secondary elements may stabilize the microstructure by limiting grain boundary mobility and suppressing recrystallization processes. In optical multilayer systems, where precise interface quality is essential for interference effects and resonance formation, such stabilization becomes critically important. Even nanometer-scale roughness growth may significantly increase scattering losses or broaden resonant spectral features.

3.5 Material composition in resonant optical systems

In resonant multilayer photonic structures, controlled optical absorption introduced by specific materials may itself become functionally beneficial. Chromium-based multilayer systems illustrate how metals with intrinsically higher damping can support narrow Fano resonances and waveguide-coupled optical modes [D]. Although chromium possesses lower reflectivity and higher absorption compared to noble metals, its dielectric properties enable stable resonance formation in carefully designed multilayer geometries. In such systems, optical functionality depends not solely on minimizing losses, but rather on achieving an optimal balance between absorption, confinement, and electromagnetic coupling. This demonstrates that the role of impurities and material composition in optical systems is highly application-dependent.

Deposition technology further influences impurity incorporation and achievable film purity. Magnetron sputtering, widely used for optical coating fabrication, allows relatively precise control of composition through target purity, gas atmosphere, deposition pressure, and co-sputtering configurations. However, residual contamination from chamber atmosphere, substrate surfaces, or target impurities may still affect ultrathin film properties. Oxygen contamination is particularly significant because even substoichiometric oxide formation at interfaces may alter nucleation behaviour and optical response. Therefore, optimization of deposition conditions is often equally important as nominal material composition.

4. MULTILAYER THIN FILMS

4.1 Fundamentals of multilayer optical structures

Single metallic or dielectric layers rarely provide sufficient functionality for advanced optical systems because many optical properties emerge not from an individual material itself, but from electromagnetic interaction between multiple interfaces and layers. For this reason, modern optical coatings are commonly based on multilayer architectures in which carefully engineered sequences of metallic and dielectric films collectively determine reflectance, transmission, absorption, resonance behaviour, thermal stability, and environmental durability. In such systems, the optical response depends simultaneously on material composition, layer thicknesses, interface quality, structural symmetry, and external optical configuration. As a result, multilayer thin films represent not only a combination of materials, but a complex electromagnetic structure whose behaviour often differs fundamentally from the properties of its individual components.

The operation of multilayer optical coatings is primarily governed by interference phenomena. When electromagnetic waves encounter interfaces between materials with different refractive indices, partial reflection and transmission occur at each boundary. Constructive and destructive interference between these reflected waves enables precise control of spectral and angular optical response. By selecting appropriate optical thicknesses and refractive index contrasts, multilayer systems may function as mirrors, antireflection coatings, spectral filters, absorbers, resonators, or waveguides. In metallic multilayer structures, additional plasmonic and dissipative effects further expand the range of achievable optical phenomena.

Dielectric multilayer systems are widely used for high-reflectivity mirrors because repeated refractive index modulation enables efficient Bragg reflection. Alternating high- and low-index dielectric layers can produce reflectance values exceeding 99.9% within selected spectral ranges while maintaining relatively low absorption losses. However, dielectric mirrors alone are not always sufficient for applications requiring broadband reflectivity, plasmonic coupling, or electrically conductive surfaces. Metallic layers are therefore frequently incorporated into multilayer architectures to provide additional optical functionality. Noble metals such as silver and gold are especially important because their high free-electron density enables strong reflectance and surface plasmon excitation.

4.2 Metallic layers and plasmonic multilayer systems

The integration of metallic layers into multilayer structures introduces complexity because metal films simultaneously support reflection, absorption, and near-field electromagnetic coupling. In ultrathin metallic layers, optical behaviour becomes strongly dependent on film continuity, morphology, and interface quality. As a result, even small deviations in thickness or roughness may significantly alter resonance conditions and spectral response. Precise deposition control therefore becomes essential for fabrication of reproducible multilayer optical systems.

One important class of multilayer structures is based on plasmonic resonances occurring at metal–dielectric interfaces. Surface plasmon resonance systems typically employ thin noble metal layers coupled to dielectric environments through prism geometries or waveguide structures. Efficient excitation of plasmon modes requires strict momentum matching between incident light and the plasmonic wave propagating along the interface. Consequently, the overall optical architecture becomes equally important as the thin film materials themselves. Parameters such as prism refractive index, incidence angle, polarization state, dielectric environment, and substrate geometry directly influence resonance excitation efficiency and sensitivity [D, E].

Multilayer plasmon waveguide resonance structures extend classical surface plasmon systems by introducing additional dielectric layers capable of supporting guided electromagnetic modes. In such architectures, coupling between plasmonic and waveguide modes produces enhanced field confinement and sharper resonant responses. In publication [E] was demonstrated that silver-based multilayer structures combined with fixed angle of incidence total internal reflection ellipsometry can significantly improve biosensor phase sensitivity measurements compared to conventional gold thin film configurations. The enhanced sensitivity originates from optimized interaction between dielectric waveguide modes and plasmonic oscillations supported by thin metallic layers. These results illustrate that the optical response of multilayer systems cannot be understood solely through individual material properties because the entire electromagnetic structure determines field distribution and resonance behaviour.

4.3 Fano resonances and resonant multilayer architectures

Fano-resonant multilayer systems provide another example of how optical architecture governs functional properties. Fano resonances arise from interference between narrow discrete resonant states and broader continuum modes, producing highly asymmetric spectral profiles with sharp angular or spectral selectivity. In chromium-based multilayer stacks, hybridization of waveguide and surface electromagnetic modes enables formation of narrow resonances with sub-milliradian angular widths [D]. The resonance characteristics depend critically not only on chromium thickness, but also on the surrounding dielectric stack, incidence geometry, polarization conditions, and prism coupling configuration. Small variations in incidence angle or refractive index substantially shift resonance positions, demonstrating high sensitivity to the environment and suitability in sensor applications.

Importance of overall optical architecture becomes especially evident in resonant systems due to electromagnetic coupling between all structural components. Prism materials, dielectric thicknesses, interface roughness, and external optical alignment all contribute directly to final resonance and sensor sensitivity further described in publication [D].

4.4 Multilayer structures in high-power and space optics

The importance of multilayer architecture becomes evident in practical high-power laser and space optical systems, where optical coatings must simultaneously satisfy optical, thermal, and mechanical requirements. In these applications, the substrate itself becomes an active functional component rather than merely a mechanical support. High-reflectivity mirrors exposed to elevated optical power densities experience substantial thermal loading caused by residual absorption inside metallic or dielectric layers. If heat is not efficiently dissipated, local temperature gradients may induce stress, coating degradation, resonance drift, or catastrophic optical damage. Consequently, multilayer coating performance strongly depends on substrate thermal conductivity, mechanical stability, and cooling capability.

Additive manufacturing technologies enable fabrication of lightweight actively cooled mirror substrates with complex internal geometries optimized for thermal management [C]. However, surfaces produced by selective laser melting initially possess relatively high roughness and microstructural defects unsuitable for high-quality optical applications. Subsequent polishing and deposition of reflective multilayer coatings therefore become necessary to achieve the required optical performance. Investigations of silver–aluminium coated actively cooled mirrors demonstrated that the combination of substrate engineering, polishing processes, and optimized thin film deposition enables fabrication of lightweight mirrors with reflectance exceeding 95% in visible and infrared spectral ranges [C]. These results highlight that long-term optical performance depends not only on coating materials themselves, but on integration between multilayer coatings and thermally optimized substrate architectures.

4.5 Protective layers and interface engineering

Protective layers constitute another essential aspect of multilayer thin film systems. Many high-performance optical materials possess limited environmental stability when directly exposed to atmosphere, humidity, radiation, or chemically reactive environments. Silver, despite its superior optical reflectance, readily degrades due to oxidation and sulfur contamination. Protective dielectric overlayers are therefore frequently employed to isolate metallic films from environmental exposure while preserving optical performance. Ultrathin alumina coatings deposited by atomic layer deposition provide one example of such protection strategies because they form dense conformal barriers capable of suppressing degradation processes without substantially affecting optical behaviour [A]. Similarly, dielectric encapsulation layers may improve resistance to thermal cycling, ion irradiation, and mechanical wear in space optical systems.

Multilayer protection strategies also influence optical performance through modification of electromagnetic boundary conditions. Even nanometer-scale dielectric overlayers may shift resonance frequencies, alter plasmon coupling efficiency, or modify interference conditions. As a result, protective coatings cannot be treated as purely passive elements because they participate directly in formation of the final optical response. In resonant photonic structures, optimization of protective layers therefore requires simultaneous consideration of environmental durability and electromagnetic functionality [E].

Interface quality represents one of the most critical factors determining multilayer optical performance. Roughness, interdiffusion, and crystallographic disorder at interfaces introduce scattering losses and reduce coherence between reflected waves. In resonant systems, such imperfections may broaden spectral resonances and reduce sensitivity. Interface engineering therefore becomes increasingly important as device complexity and resonance sharpness increase.

5. SENSORS - OPTICAL SENSOR SENSITIVITY AND LIMITATIONS.

5.1 Fundamentals of optical sensing and refractive index sensitivity

Optical sensors play important role in modern measurement technologies because they enable non-contact, high-sensitivity detection of physical, chemical, and biological phenomena. Continuous improvements in sensor sensitivity directly expand the limits of detection, measurement precision, and analytical capability in fields ranging from biomedical diagnostics and environmental monitoring to aerospace communication and quantum technologies. Among the broad variety of sensing approaches, optical sensors occupy a particularly important position due to their non-contact operation, high sensitivity, fast response time, immunity to electromagnetic interference, and compatibility with remote and miniaturized systems. The performance of optical sensors is strongly influenced by the interaction between electromagnetic radiation and matter, making optical material properties, multilayer architectures, and resonance phenomena central factors determining sensing capability.

Many modern optical sensors operate by detecting changes in refractive index near an optically active surface. In such systems, molecular adsorption or environmental variation modifies the local dielectric environment, producing measurable shifts in optical parameters such as resonance angle, resonance wavelength, phase response, transmission intensity, or polarization state. The sensitivity of refractive index sensors is commonly quantified in refractive index units (RIU), typically expressed as angular sensitivity (deg RIU^{-1}), wavelength sensitivity (nm RIU^{-1}), or phase sensitivity depending on the interrogation method. High sensitivity corresponds to large measurable optical changes caused by very small refractive index variations. However, practical sensor performance depends not only on nominal sensitivity values, but also on resonance linewidth, signal-to-noise ratio, system stability, and detection methodology.

5.2 Surface plasmon resonance sensors and resonance linewidth limitations

Surface plasmon resonance sensors represent one of the most widely used classes of optical refractive index sensors. These systems rely on excitation of collective electron oscillations at a metal–dielectric interface, typically employing thin gold films due to their chemical stability and relatively low optical losses. Under appropriate optical conditions, incident light couples to a surface plasmon mode, producing a sharp resonance minimum in reflected intensity. Changes in the surrounding refractive index alter the plasmon propagation conditions and shift the resonance position, enabling highly sensitive detection of molecular interactions or environmental changes.

The performance of plasmonic sensors is strongly determined by resonance sharpness. Resonance width is commonly characterized using the full width at half maximum (FWHM), which defines the angular or spectral width of the resonance peak measured at half of its maximum intensity. Narrower resonances provide steeper resonance slopes and therefore larger signal changes for small resonance shifts. This effect becomes particularly important in fixed-angle interrogation methods, where sensing is performed by monitoring intensity variation at a constant angle of incidence positioned on the steep resonance edge. Under these conditions, a narrow resonance with high angular gradient produces significantly larger signal modulation compared to a broader resonance, even if both structures exhibit similar resonance shifts. Consequently, sensor performance is often governed not only by absolute resonance displacement, but by the ratio between resonance shift and resonance linewidth. These resonance formation mechanisms and linewidth optimization strategies were investigated in detail in publications [D, E].

5.3 Phase-sensitive sensing and multilayer plasmonic enhancement

The relationship between resonance sharpness and sensitivity is especially important in phase-sensitive and ellipsometric sensing methods. Total internal reflection ellipsometry enables simultaneous measurement of amplitude and phase variations associated with plasmonic resonances. Because optical phase changes occur extremely rapidly near resonance conditions, ellipsometric interrogation may achieve substantially higher sensitivity than conventional intensity-based detection. Our developed silver-based multilayer plasmon waveguide resonance structures demonstrated significantly higher sensitivity than conventional single-layer gold sensors in fixed angle ellipsometric measurements [E]. The improved performance originates from stronger electromagnetic field confinement and formation of sharper resonant features supported by coupling between plasmonic and dielectric waveguide modes. Such multilayer architectures enable resonance narrowing and increased phase sensitivity, allowing detection of smaller refractive index variations than achievable with classical gold-based plasmonic systems.

Although gold remains the dominant material in commercial plasmonic sensors due to its chemical inertness and stable optical properties, it possesses several limitations. Gold exhibits higher optical losses and broader plasmon resonances compared to silver, reducing resonance sharpness and limiting achievable field enhancement. Silver provides lower damping and sharper resonant behaviour, making it theoretically superior for high-sensitivity plasmonic sensing. However, practical application of silver is restricted by its lower environmental stability and susceptibility to oxidation or sulfur contamination. Consequently, advanced multilayer structures and protective coatings are often required to preserve the optical advantages of silver while improving long-term stability. Such approaches demonstrate that sensor optimization frequently requires balancing intrinsic optical performance with technological durability.

5.4 Fabrication limitations and influence of thin film quality

Sensor sensitivity is additionally limited by fabrication imperfections and structural non-uniformity. Surface roughness, grain boundaries, thickness fluctuations, and interface defects broaden resonances and increase optical scattering losses, thereby reducing measurement precision. In plasmonic systems, nanometer-scale roughness may significantly alter local electromagnetic field distribution and reduce reproducibility between fabricated devices. The quality of ultrathin metallic layers therefore becomes critically important for high-performance sensing applications. Investigations of sputtered silver films demonstrated that film continuity and surface morphology strongly influence optical response during the coalescence process [A]. Precise control of deposition parameters and thin film growth is therefore essential for achieving stable and reproducible sensor characteristics.

The surrounding optical architecture also strongly influences sensor performance. Prism coupling geometry, substrate refractive index, polarization state, illumination coherence, and incidence angle all contribute to resonance formation and measurement sensitivity. In resonant optical systems, small variations in alignment or optical path quality may significantly affect signal stability and measurement accuracy. Consequently, the performance of optical sensors depends not only on the sensing layer itself, but on the quality of the entire optical system guiding light toward the detector.

5.5 Sensor stability and system-level optical considerations

This broader systems perspective becomes particularly important in space optics and high-precision optical communication systems, where optical elements located before the sensing stage may influence signal quality. Mirrors, beam steering components, and protective optical coatings determine wavefront quality, scattering losses, and signal-to-noise ratio reaching the detector. High-reflectivity actively cooled silver mirrors developed using additive manufacturing and optimized coating technologies demonstrate how thermal stability and optical surface quality become essential for maintaining stable optical performance under elevated power loads [C]. Efficient thermal management reduces optical distortions caused by local heating, thereby preserving beam quality and long-term operational stability in optical communication systems.

Similarly, low-roughness Ag–Al mixed coatings developed for space applications demonstrate the importance of coating morphology and environmental durability for optical instrumentation [B]. In telescopes, imaging systems, and free-space optical communication devices, even small scattering losses introduced by surface roughness or degradation may substantially reduce signal intensity and measurement precision. Optical coatings therefore contribute not only to reflection efficiency, but also to overall sensor system sensitivity by preserving wavefront integrity and minimizing parasitic optical losses before light reaches the active sensing element.

Another important limitation of optical sensors arises from the trade-off between sensitivity and operational stability. Extremely sharp resonances provide high sensitivity but may simultaneously increase susceptibility to thermal drift, mechanical vibrations, and fabrication tolerances. Narrow resonances are highly responsive to refractive index changes, but also to unintended environmental fluctuations. As a result, practical sensor development requires optimization between maximum theoretical sensitivity and stable real-world operation. This balance is especially important in biosensing applications, where reliable long-term measurements often become more valuable than achieving the absolute highest sensitivity under ideal laboratory conditions.

Overall, optical sensor sensitivity emerges from a interaction between resonance physics, thin film quality, material selection, multilayer architecture, and overall optical system design. Parameters such as refractive index sensitivity, resonance linewidth, FWHM, phase response, and signal stability collectively determine practical sensing performance. Advanced multilayer plasmonic structures employing optimized silver-based coatings demonstrate that substantial improvements beyond classical gold sensors can be achieved through precise engineering of electromagnetic field confinement and resonance sharpness. At the same time, the quality of surrounding optical components, including mirrors, substrates, and protective coatings, remains equally important because the entire optical pathway contributes to final system sensitivity, stability, and measurement precision. The challenges discussed in this section were investigated and presented in publications [A–E].

6. OPTICAL SENSOR STRUCTURE FOR BIO APPLICATIONS.

6.1 Fundamentals of optical biosensors [E]

Optical biosensors are designed to detect biological interactions through changes in optical properties occurring near a sensing surface. Their operation is based on biomolecular binding events modifying the local refractive index at the interface between the sensor surface and the biological medium. These refractive index variations alter the propagation conditions of electromagnetic modes supported by the optical structure, producing measurable changes in resonance angle, wavelength, phase, polarization state, or reflected intensity. Because optical methods enable label-free, real-time, and highly sensitive measurements, optical biosensors have become important tools in medical diagnostics, pharmaceutical analysis, environmental monitoring, and investigation of biomolecular interactions.

The performance of optical biosensors is determined primarily by the structure supporting electromagnetic field localization near the sensing interface. Efficient sensing requires strong overlap between the evanescent electromagnetic field and the biological medium because only the field portion extending into the analyte region can interact with biomolecules attached to the sensor surface. For this reason, most modern biosensors employ resonant optical structures capable of generating highly localized electromagnetic fields and narrow optical resonances sensitive to refractive index variations.

6.2 Classical surface plasmon resonance biosensors

Classical surface plasmon resonance biosensors are among the most widely used optical sensing platforms. In these systems, a thin metallic layer, typically gold with thickness near 50 nm, is deposited on a prism substrate operating in Kretschmann configuration. Under specific incidence angle and polarization conditions, incident light couples to a propagating surface plasmon mode at the metal–dielectric interface, producing a sharp minimum in reflected intensity. Binding of biological molecules near the metal surface changes the local refractive index and shifts the resonance position, enabling quantitative analysis of biomolecular interactions. Gold remains the dominant plasmonic material because of its chemical stability, resistance to oxidation, and compatibility with biological functionalization processes.

Despite their widespread use, classical gold-based sensors possess several limitations. Gold exhibits relatively high optical damping compared to silver, resulting in broader resonances and lower electromagnetic field confinement. Broader resonances reduce angular sensitivity and limit the achievable signal-to-noise ratio, particularly in fixed-angle or phase-sensitive interrogation schemes. In addition, conventional single-layer plasmonic sensors support only one dominant surface plasmon mode, restricting possibilities for engineering field distribution and resonance characteristics. As a result, significant research efforts have focused on development of multilayer plasmonic structures capable of supporting sharper resonances and stronger field enhancement.

6.3 Multilayer plasmon-waveguide biosensor structures

One approach for improving sensor sensitivity involves coupling plasmonic modes with dielectric waveguide resonances inside multilayer metal–dielectric structures. Such hybrid systems support simultaneous excitation of surface plasmons and guided electromagnetic modes, producing stronger field localization and narrower resonant features compared to classical plasmonic sensors. The development of chromium-based Fano-resonant multilayer structures demonstrated that interference between resonant electromagnetic states may generate extremely sharp angular resonances with sub-milliradian linewidths [D]. These investigations showed that carefully engineered multilayer architectures are capable of supporting highly sensitive optical responses governed not only by plasmonic behaviour, but also by mode hybridization and resonance interference effects.

The sharp asymmetric resonances observed in chromium-based multilayer systems provided conceptual motivation for development of multilayer biosensor architectures employing similar resonant principles but optimized for biological sensing applications. Instead of using chromium primarily as an absorbing resonant layer, subsequent sensor designs incorporated silver-based multilayer structures capable of supporting plasmon waveguide resonances with lower optical losses and stronger electromagnetic confinement [E]. The resulting multilayer biosensor architecture combines thin metallic films with dielectric layers designed to support coupled resonant modes, enabling substantial improvement of sensitivity compared to conventional single-layer gold sensors.

In the developed plasmon waveguide resonance structures, the dielectric multilayer plays an active role in electromagnetic field engineering rather than serving merely as a passive substrate. The dielectric stack modifies optical dispersion conditions and enables coupling between guided waveguide modes and surface plasmons supported by the metallic layer. This interaction produces sharper resonances and stronger local electromagnetic fields extending into the biological medium. As a consequence, even small refractive index changes caused by biomolecular adsorption generate larger measurable optical responses. Experimental investigations demonstrated that such multilayer structures significantly enhance sensitivity in total internal reflection ellipsometry measurements compared to conventional gold-based plasmonic sensors [E].

6.4 Material selection and interrogation methods [E]

The choice of silver instead of gold was motivated primarily by its plasmonic properties. Silver exhibits lower optical losses and supports narrower resonances due to reduced electron damping in the visible spectral range. Narrower resonances produce steeper angular and phase gradients, improving sensitivity particularly in phase-sensitive interrogation methods. However, silver also presents technological challenges related to oxidation and environmental degradation. For this reason, multilayer sensor architectures often require additional protective or stabilizing layers capable of preserving optical performance while maintaining efficient plasmonic coupling.

Measurement methodology represents another important aspect of biosensor structure design. Conventional surface plasmon resonance systems typically employ intensity interrogation, where resonance shifts are monitored through changes in reflected intensity as a function of angle or wavelength. While such methods are relatively simple and robust, their sensitivity is limited by resonance linewidth and detector noise.

Ellipsometric interrogation methods provide higher sensitivity because they simultaneously measure amplitude and phase changes associated with optical resonances. Near resonance conditions, optical phase may vary extremely rapidly with refractive index, enabling detection of very small environmental changes. Total internal reflection ellipsometry therefore represents a particularly attractive approach for multilayer plasmon waveguide resonance sensors because the sharp resonances supported by these structures generate strong phase responses [E].

6.5 Alternative biosensor structures and fabrication considerations

Various alternative optical biosensor types have been developed depending on application requirements. Interferometric sensors employ phase differences between optical paths to detect refractive index changes with extremely high precision. Ring resonators and photonic crystal sensors rely on wavelength-selective resonant modes confined inside dielectric microstructures. Localized surface plasmon resonance sensors use metallic nanoparticles instead of continuous films, enabling compact sensing geometries and strong near-field enhancement. Optical waveguide sensors detect changes in guided mode propagation caused by interaction with surrounding media. Although these approaches differ in physical principles and geometry, they all rely on maximizing electromagnetic interaction between the optical field and biological analytes.

In practical biosensing systems, the quality of thin film deposition and interface engineering becomes critically important because resonance sharpness and field confinement strongly depend on layer thickness uniformity and surface roughness. Imperfections smaller than nanometer may broaden resonances, increase optical losses, and reduce measurement reproducibility. Consequently, fabrication technologies such as magnetron sputtering, ion beam spuutering and atomic layer deposition play essential roles in achieving stable and reproducible biosensor performance. Precise control of metallic layer continuity is particularly important for silver-based plasmonic structures because discontinuities and roughness strongly influence plasmon propagation and resonance quality.

The overall optical architecture surrounding the biosensor additionally influences measurement sensitivity and stability. Prism coupling geometry, substrate refractive index, polarization control, and optical alignment determine coupling efficiency between incident light and resonant electromagnetic modes. Since plasmon waveguide resonance structures operate through highly angle-sensitive optical phenomena, even small alignment deviations may affect resonance stability. As a result, biosensor performance emerges not only from the sensing layer itself, but from the interaction of the entire optical system.

7. OPTICS AND SENSORS IN SPACE APPLICATIONS.

7.1 Optical systems and environmental challenges in space

Optical systems play important role in modern space technologies because electromagnetic radiation represents the primary carrier of information in remote sensing, astronomical observation, navigation, Earth monitoring, and free-space optical communication. Unlike terrestrial systems, space optical instruments operate in an environment characterized by vacuum conditions, strong radiation exposure, extreme thermal cycling, micrometeoroid impacts, and long-term absence of maintenance. Under such conditions, the reliability and durability of optical coatings become equally as important as their initial optical performance. As a result, modern space optics require thin film structures capable of maintaining stable reflectance, transmission, resonance behaviour, and surface quality throughout prolonged operation under harsh environmental conditions.

Thin film optical coatings are essential components of virtually all space optical systems. Metallic and dielectric multilayers are used in mirrors, beam splitters, filters, sensors, detectors, solar panels, thermal control surfaces, and laser communication systems. Their functionality depends on precise control of optical interference, absorption, reflection, and electromagnetic field confinement. However, optical properties optimized under laboratory conditions may substantially degrade in space due to radiation-induced defects, thermal stress accumulation, surface contamination, and structural instability. Consequently, the design of space optical coatings requires simultaneous optimization of optical efficiency, mechanical robustness, thermal stability, and environmental resistance.

7.2 Thermal cycling and mechanical stability of optical coatings

One of the most important challenges for space optical systems is thermal cycling. Spacecraft components are repeatedly exposed to rapid temperature variations caused by alternating solar illumination and shadow conditions during orbital motion. Depending on mission geometry and location, optical surfaces may experience temperature changes ranging from cryogenic conditions to several hundred degrees Celsius. Repeated expansion and contraction of thin film layers under such conditions generate mechanical stress at material interfaces. Because multilayer coatings are typically composed of materials with different thermal expansion coefficients, thermal cycling may induce cracking, delamination, roughness evolution, or gradual degradation of interface quality. Even less than nanometer-scale structural changes may significantly affect optical performance in resonant or interference-based systems.

Thermal stability becomes particularly critical in high-reflectivity mirrors and laser communication optics where local heating caused by residual absorption may further amplify stress accumulation. Metallic coatings such as silver provide exceptionally high reflectance in visible and infrared spectral regions, making them attractive for space mirrors and free-space optical communication systems. However, pure silver films possess relatively poor environmental stability and may undergo morphological degradation during prolonged thermal exposure. Grain growth, surface diffusion, and interface instability can increase roughness and optical scattering losses, reducing mirror efficiency and beam quality. For this reason, alloying and multilayer protection strategies are frequently employed to improve thermal and structural stability while preserving high reflectance.

Silver–aluminium mixed coatings demonstrate one approach for enhancing durability of reflective optical systems intended for space applications [B]. Aluminium incorporation modifies film microstructure and suppresses excessive grain coalescence, resulting in smoother surfaces and improved resistance to degradation processes. Experimental investigations showed that Ag–Al coatings maintain high reflectance while exhibiting improved stability under simulated space environmental conditions [B]. Reduced surface roughness is particularly important for precision optical systems because roughness-induced scattering directly degrades wavefront quality and decreases optical signal efficiency. In astronomical instruments and long-distance optical communication systems, even relatively small scattering losses may substantially reduce system sensitivity and transmission performance.

7.3 Radiation effects on thin film optical coatings

Radiation exposure represents another challenge for space optical coatings. Outside the protective atmosphere of Earth, optical systems are continuously exposed to energetic protons, electrons, ultraviolet radiation, and cosmic particles capable of modifying material structure at atomic and nanoscale levels. Radiation-induced defects may alter refractive indices, increase optical absorption, modify crystallographic structure, and accelerate degradation processes. Metallic layers may experience defect accumulation, interface diffusion, and morphological instability, while dielectric layers may develop color centers or localized structural damage affecting transparency and resonance conditions.

Proton irradiation is especially relevant for optical systems operating in low earth orbit, but also in deep-space environments. Energetic particles penetrate thin film structures and transfer energy through atomic collisions, producing vacancies, interstitial defects, and local structural disorder. Such defects may increase electron scattering and modify dielectric permittivity, thereby reducing reflectance and increasing optical losses. Investigations of silver–aluminium mirrors under proton irradiation demonstrated that alloyed coatings exhibit improved resistance to radiation-induced degradation compared to pure silver films (Figure 6) [B]. Enhanced radiation stability is associated with improved structural homogeneity and reduced susceptibility to defect-driven morphological evolution. These results demonstrate that material composition optimization may significantly improve long-term optical reliability in space environments.

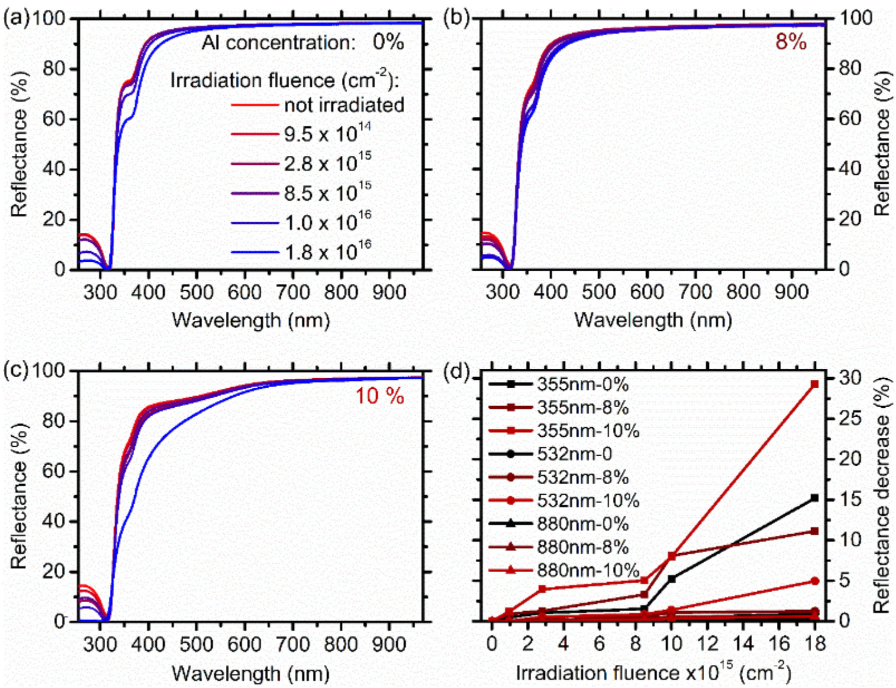

Figure 6. Reflectance spectra of Ag-Al mixed films with a) 0%, b) 8% and c) 10% Al concentration before and after the irradiation. d) summary of Ag-Al mixed films reflectance caused by the irradiation at various wavelengths.

Vacuum conditions additionally influence thin film stability because absence of atmospheric pressure enhances surface diffusion and desorption processes. Although vacuum eliminates oxidation mechanisms commonly present under terrestrial conditions, it may accelerate structural relaxation and diffusion-driven morphological changes in thin metallic layers. Furthermore, contamination caused by outgassing of spacecraft materials may deposit molecular films onto optical surfaces, altering transmission and reflectance properties. Such contamination becomes particularly problematic for ultraviolet and infrared optical systems where even extremely thin contaminant layers may introduce substantial absorption losses.

7.4 Protective coatings for space optics

Protective coatings are therefore widely used in space optics to isolate sensitive metallic layers from environmental exposure. Dielectric overcoats may provide chemical stability, suppress diffusion processes, and improve resistance to radiation and thermal cycling. Atomic layer deposition techniques are particularly attractive for such applications because they enable conformal formation of dense nanoscale protective layers with excellent thickness control. Alumina protective coatings deposited on ultrathin silver films have demonstrated improved environmental durability while preserving optical functionality [A]. Properly engineered protection layers may therefore significantly extend operational lifetime of high-performance optical coatings in space environments.

The importance of optical coatings in space systems extends beyond passive mirrors and filters toward advanced optical sensing and communication technologies. Optical sensors used for satellite positioning, Earth observation, environmental monitoring, and astronomical instrumentation require highly stable optical characteristics and low-noise operation. Resonant optical structures employed in sensors are especially sensitive to temperature fluctuations and material degradation because small variations in refractive index or layer thickness may shift resonance conditions and reduce measurement precision. Consequently, thermal stability and radiation resistance are essential not only for preserving optical throughput, but also for maintaining calibration stability and sensing accuracy.

7.5 Space optical communication and actively cooled mirrors

Free-space optical communication systems place demanding requirements on optical coatings because signal transmission efficiency directly depends on mirror reflectivity, surface roughness, and thermal stability. High-power laser beams used in optical communication generate localized heating within optical components, potentially producing thermal lensing, deformation, or coating damage. Lightweight actively cooled mirrors manufactured using additive manufacturing technologies provide one approach for addressing these challenges [C]. Internal cooling channels integrated within the mirror substrate enable efficient heat dissipation while maintaining low structural mass. Combined with optimized reflective coatings, such structures allow stable operation under elevated optical power densities while preserving high reflectance and beam quality.

Surface quality is equally critical in space telescopes and imaging systems because optical scattering caused by roughness or coating degradation reduces image contrast and signal sensitivity. Nanometer-scale imperfections may broaden point spread functions and introduce parasitic stray light, limiting performance of high-resolution imaging instruments. For this reason, deposition uniformity, polishing quality, and multilayer interface control remain fundamental requirements in fabrication of space optical coatings.

Overall, optical coatings used in space applications must function simultaneously as electromagnetic, mechanical, thermal, and environmental protection systems. Their performance is governed not only by intrinsic optical properties, but also by resistance to radiation damage, thermal stress, vacuum-induced degradation, and long-term morphological evolution. Advanced multilayer architectures employing optimized metallic films, dielectric protection layers, and thermally engineered substrates provide pathways toward stable high-performance optical systems capable of operating under the extreme conditions of space environments. Understanding the interaction between optical functionality and environmental durability is therefore essential for the development of next-generation space communication systems, astronomical instruments, optical sensors, and precision reflective components.

8. HIGH POWER LASER OPTICS.

8.1 Requirements for high power laser optical systems

High power laser systems impose demanding requirements on optical materials and thin film coatings because even small optical losses may generate substantial thermal loading under elevated radiation intensities. Optical components operating in high power laser environments must simultaneously maintain high reflectance or transmission, low absorption, dimensional stability, resistance to thermal deformation, and long operational lifetime. Under such conditions, the performance of the optical coating cannot be separated from the properties of the substrate and overall mechanical structure. The optical layer, substrate material, thermal management system, and surface quality together form an integrated opto-thermo-mechanical system whose stability determines the final performance of the laser optics.

One of the primary challenges in high power laser optics is residual absorption inside thin film coatings. Even highly reflective metallic or dielectric mirrors absorb a small fraction of incident optical energy. At low optical powers such absorption may be negligible, but at powers above kilowatt-level irradiation localized heating becomes significant. Temperature gradients generated inside the coating and substrate induce thermal expansion, mechanical stress, and refractive index variations (Figure 7). These effects may distort the optical wavefront, shift resonance conditions, increase scattering losses, and ultimately lead to coating damage or substrate failure. Consequently, minimizing optical absorption is one of the most critical requirements for high-power laser coatings.

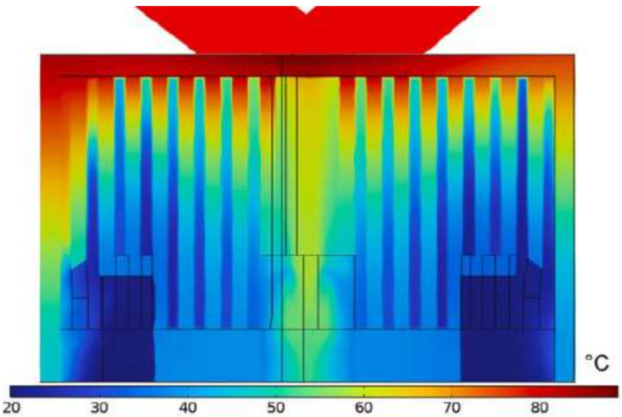

Figure 7. Temperature and airflow distribution of actively cooled metallic mirror at 2000 W laser beam power, 10 mm spot size and 95 % reflectance. [C]

8.2 Metallic coatings and morphology optimization

In high-power laser systems, the long-term stability of reflective coatings becomes as important as their initial optical performance. Although metallic mirrors may exhibit high reflectance, residual absorption inevitably generates heat that can modify coating morphology, increase surface roughness, and reduce beam quality during operation or even cause thermal damage to the coating. Consequently, optimization of microstructure and suppression of thermally induced degradation represent key challenges in the development of high-power laser optics.

Smoother surfaces minimize diffuse scattering and preserve wavefront quality, while dense homogeneous microstructures improve thermal stability and reduce defect formation. Alloying approaches such as incorporation of aluminium into silver coatings provide one strategy for improving structural stability while preserving high reflectance [B]. Ag–Al mixed films exhibit reduced surface roughness and improved resistance to degradation processes compared to pure silver layers, making them more suitable for demanding optical environments involving elevated thermal or radiation loads. Improved morphological stability also contributes to more uniform thermal distribution within the coating, reducing the probability of localized overheating.

8.3 Importance of substrate materials and thermal management

Although coating properties are critically important, the substrate itself often determines the ultimate thermal performance of high-power optical systems. Heat generated inside the optical coating must be efficiently transferred away from the irradiated region to prevent accumulation of thermal stress and deformation. Substrate materials with high thermal conductivity, low thermal expansion, and good mechanical stability are therefore preferred for high-power laser optics. Materials such as copper, silicon carbide, aluminium alloys, and specialized ceramics are commonly employed because they enable rapid heat dissipation while maintaining structural rigidity.

In many modern laser systems, passive thermal conduction alone is insufficient for maintaining stable optical performance. Active cooling systems are therefore integrated directly into optical components to continuously remove heat during operation. Actively cooled mirrors employ internal cooling channels through which liquid or gas coolants circulate, enabling efficient thermal management under high optical loads. Such systems significantly reduce temperature gradients and suppress thermally induced deformation. However, integration of active cooling introduces additional technological challenges because the substrate geometry must simultaneously satisfy thermal, mechanical, and optical requirements.

Thermal deformation represents one of the most critical limitations in high-power optical systems because even submicrometer surface distortions may significantly degrade beam quality. Laser-induced heating causes local expansion of both coating and substrate materials, producing curvature changes and optical aberrations. Thermal gradients may additionally induce stress accumulation at coating interfaces due to differences in thermal expansion coefficients between multilayer components. Repeated thermal cycling may therefore gradually degrade adhesion and structural integrity of optical coatings.

8.4 Additive manufacturing and lightweight mirror structures

Additive manufacturing technologies provide new possibilities for fabrication of lightweight actively cooled optical substrates with complex internal cooling geometries impossible to achieve using conventional machining methods. Selective laser melting enables production of metal mirror structures containing integrated cooling channels optimized for uniform heat extraction and reduced structural mass. Nevertheless, surfaces produced by additive manufacturing initially possess relatively high roughness and microstructural irregularities incompatible with precision optical applications. Extensive post-processing including polishing and thin film coating deposition is therefore required to achieve optical-quality surfaces.

Investigations of actively cooled metallic mirrors manufactured using additive technologies demonstrated that the combination of substrate engineering, polishing optimization, and reflective thin film deposition enables fabrication of high-reflectivity laser mirrors suitable for demanding optical applications [C]. Deposition of Ag–Al reflective coatings onto polished additively manufactured substrates produced mirrors with reflectance exceeding 95% across visible and infrared spectral ranges while maintaining relatively low surface roughness [C]. These results demonstrate that optical performance depends not only on intrinsic coating reflectivity, but also on the interaction between substrate topology, thermal management, and coating morphology (Figure 8).

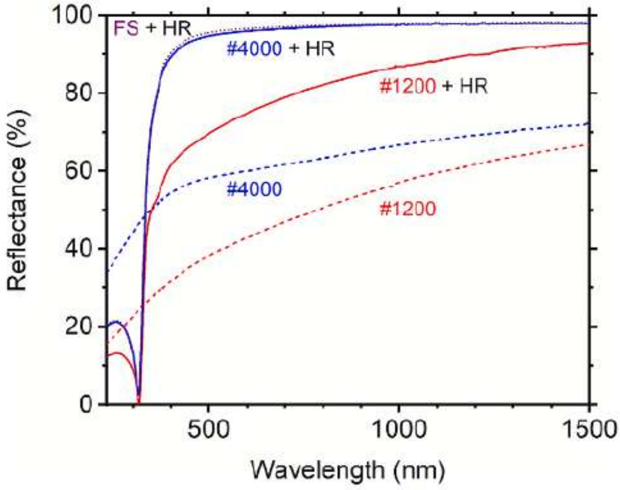

Figure 8. Reflectance spectra of Selective laser melted metal mirror, polished with #1200 grit and #4000 grit before and after high reflective (HR) coating deposition. Spectra of HR coated double-sided optically polished fused silica (FS) substrate are shown as reference. [C]

Thermal deformation represents one of the most critical limitations in high-power optical systems because even submicrometer surface distortions may significantly degrade beam quality. Laser-induced heating causes local expansion of both coating and substrate materials, producing curvature changes and optical aberrations. In resonant laser systems, such distortions may alter cavity alignment and reduce operational stability. Thermal gradients may additionally induce stress accumulation at coating interfaces due to differences in thermal expansion coefficients between multilayer components. Repeated thermal cycling may therefore gradually degrade adhesion and structural integrity of optical coatings. Threrfore, to minimise temperature gradients active cooled mirror substrate structures can be implemented (Figure 9) [C].

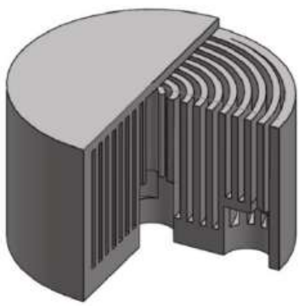

Figure 9. Isometric cross section view of active cooled metallic mirror substrate structure [C].

The importance of substrate engineering becomes even greater in applications involving ultrafast or high-energy pulsed lasers. In such systems, extremely high peak intensities may generate rapid transient heating and nonlinear optical effects within thin film layers. Localized defects, contamination particles, or surface imperfections may concentrate electromagnetic fields and initiate catastrophic optical damage. Consequently, high-power laser optics require exceptionally low defect density and high surface quality. Smaller than few nanometer scale surface roughness control becomes essential not only for minimizing scattering losses but also for preventing local intensity enhancement responsible for laser-induced damage initiation.

8.5 Dielectric multilayers, hybrid coatings, and environmental stability

Dielectric multilayer mirrors are widely used in high-power laser systems because they can achieve high reflectance with very low absorption. However, dielectric coatings are typically optimized for narrower spectral and angular ranges than metallic mirrors. In broadband or dynamically varying laser systems, metallic coatings may therefore remain advantageous despite their somewhat higher absorption. Hybrid multilayer architectures combining metallic and dielectric layers are often employed to balance broadband performance, thermal stability, and environmental durability.

Environmental resistance additionally becomes important because high-power laser optics may operate in vacuum systems, industrial environments, or space conditions where contamination and thermal cycling accelerate degradation processes. Protective dielectric overlayers are frequently used to isolate reflective metallic coatings from oxidation, contamination, and mechanical wear. Such protective layers must simultaneously preserve low optical absorption and maintain strong adhesion under thermal loading conditions.

COPIES OF PUBLICATIONS INCLUDED IN THE THESIS

A. Ultrathin sputtered silver films protected by ALD alumina: Comparison of in-situ investigation with ex-situ resistance and ellipsometric measurements

A. Belosludtsev, A. Sytchkova, N. Kyžas, I. Bitinaitis,
R. Simniškis, R. Drazdys

Vacuum 195 (2022) 110669

Contents lists available at ScienceDirect

Vacuum

journal homepage: www.elsevier.com/locate/vacuum

Ultrathin sputtered silver films protected by ALD alumina: Comparison of in-situ investigation with ex-situ resistance and ellipsometric measurements

Alexandr Belosludtsev [a,**], Anna Sytchkova [b,*], Naglis Kyžas [a,1], Ignas Bitinaitis [a], Rimantas Simniškis [a], Ramutis Drazdys [a]

[a] Center for Physical Sciences and Technology, Savanoriu ave. 231, Vilnius, 02300, Lithuania
[b] Optical Coatings Group, ENEA Casaccia, Via Anguillarese 301, Rome, 00123, Italy

ARTICLE INFO

Keywords:
Metal film growth
Silver
Ellipsometry
Optical properties
Sputtering
ALD

ABSTRACT

We compare *in-situ* transmittance and plasma emission spectra with *ex-situ* resistance and ellipsometric measurements performed on ultrathin silver films with thicknesses varying from 3 nm through 40 nm and on relatively thick layers up to 100 nm. We show that the transmittance broadband monitoring (BBM) of the growing silver layer allows for *in-situ* reliable estimation of the minimum thickness when the film becomes continuous. Moreover, a proper selection of the monitoring wavelength(s) renders the coalescence and percolation stages of the film growth clearly distinguishable. For our films deposited by magnetron sputtering on fused silica substrates, the minimum thickness when a film becomes continuous was found to be approximately 12 nm. The percolation threshold was determined as approximately 6 nm. The method of selective-wavelength transmittance BBM is practical, intuitive and hence may represent a useful tool enabling high-precision growth of ultrathin silver layers. Furthermore, we show here for the first time that ellipsometry is sensitive to the metal coalescence development. In particular, the ellipsometric analysis suggests that the percolation of silver sputtered films begins at the top of the growing layer and hence propagates towards the film bottom.

1. Introduction

The first studies on silver film growth mechanisms and on the percolation and resistivity of this metal date back to early 1950s, initially performed for evaporated [1] and right after for sputtered films [2]. Silver is one of the most studied thin film materials because of its technological importance, yet there are still open questions to answer and the research is in progress [3,4] aimed to obtain silver films of enhanced quality for many important applications. In optical applications, sputtered silver films are used in low-emissivity glasses [5,6], in mirror production [7–9], for sensing [7,10,11], as flexible transparent film heaters [12], as transparent conducting electrode [13–15], as transparent antenna [16,17], in optical filters [18] and many others.

In applications searching for ever lower optical losses, ever thinner layers are required. Precise determination of the optical parameters of ultrathin layers is important, while the material structure and morphology may vary for every deposition process. Therefore, reliable methodology of the optical characterization of ultrathin silver films is important, with particular emphasis on the physical meaning of the fitting results. Additionally, unprotected ultrathin silver films rapidly change their optical and electrical properties when exposed to a reactive environment. Various mechanisms of silver degradation are described in literature [19] and protection with thin dielectric films may be applied. For some applications, coating a silver layer with a dielectric film serves to render silver more transparent in a chosen spectral range [20,21]. When a silver film is coated by a dielectric layer, silver optical response varies, albeit such dielectric layer may be optically very thin.

Tracing changes of the film properties through proper chosen model parameters may provide additional insight into film growth and film properties. Initial ultrathin film growth can be investigated using various methods mentioned in the introduction in Refs. [22,23] and in the review [24].

Comparison of the experimental data is challenging for a number of reasons like film instability or contamination, difference in analysis

* Corresponding author.
** Corresponding author.
E-mail addresses: Alexandr.Belosludtsev@ftmc.lt (A. Belosludtsev), Anna.Sytchkova@enea.it (A. Sytchkova).
[1] Present address: Optogama UAB, Mokslininku st. 2A, Vilnius 08412, Lithuania.

https://doi.org/10.1016/j.vacuum.2021.110669
Received 20 July 2021; Received in revised form 6 October 2021; Accepted 7 October 2021
Available online 13 October 2021

approaches, etc. For example, material quality studied in Ref. [18] was compromised, because of partial oxidation of the metal films already in the deposition chamber due to residual oxygen (the base pressure values were of 3–5x10^{-5} Torr). Furthermore, authors suggested using a simple exponential function to fit the trend of transmission variation at several chosen wavelengths. Such approach has limitations and works only in the IR range and for relatively thick films, as we show here.

Previously, in Ref. [22], copper films were investigated *in-situ* and compared with spectrophotometric *ex-situ* spectrophotometric measurements. In that study, the optical constants for continuous films were taken from the literature. Here instead, the *in-situ* optical transmittance spectroscopy of silver is compared with the *ex-situ* results of resistance and ellipsometric measurements. The silver films were deposited on fused silica substrates by magnetron sputtering and protected by ~12 nm of alumina prepared by atomic layer deposition (ALD). Silver optical constants were analyzed starting from the stage of initial nanoparticles to the formation of a continuous film. A particularly detailed investigation was performed for films up to 40 nm thickness, in order to study the growth stages for the thicknesses below the electron mean free path in silver.

2. Experimental details

Silver films were prepared using an unbalanced magnetron source (Torus™ sputter gun) with planar circular targets (Ag, 99.99% purity) in a Kurt J. Lesker sputtering system (PVD225). Target diameter and thickness were 101.6 mm and 5 mm, respectively. It is well-known that silver degrades if even a little amount of atomic oxygen is present in the chamber during a deposition process. In order to avoid silver degradation, the system was initially pumped down to a base pressure below 3 × 10^{-7} Torr. The magnetron was driven by a pulsed DC power supply (Advanced Energy Pinnacle Plus). In this work, the repetition frequency was 100 kHz, the duty cycle was 80% and the fixed was 80 W. The argon (Ar, >99.999% pure) flow rate was 20 sccm and the pumping speed was adjusted to attain the argon pressure at the same value of 2.2 mTorr. The settings of the Ar flow rate and the pumping speed were not changed during the experiments. Prior every experiment, a target was pre-sputtered for 5 min to remove any surface impurities. The target-to-substrate distance was 230 mm. The system was equipped with magnetron and substrate shutters. The experiments were conducted at room temperature.

During the deposition, the film mass thickness was controlled by quartz crystal and optical broadband monitoring (BBM). The BBM transmittance spectra were real-time recorded in the 400–1000 nm wavelength range. For time-resolved Optical Emission Spectroscopy (OES) Nova Fabrica Ltd. Inteleg® 2B-PEM (Broad-band Plasma Emission Monitoring) system (Model Number: I2BPEM-341D015000) was used. The 2B-PEM detector covers spectral range of 200–1100 nm with 3 nm resolution. A fiber-optic optical monitoring assembly consisting of a focusing lens and a collimator tube was placed inside the process chamber. It collects the light originating from dense plasma 1 cm above the target surface while integrating light along the width of the plasma.

To prevent possible silver degradation, all samples were transferred in a separate ALD chamber right after the sputtering deposition and were covered with a ~12 nm-thick layer of aluminium oxide. ALD deposition was performed using cross-flow type Ultratech ALD reactor (Savannah S200). Nitrogen (purity 99,999%) was used as a carrier and as a purging gas at a constant flow of 20 sccm. Commercial trimethylaluminium (TMA) and deionized water were used as reactants. The pulse for TMA and water was of 0.02 s at a time. The duration of purge cycle of TMA and water excess and reaction products was 6 s. The reactor temperature during the deposition process was 150 °C. To obtain the desired layer thickness, 70 cycles were deposited. ALD technique provides an efficient way to form a coating protecting the sensitive surface of silver from a corrosive and oxidizing environment [25]. Aluminium oxide is known to protect silver well and to minimize silver diffusion through the

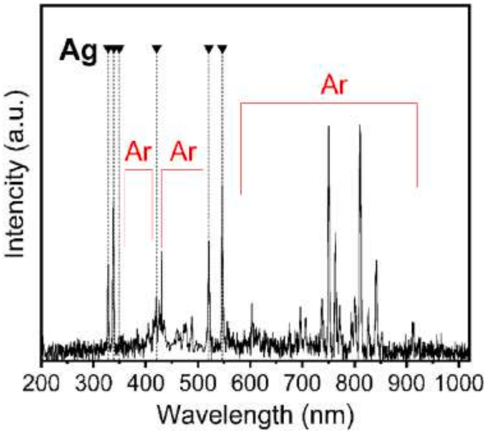

Fig. 1. Optical emission spectrum of Ag plasma.

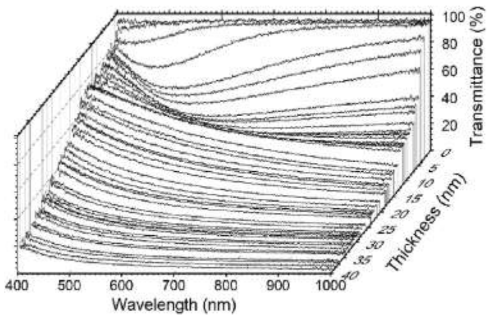

Fig. 2. Transmittance spectra evolution during silver film growth on fused silica substrate, recorded real-time *in-situ*.

protective layer [26,27]. In Ref. [28], it was calculated oxidation of selected metals. Qualitatively, the results show the preference of partially oxidized Al to form a stoichiometric oxide plus metal. In the case of Ag with low absorption energy, no convincing preference observed.

The thickness of relatively thick silver films (~100 nm) was measured *ex-situ* at the film edge by profilometry (Veeco Dektak 150).

To determine the optical constants of the films, ellipsometric measurements were performed using a J.A. Woolam VASE instrument in the spectral range 260–1500 nm, at three incidence angles 55°, 65° and 75°.

Surface resistance measurements were carried out applying the contactless microwave technique. More information about the measurement setup and calculations can be found in Ref. [29]. This method allows for a contactless non-destructive analysis of the electrical properties of metal films, even when they are fully coated with a protective dielectric layer.

3. Results and discussion

3.1. Evolution of growing silver films optical properties

To ensure silver film purity, an *in-situ* analysis of optical emission lines of Ag plasma was performed. In this method, characteristic

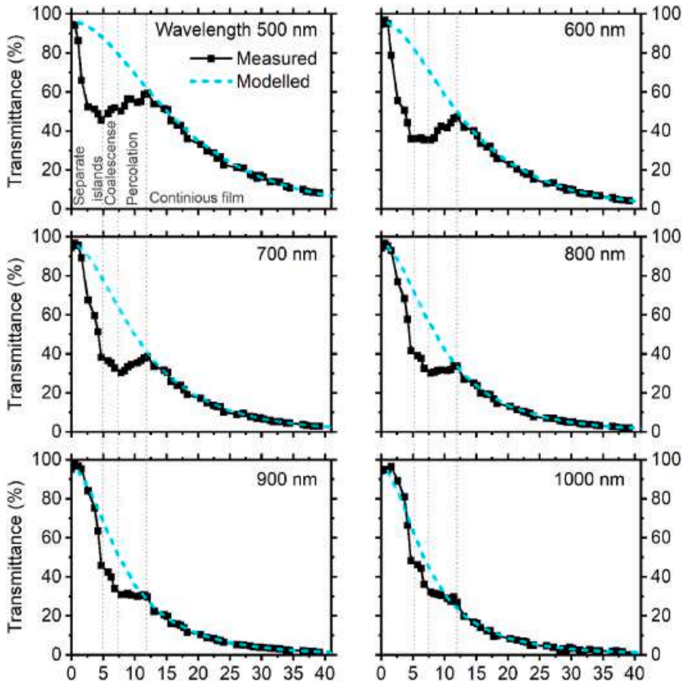

Fig. 3. Real-time *in-situ* transmittance values measured during silver growth at various wavelengths from 500 nm to 1000 nm. Measured and modeled transmittance values are shown, see text for details.

emission frequencies can be assigned to every single element. In Fig. 1, the intense silver emission lines are in the ultraviolet through green: at 328.1 nm [30,31], followed by 338.9 nm line [30,31], and further [31]: 349.5 nm, 421.1 nm, 520.9 nm, 546.6 nm and 547.2 nm. Other lines are related to Ar emission [31–34]. No oxygen lines or any other possible pollutant emission lines at this optical range were detected.

Dependence of the optical properties of silver films on the thickness is not monotonous. Fig. 2 illustrates the evolution of the film transmission measured *in-situ* in a broad wavelength range. The spectra were acquired at different stages of the film growth: separate islands first, followed by coalescence and percolation phases [35], and hence a continuous layer. It is well known that silver (as other noble metals) grows on oxide surfaces following Volmer-Weber mode [22]. For ultrathin silver films, the transmittance spectra maximum is at ~350 nm [23,36] and is a convenient spectral feature for silver film thickness monitoring. Although this wavelength is out of the range of our BBM setup, the evolution of the *in-situ* transmittance spectra with the increase of a silver film thickness is clearly seen.

The change of *in-situ* transmittance at several representative wavelengths is shown in Fig. 3. The monotonous curve signed as "Modeled" corresponds to modeled transmittance values of a silver continuous layer of a given thickness in assumption that the layer has the optical constants of "bulky" silver as retrieved *ex-situ* for the 100 nm-thick film. It is well seen that this function interprets closer the experimental data in the IR. Close to exponential behavior of the curve in the IR agrees with the observations reported in Ref. [23]. The measured transmittance decreases rapidly before the percolation threshold. After the percolation, the transmittance decrease slows down, stabilizes and then inverts the slope. The film transmits increasingly until the formation of a continuous layer. After this moment the transmittance turns to decrease again. The transmittance BBM of silver is most sensitive at approximately 560 nm which is the spectral position of the local surface plasmon resonances (LSPR) peak. It gradually loses its sensitivity at wavelengths above 900 nm.

Proper choice of a few wavelengths for transmittance monitoring simplifies estimation of the percolation threshold as well as moment of a continuous film formation. The latter represents thickness of optimized film characteristics: the highest transparency at good conductivity. In our deposition experiment, a silver film percolated at about 6 nm and became continuous at about 12 nm. This last thickness was slightly higher than 10 nm we received by the same deposition method for copper films [22].

In contrast with the results for copper films [22], very precise estimation of the silver layer thicknesses at which the coalescence and percolation begin was not straightforward and additional analysis was necessary. For example, the difference between coalescence and percolation in thin metal films may be observed using scanning electron microscope (SEM) images [35].

Modeling of the optical constants for island metal films and ultrathin plasmonic films is known to be challenging, even when such a high-sensitivity technique like ellipsometry is used [37–40]. To ensure a physically meaningful and reliable solution, multiple factors should be considered. The relatively high absorbance of such films at absence of interference fringes complicates the unpairing of two intertwined parameters, which are geometrical thickness and complex refractive index of the film. An additional difficulty raised by the film discontinuity is high depolarization of the acquired signal. On the other hand, in our analysis the measured depolarization spectra allowed us to evaluate

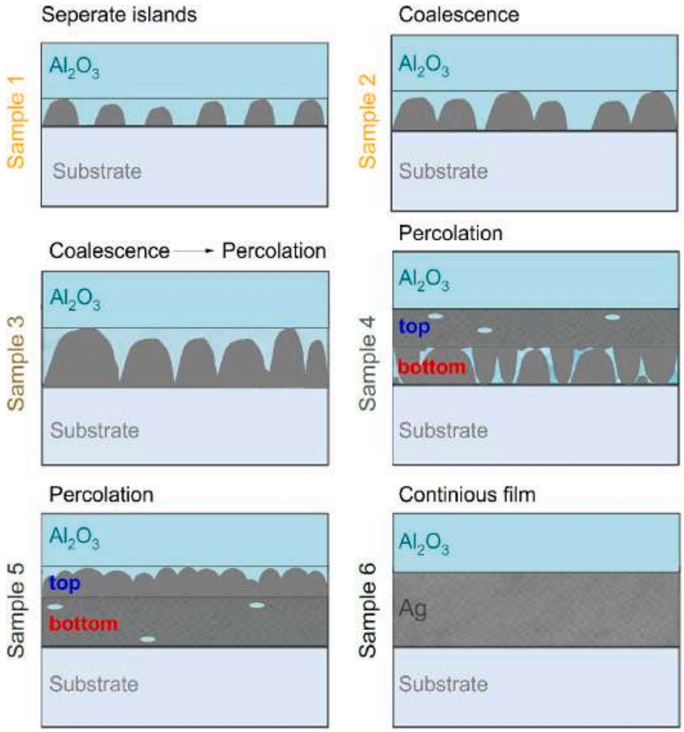

Fig. 4. Schematic of the coating model. Sample 1 – initial seeds; Samples 2 and 3 merging of seeds into bigger particles. Sample 4 – initial percolation as formation of a denser top sub-layer; Sample 5 - percolation proceeds as densification of the bottom sub-layer. The bilayer describing silver film in samples 4 and 5 consists of two effective media. Sample 6 - formation of a continuous silver film, the coating may be considered as a bilayer of flat dense silver and alumina.

residual backside reflection level, and depolarization factor. The latter is an important fitting parameter for such type of films. Furthermore, in the case of transparent substrates, partial transparency of such layers imposes both physical suppression of the backside reflection and its further parameterization.

A typical approach [41] in parameterization of the optical functions of island and ultrathin silver film consists of using the Lorentz or Gauss oscillators, and in particular modeling of the LSPR generated in silver nanoparticles of various shapes and sizes. For (partially) percolated films instead, the free-electron part of the spectrum is typically modeled using the Drude formula. Then the fit consists in variation of the oscillators' parameters. Insight of the film physical properties is hence given by the oscillators' parameters spectral position variation, together with the overall optical functions spectral dispersion.

Here we propose an insight into the silver film growth process using estimation of the silver content in the deposited films and the analysis of applicability of the effective medium approximation (EMA) models, namely the Maxwell-Garnett model (MGM) versus the Bruggemann model (BM). The proposed approach is very intuitive and allows a physical insight into the film formation mechanisms through its optical functions. Indeed, MGM describes an effective medium (composite) of well-separated particles (inclusions) randomly distributed in another material (host) [42–45]. MGM may be used for bi-component mixes when the volume fraction of inclusions is smaller than the volume fraction of the host material, because its formula is not symmetric for the two components. BM is typically used for mixes of components with similar volume fractions as well as for multi-component composites. However, as we will see below, there exist broader states of the silver film formation when both MGM and BM may bring meaningful results, helping to understand better the film morphology evolution.

To simplify the coating modeling, the thickness of about 12 nm for the deposited capping aluminum oxide layer was chosen to exceed the thickness of the percolation threshold for silver manufactured by sputtering process at similar deposition conditions [46]. This way the particles composing our silver films before and during the percolation may be considered as fully embedded in the alumina matrix. The alumina layer thickness is such to ensure a sufficient amount of the deposited material to fill the holes in the discontinuous silver film and to create an additional capping over the EMA film. Notice that the deposition of the capping alumina layer using ALD technique has an additional advantage to not perturb the morphology of the previously sputtered silver layer; instead it actually "freezes" it, what is particularly suitable to the aim of this study. Moreover, use of ALD technique for the alumina layer manufacturing ensures the absence of voids in the effective medium layer, thus it is considered as composed of alumina and silver only (we will discuss below the only exception among our samples in this concern).

Therefore, the thinnest of our silver films are particles and islands positioned at the bottom of the alumina film. A coating is hence modeled as a bilayer of a film of effective medium mix of silver and alumina covered by an alumina film of fixed thickness, Fig. 4 (Sample 1). This EMA layer becomes richer in silver until the formation of a continuous

Table 1
Summary of the ellipsometric analysis results.

Sample number	Mass (nominal) thickness, nm	Ellipsometrically estimated thickness, nm	Applied EMA model and Silver content	
			bottom sub-layer (thickness)	top sub-layer (thickness)
1	3	3.2	BM 69%	NA
2	5	5.0	MGM 42%	NA
3	8	9.4	MGM 45%	NA
4	11	8.2/10.5[a]	BM 76% (3.8 nm)/BM[a] 55% (3.5 nm)	BM 92% (4.4 nm)/MGM[a] 85% (7 nm)
5	13	9.7	BM 92% (5.9 nm)	BM 80% (3.8 nm)

[a] See text for details on the fraction calculation.

silver film, Fig. 4 (Sample 6).

The first step of the ellipsometric data elaboration was tuning only of the thickness of the EMA layer for the mixture of silver and alumina, as well as of the percentage of the silver content in this layer. The thickness of the modeled top alumina layer was kept fixed at 10 nm as long as little variations of this layer thickness impact very slightly the simulated ellipsometric spectra and mainly at their short-wavelengths part. For the same reason, the model is not sensitive to the presence of an overlayer, which can be used to describe roughness of the capping layer. Instead, the depolarization originating partly from the capping layer roughness is taken into account through the fitting parameter "depolarization factor".

The optical constants of alumina and those of silver used for the EMA mixture were taken from the J.A. Woolam WVASE32 database, which collects well-established data from the literature [47]. Optical constants of thin films are well-known to depend on the deposition technique and conditions. In particular, ALD-deposited oxides may be not free from residuals of the organic precursors and hence may contain trace amounts of H, N or C, in particular. Our alumina deposition process was properly tuned and a detailed material characterization was performed for a single layer of alumina of about 100 nm deposited on a fused silica substrate. Its optical constants were found to coincide with the optical constants from the Woolam database in the optical range of interest. The XPS analysis of the film evidenced the film near-stoichiometry (Al/O at. ratio of 1.54) and less than 1.6 at. % of N and C. The layer was amorphous and smooth with a roughness similar to that of the substrate. The optical response of "bulky" silver (100 nm-thick film sputtered on fused silica) was also possible to fit using the optical functions from the aforementioned database.

The second step was a very light B-spline adjustment of the optical functions, necessary to compensate for the fact that the theoretical optical functions of relatively thick films cannot adequately describe real complexity of ultrathin layers. In fact, the damping factor in the dielectric function represents the free electron damping rate due to collisions with other electrons, phonons, eventual grain boundaries and

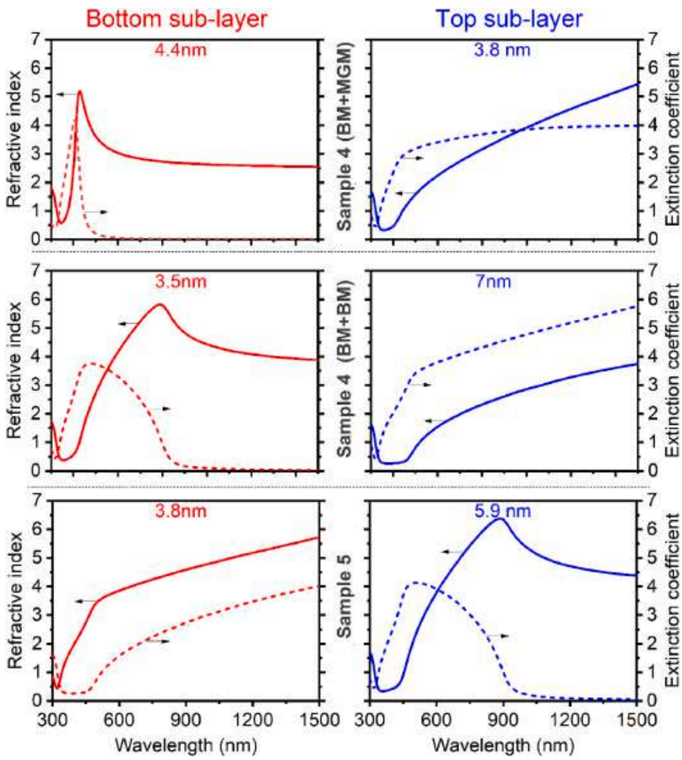

Fig. 5. The evaluated optical constants (see text for details) for the double-layer models describing two stages of the pre-coalescent silver films: sample 4 (rows 1 and 2) and sample 5 (row 3).

lattice imperfections. All these factors depend on the deposition process and the consequent film's structure and morphology. Furthermore, the chemical interface effect due to the alumina capping layer presence changes silver electron damping [26,48,49]. This last effect is proportional to the surface-to-volume ratio and hence is more pronounced for thinner silver films. Additionally, for the films consisting of non-percolated particles the chemical interface is also a function of the particle size and shape impacting the resulting LSPR peak amplitude, width and spectral position.

The aforementioned considerations do not preclude the analysis of the ellipsometric data in simple terms of EMA mixtures, as we will see below.

The film initial seed (separate islands) state (sample 1 of about 3 nm) can be well described using BM. The determined 69% silver volume fraction corresponds to a picture of a rather dense layer. Indeed, the corresponding film thickness value is close to the nominal thickness estimated from the deposition time, Table 1.

Starting from sample 2 (nominal 5 nm), MGM should be used to ensure a reasonable fit. This indicates the appearance of larger well-separated silver particles, Fig. 4 (Sample 2). Notice that the silver volume fraction drops down to 42% indicating the agglomeration of small seeds into larger particles forming the effective medium layer of thickness determined as 5 nm. Inapplicability of BM is in perfect agreement with the conclusions driven in Ref. [45], where rigorous analytic calculation of the spectral response of spherical metal particles in a dielectric matrix was compared with the Maxwell Garnett and the Bruggeman's formulas. It was demonstrated there that for such type of composite, the effective medium is accurately represented by MGM at low-to-moderate metal volume fractions, while BM does not provide any meaningful result.

For sample 3 (nominal 8 nm), the optical response still may be described by MGM. The separation distance between the particles decreases slightly (silver content 45%) and the particles keep growing in height, resulting in a layer of 9.4 nm.

Both samples 4 and 5 have a more complex optical response that can be described by a bilayer structure, as long as a single layer modeled by either BM or MGM is not anymore sufficient. In fact, the layer thicknesses corresponding to any of such homogeneous layer solutions result way too far from the nominal mass thickness.

In case of sample 4, the partial coalescence may be described by a stack composed of a denser top BM sub-layer over a BM bottom sub-layer of lower density, Fig. 4 (Sample 4). It is worth to underline the model sensitivity: it undoubtedly suggests that coalescence starts at the top of the grown particles because the resulting top sub-layer is richer in silver. Conversely, the reversed order of sub-layer densities results in impossibility to adjust the model parameters for a reasonable fit.

Notice that the bottom sub-layer of the sample 4 silver film may still be described using MGM that would lead to a different thickness of this sub-layer. Regardless of which model is used to describe the optical constants of the bottom sub-layer, both BM and MGM provide the same trend in the optical function change through the layer thickness. Rigorously speaking, in this case MGM was applied in the "flipped" version. Indeed, this model doesn't consider symmetrically the inclusions and host material and the host in this case should be silver filled with alumina inclusions. Such flipping is straightforward for two-component composites. The higher silver density of the upper sub-layer resulting independently from the applied model may be interpreted as a confirmation of the fact that coalescence begins at the top part of the growing film.

Formation of a denser layer at the top of the growing silver film may influence the bottom layer modelling, as far as it becomes inaccessible to the alumina overcoat. We hence recalculated the bottom layer effective constants for the mix of voids and silver. The relevant change in the optical response of the layer was negligible, as it was predictable.

The percolation proceeds towards the film bottom as it was inferred from the analysis of the ellipsometric spectra acquired on the sample 5.

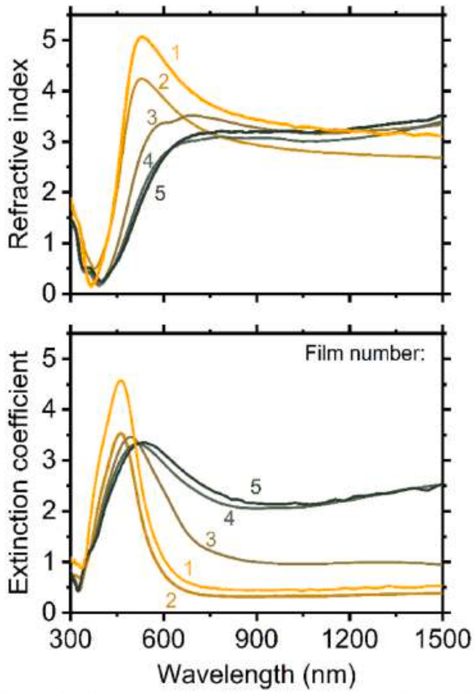

Fig. 6. The effective optical constants of the silver layers in samples 1 through 5, as evaluated from ellipsometric measurements at homogenous layer model.

In this case, the silver film of the nominal thickness 13 nm is described by a double sub-layer structure, too, emulating the in-depth inhomogeneity of the layer. Differently from the sample 4, for both sub-layers, only BM is the model to describe their optical response, and the bottom sub-layer results denser, Fig. 4 (Sample 5).

The aforementioned conclusions on the morphology of our samples are summarized in Table 1 in terms of layer thicknesses. Fig. 5 reports the optical constants of their top and bottom sub-layers for the samples 4 and 5.

Interestingly, the overall thickness of both sub-layers is lower than the nominal silver layer thickness. This is true for both sample 4 and sample 5. The percolating structure "spreads" over the substrate, resulting in a thinner and denser film. The film growth proceeds by filling of the remaining holes along with the thickness increase. The layer top naturally has some residual roughness: notice the residual presence of peaks at approximately 400 nm indicating residual LSPR in the remaining Ag nanoparticles at the top of the silver layer.

This process is also well observed in the transmittance BBM curves, Fig. 3, in the film resistivity trend, and in the change of the LSPR parameters, as discussed below, Fig. 7.

To simplify comparison of our results with the literature data, in Fig. 6 we report the results of the ellipsometric data modeling using the traditional approach. These more conventional optical functions obtained by tuning the oscillators' parameters describe a homogenous silver layer. Fig. 6 hence illustrates the evolution of the optical functions of a growing homogenous silver film with the film thickness. When evaluating these optical functions, for all silver films we kept their thicknesses fixed to the values determined using the above described

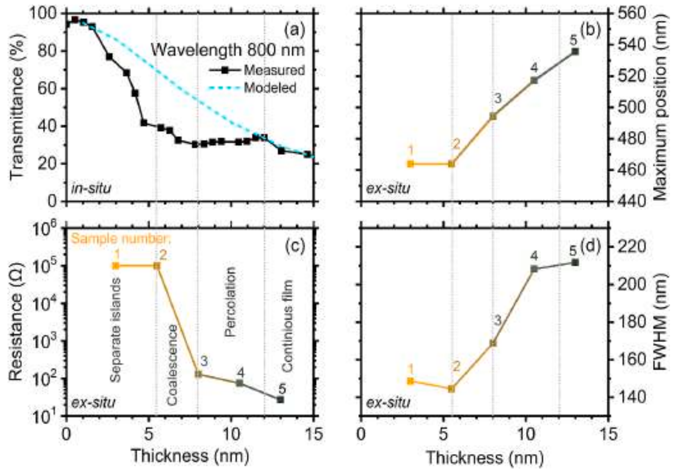

Fig. 7. Transmittance (a), LSPR Maximum position (b), Resistance (c) and LSPR FWHM (d) values evolution with the silver film thickness. The dotted vertical lines indicate three various stages of the growing film.

method. A slight final B-spline adjustment was necessary for all samples. This approach was used to visualize the LSPR spectral position and bandwidth as functions of the film thickness.

Fig. 7 illustrates the evolution of the optical and electrical properties of the silver films with their growth. Similarly to the film transmittance (Fig. 7a), the film resistivity decreases rapidly when separate islands merge (Fig. 7c), up to the percolation threshold when conductive channels appear. When the connected islands form the channels [50], the films become conductive, although it is still not continuous [51]. Our magnetron sputtered silver films became conductive at approximately 6 nm thickness, similar to the results reported in Ref. [46]. It is twice thinner than for electron beam evaporated film [51]. Sputtered films percolate earlier due to higher process energy compared to evaporation [2]. Lower thickness means lower absorption that is a desired quality for many optical applications.

With the thickness increase, the resonant wavelength shifts to longer wavelengths (Fig. 7b) and hence the extinction coefficient peak position shifts to longer wavelengths. Similar results were reported for semi-continuous sputtered films [52] and continuous films [53]. With the film thickness increase, the free electron density increases to reach the value of bulk silver, which agrees with the observed increasing metallic behavior. Moreover, the full width at half maximum (FWHM) of the LSPR increases with the increase in film thickness (Fig. 7d).

4. Conclusions

We investigated the stages of formation of ultrathin sputtered silver films using *in-situ* and *ex-situ* methods, in terms of their microstructure, optical and electrical properties. Films of selected thicknesses in the range from 3 nm to 100 nm were manufactured. A particularly detailed investigation was performed for films up to 40 nm thickness, in order to study the growth stages for the thicknesses below the electron mean free path in silver.

We show that BBM of the film transmittance is a suitable method for reliable estimation of film growing stages and the minimum thickness of continuous film. Furthermore, we show that monitoring of silver film transmittance in the visible range has high sensitivity, while it is not as much sensitive in the near infrared. We infer hence that the monitoring can be further simplified if performed at a few proper wavelengths. We show that this method is more informative than the resistance measurements. This method is non-invasive and straightforward for implementation. The four stages of the metal film growth - separate islands, coalescence, percolation and continuous film - are well distinguishable when monitoring the film transmittance, and are clearly distinguishable in evolution of *ex-situ* measured resistance and ellipsometrically evaluated LSPR maximum position and broadening.

We also show that ellipsometry is extremely sensitive to the in-depth analysis of silver ultrathin films and hence allows for monitoring of the percolation process. In particular, ellipsometric analysis infers that the coalescence of silver nanoparticles begins from the top of the growing film, proceeds with the holes filling what leads finally to denser bottom part of the silver layer with residual particles at the layer top.

CRediT authorship contribution statement

Alexandr Belosludtsev: Funding acquisition, Conceptualization, Investigation, Methodology, Project administration, Resources, Visualization, Writing – original draft, Writing – review & editing. **Anna Sytchkova:** Writing – review & editing, Writing – original draft, Visualization, Supervision, Methodology, Investigation, Conceptualization. **Naglis Kyžas:** Investigation, Validation, Writing – original draft, Writing – review & editing. **Ignas Bitinaitis:** Investigation, Writing – review & editing. **Rimantas Simniškis:** Investigation, Writing – original draft, Writing – review & editing. **Ramutis Drazdys:** Writing – review & editing, Investigation.

Declaration of competing interest

The authors declare that they have no known competing financial interests or personal relationships that could have appeared to influence the work reported in this paper.

Acknowledgement

This work was supported by the European Social Fund (project No 09.3.3.-LMT-K-712-21-0102) under a grant agreement with the Research Council of Lithuania (LMTLT). Also, A.B. would like to acknowledge Optical Coatings Group at ENEA, Italy for hosting.

References

[1] R.S. Sennett, G.D. Scott, The structure of evaporated metal films and their optical properties, J. Opt. Soc. Am. 40 (1950) 203–211.
[2] C.E. Ells, G.D. Scott, The structure of sputtered silver films, J. Appl. Phys. 23 (1952) 31–34.
[3] T. Perova, I. Shaganov, K. Berwick, Accounting for the local field when determining the dielectric loss spectra of metals in the region of the frequencies of volume, surface and localized plasmon oscillations, Materials 13 (2020) 631.
[4] E. Jeong, T. Lee, S.-G. Lee, S.M. Yu, J.-S. Bae, G.-H. Lee, D. Choi, J. Yun, Thermal stability enhancement of ultrathin Ag film electrodes by incorporating atomic oxygen, Appl. Surf. Sci. 546 (2021) 149149.
[5] A.E. Gumrukcu, H. Kaplan, N.A. Sonmez, S. Ozcelik, Electrical, optical and structural properties of silver-based multilayer films deposited by magnetron sputtering, J. Mater. Sci. Mater. Electron. 30 (2019) 18519–18523.
[6] M.M. Rahman, M.K. Basher, M. Vasiliev, K. Alameh, Optical and chromaticity properties of metal-dielectric composite-based multilayer thin-film structures prepared by rf magnetron sputtering, Coatings 10 (2020) 251.
[7] F. Anjum, D.M. Fryauf, R. Ahmad, A.C. Phillips, N.P. Kobayashi, Improving silver mirrors with aluminum oxynitride protection layers: variation in refractive index with controlled oxygen content by radiofrequency magnetron sputtering, J. Astron. Telesc. Inst. 4 (2018) 44004.
[8] C. Grèzes-Besset, N. Valette, G. Chauveau, M. Castelnau, K. Mathieu, M. Tatat, F. Lemarquis, in: Int. Conf, Sp. Opt (Eds.), High Performance Silver Coating with PACA2M Magnetron Sputtering, International Society for Optics and Photonics, 2018, p. 1118083, 2019.
[9] L. Mao, Y. Geng, Y. Cao, Y. Yan, Uniform high-reflectivity silver film deposited by planar magnetron sputtering, Vacuum 185 (2021) 109999.
[10] E. Buzavaite-Verteliene, I. Plikusiene, T. Tolenis, A. Valavicius, J. Anulyte, A. Ramanavicius, Z. Balevicius, Hybrid Tamm-surface plasmon polariton mode for highly sensitive detection of protein interactions, Opt Express 28 (2020) 29033–29043.
[11] J. Zhu, L. Sun, Y. Shan, Y. Zhi, J. Chen, B. Dou, W. Su, Green preparation of silver nanofilms as SERS-active substrates for Rhodamine 6G detection, Vacuum 187 (2021) 110096.
[12] P. Zhao, S. Kim, S. Yoon, P. Song, Characteristics of indium zinc oxide/silver/indium zinc oxide multilayer thin films prepared by magnetron sputtering as flexible transparent film heaters, Thin Solid Films 665 (2018) 137–142.
[13] R.V. Babu, J.M. Fernandes, M. Kovendhan, N. Purushothamreddy, R. Muniramaiah, R. Arockiakumar, N.S. Karthiselva, D.P. Joseph, Investigation of structural, optical, electrical and mechanical properties of transparent conducting 'Ag'electrodes, Physica B 607 (2021) 412690.
[14] C. Zhang, C. Ji, Y. Park, L.J. Guo, Thin-metal-film-Based transparent conductors: material preparation, optical design, and device applications, Adv. Opt. Mater. 9 (2021) 2001298.
[15] G. Cesarini, G. Leahu, M.L. Grilli, A. Sytchkova, C. Sibilia, R. Li Voti, Optical and photoacoustic investigation of AZO/Ag/AZO transparent conductive coating for solar cells, Phys. Status Solidi C 13 (2016) 998–1001.
[16] C.-T. Wu, Y.-R. Ho, D.-Z. Huang, J.-J. Huang, AZO/silver nanowire stacked films deposited by RF magnetron sputtering for transparent antenna, Surf. Coating. Technol. 360 (2019) 95–102.
[17] E.M. Kaidashev, A.M. Lerer, E. V Golovacheva, V.E. Kaydashev, N. V Lyanguzov, E. A. Tsvetyanskii, Experimental and theoretical study of optical antennas formed from ZnO nanorods coated with a thin silver film, J. Commun. Technol. El.+ 62 (2017) 1328–1335.
[18] Y. Pan, Y. Fan, J. Niu, Optical properties of ultra-thin silver films deposited by thermal evaporation and its application in optical filters, Infrared Phys. Technol. 104 (2020) 103123.
[19] A.S. Baburin, A.I. Ivanov, I.A. Ryzhikov, I. V Trofimov, A.R. Gabidullin, D. O. Moskalev, Y. V Panfilov, I.A. Rodionov, Crystalline structure dependence on optical properties of silver thin film over time. 2017 Prog. Electromagn. Res. Symp., IEEE, 2017, pp. 1497–1502.
[20] Y. Liu, C.-F. Guo, S. Huang, T. Sun, Y. Wang, Z. Ren, A new method for fabricating ultrathin metal films as scratch-resistant flexible transparent electrodes, J. Materiomics 1 (2015) 52–59.
[21] C. Ji, D. Liu, C. Zhang, L.J. Guo, Ultrathin-metal-film-based transparent electrodes with relative transmittance surpassing 100, Nat. Commun. 11 (2020) 1–8.
[22] A. Belosludtsev, N. Kyžas, Real-time in-situ investigation of copper ultrathin films growth, Mater. Lett. 232 (2018) 216–219.
[23] A. Axelevitch, B. Apter, In-situ investigation of optical transmittance in metal thin films, Thin Solid Films 591 (2015) 261–266.
[24] J. Colin, A. Jamnig, C. Furgeaud, A. Michel, N. Pliatsikas, K. Sarakinos, G. Abadias, In situ and real-time nanoscale monitoring of ultra-thin metal film growth using optical and electrical diagnostic tools, Nanomaterials 10 (2020) 2225.
[25] P. Bulkin, S. Gaiaschi, P. Chapon, D. Daineka, N. Kundikova, Protective coatings for front surface silver mirrors by atomic layer deposition, Opt Express 28 (2020) 15753–15760.
[26] V.P. Drachev, U.K. Chettiar, A. V Kildishev, H.-K. Yuan, W. Cai, V.M. Shalaev, The Ag dielectric function in plasmonic metamaterials, Opt Express 16 (2008) 1186–1195.
[27] B. Lesage, Some aspects of diffusion in ceramics, J. Phys. III 4 (1994) 1833–1850.
[28] A.J. Houska, T. Kozak, Relationships between the distribution of O atoms on partially oxidized metal (Al, Ag, Cu, Ti, Zr, Hf) surfaces and the adsorption energy: a density-functional theory study, J. Appl. Phys. 121 (2017) 225303.
[29] A. Sytchkova, A. Belosludtsev, R. Volosevičienė, L. Juškėnas, R. Simniškis, Structural, optical and electrical properties of sputtered ultrathin chromium films, Opt. Mater. 121 (2021) 111530.
[30] S.W. Brittle, J.D. Baker, K.M. Dorney, J.M. Dagher, T. Ebrahimian, S.R. Higgins, I. E. Pavel Sizemore, Measuring the silver composition of nanocolloids by inductively coupled plasma–optical emission spectroscopy: a laboratory experiment for chemistry and engineering students, J. Chem. Educ. 92 (2015) 1061–1065.
[31] M. Novotný, J. Bulíř, P. Pokorný, J. Lančok, L. Fekete, J. Musil, M. Čekada, RF magnetron sputtering of silver thin film in Ne, Ar and Kr discharges—plasma characterisation and surface morphology, Surf. Coating. Technol. 228 (2013) S466–S469.
[32] N. Britun, A. Belosludtsev, T. Silva, R. Snyders, Ground state atomic oxygen in high-power impulse magnetron sputtering: a quantitative study, J. Phys. D Appl. Phys. 50 (2017), 075204.
[33] N. Britun, J. Hnilica, Optical spectroscopy for sputtering process characterization, J. Appl. Phys. 127 (2020) 211101.
[34] S.A. Irimiciuc, S. Chertopalov, J. Bulíř, L. Fekete, M. Vondráček, M. Novotný, M, V. Craciun, J. Lancok, In situ optical and electrical analysis of transient plasmas generated by ns-laser ablation for Ag nanostructured film production, Vacuum 193 (2021) 110528.
[35] X. Yu, P.M. Duxbury, G. Jeffers, M.A. Dubson, Coalescence and percolation in thin metal films, Phys. Rev. B 44 (1991) 13163.
[36] L. Wang, L. Li, W.-D. Chen, Investigation of the properties of silver thin films deposited by DC magnetron sputtering, Surf. Rev. Lett. 24 (2017) 1750053.
[37] M. Carlberg, F. Pourcin, O. Margeat, J. Le Rouzo, G. Berginc, R.-M. Sauvage, J. Ackermann, L. Escoubas, Spectroscopic ellipsometry study of silver nanospheres and nanocubes in thin film layers, Opt. Mater. Express 7 (2017) 4241–4248.
[38] R. Secondo, D. Fomra, N. Izyumskaya, V. Avrutin, J.N. Hilfiker, A. Martin, Ü. Özgür, N. Kinsey, Reliable modeling of ultrathin alternative plasmonic materials using spectroscopic ellipsometry, Opt. Mater. Express 9 (2019) 760–770.
[39] M. Arya, A. Dewasi, A. Mitra, Spectroscopic ellipsometer study of laser ablation wavelength dependent growth kinetics of Ag nanoislands: an insight to potential plasmonic applications, Appl. Surf. Sci. 447 (2018) 87–99.
[40] T.V. Amotchkina, V. Janicki, J. Sancho-Parramon, A.V. Tikhonravov, M. K. Trubetskov, H. Zorc, General approach to reliable characterization of thin metal films, Appl. Opt. 50 (2011) 1453–1464.
[41] O. Stenzel, S. Wilbrandt, S. Stempfhuber, D. Gäbler, S.-J. Wolleb, Spectrophotometric characterization of thin copper and gold films prepared by electron beam evaporation: thickness dependence of the Drude damping parameter, Coatings 9 (2019) 181.
[42] V.A. Markel, Introduction to the Maxwell Garnett approximation: tutorial, JOSA A 33 (2016) 1244–1256.
[43] J.C. Maxwell-Garnett, Colours in metal glasses and in metallic films, Phil. Trans. Roy. Soc. Lond. 203 (1904) 385–420.
[44] J.C. Maxwell-Garnett, , —II, Philos. Trans.R. Soc, London, A. Ser, Colours in metal glasses, in metallic films, and in metallic solutions, Contain. Pap. a Math. or Phys. Character. 205 (1906) 237–288.
[45] V.A. Markel, Maxwell Garnett approximation (advanced topics): tutorial, JOSA A 33 (2016) 2237–2255.
[46] A. Sytchkova, M. Luisa Grilli, A. Rinaldi, S. Vedraine, P. Torchio, A. Piegari, F. Flory, Radio frequency sputtered Al: ZnO-Ag transparent conductor: a plasmonic nanostructure with enhanced optical and electrical properties, J. Appl. Phys. 114 (2013) 94509.
[47] E.D. Palik, Handbook of Optical Constants of Solids, Academic press, 1998.
[48] B.N.J. Persson, Polarizability of small spherical metal particles: influence of the matrix environment, Surf. Sci. 281 (1993) 153–162.
[49] A. Pinchuk, U. Kreibig, A. Hilger, Optical properties of metallic nanoparticles: influence of interface effects and interband transitions, Surf. Sci. 557 (2004) 269–280.
[50] C.A. Davis, D.R. McKenzie, R.C. McPhedran, Optical properties and microstructure of thin silver films, Opt Commun. 85 (1991) 70–82.
[51] H. Wei, H. Eilers, From silver nanoparticles to thin films: evolution of microstructure and electrical conduction on glass substrates, J. Phys. Chem. Solid. 70 (2009) 459–465.
[52] Q.-Q. Wang, J.-B. Hun, S. Ding, G.-G. Xiong, D.-C. Tian, Percolation characters of sputtered and vaporized semi-continuous silver island films, Appl. Surf. Sci. 243 (2005) 329–334.
[53] A. Valavičius, P. Jurkšaitis, S. Kičas, A. Belosludtsev, Optimization of thermal evaporation for continuous silver films and their application for non-polarizing optical components, in: Adv. Opt. Thin Film. VI, International Society for Optics and Photonics, 2018, p. 106911Y.

B. Proton resistance of high reflective silver-aluminium mirrors for space applications

A. Belosludtsev, I. Bitinaitis, J. Želudevičius, V. Kovalevskij,
S. T. Rastkar, A. Sytchkova

Available online at www.sciencedirect.com

ScienceDirect

Advances in Space Research 78 (2026) 5404–5412

ADVANCES IN SPACE RESEARCH
(a COSPAR publication)

www.elsevier.com/locate/asr

Proton resistance of high reflective silver-aluminium mirrors for space applications

Alexandr Belosludtsev [a,*], Ignas Bitinaitis [a], Julijanas Želudevičius [a], Vitalij Kovalevskij [a], Sabereh T. Rastkar [b], Anna Sytchkova [b,*]

[a] Center for Physical Sciences and Technology, Savanoriu ave. 231, Vilnius 02300, Lithuania
[b] Optical Coatings Group, ENEA Casaccia, via Anguillarese 301, Roma 00123, Italy

Received 4 January 2026; received in revised form 21 June 2026; accepted 27 June 2026
Available online 30 June 2026

Abstract

The volume of information necessary to transmit on Earth, in space, and between satellites and ground stations is increasing. Satellites are planned to be connected to the global secured quantum network on low-Earth orbits, to be used for quantum communication at higher distances from our planet. Such applications require optical components like metallic mirrors for signal preparation and transfer. In this study, we report a systematic investigation on the silver-aluminium (Ag-Al) mixed mirrors designed for space missions. We show the Ag-Al mixed coatings preparation process and investigate their properties for various Al concentrations up to 15%. It was found that 5–8% of Al admixing leads to the formation of smooth mirrors with high reflectance (measured >90% vis-IR range). Mirrors were tested by low-energy proton irradiation at doses typical for low-Earth orbits. It was shown that the 8% Al concentration represents an optimal solution for high reflectance and proton-resistant mirrors.

Keywords: Metal mirrors; Silver-aluminium mixed films; Magnetron sputtering; Radiation tests; Space Optics; Quantum communication

1. Introduction

Silver (Ag) is a widely used metal in various fields, including metamaterials, plasmonics, optics, optoelectronics, and many others. Thanks to its highest metallic reflectivity in a wide spectral range, Ag-based coatings are traditionally applied as telescope mirrors (Jacobson et al., 1998; Atad-Ettedgui and Dierickx, 2004; Vucina et al., 2008). The use of silver increases the telescopes' sensitivity and helps achieve significant infrared optimization while being cost-effective. Acknowledging Ag properties, new space missions consider this metal as their primary choice in the Kepler Mission (Sheikh et al., 2008) and others. Ag-based coatings show great perspective in plasmonic applications, as together with the highest reflectivity, Ag has the lowest polarization splitting in a broad VIS-IR (400–10000 nm) wavelength range (Thomas et al., 1998; Heaney et al., 2012). Also, Ag has the highest figure of merit (FoM = $\mathrm{Re}\{\varepsilon\}/\mathrm{Im}\{\varepsilon\}$, where ε is the material dielectric function) that is necessary for plasmonic applications (Heaney et al., 2012). Furthermore, Ag is used in cutting-edge applications such as transparent cathodes and transparent organic light-emitting diodes (Song et al., 2020), solar reflectors (Adams et al., 1979), transparent conductors (Sytchkova et al., 2013), semi-transparent smart

* Corresponding authors.
E-mail addresses: Alexandr.Belosludtsev@ftmc.lt (A. Belosludtsev), Anna.Sytchkova@enea.it (A. Sytchkova).

https://doi.org/10.1016/j.asr.2026.06.103
0273-1177/

windows (Zhang et al., 2014), and long-range surface plasmon polariton waveguides (Zhang et al., 2017).

Among the drawbacks of silver implementation as thin film coatings are its low adhesion to glass substrates and high vulnerability to sulphating and oxidation when exposed to air. Although the cleaning procedures can help to achieve higher wettability of glass and hence facilitate adhesion of silver (Bakar et al., 2025), to meet adhesion standards such as MIL-C-675C (Hausner, 2019), adhesive or seed layers (Formica et al., 2013) are commonly used. To prevent tarnishing, silver layers are commonly protected with layers of metal oxides or fluorides (Wulff, 1934; Harris and Siegel, 1948; Weaver and Brown, 1968). Silver protection with oxide layer has been extensively studied (e.g., (Sytchkova et al., 2018) and references within) yet regardless noticeably enhanced mirror durability, further development is required for ever growing application needs. Additional improvement of the mechanical and chemical stability of silver layers can be achieved by mixing Ag with other materials, such as Ca, TiO_2, VCN (Navabpour et al., 2014; Bondarev et al., 2017; Wang et al., 2021). Mixing silver with aluminum results in films with better thermal stability compared to pure silver films, under the condition of post-deposition annealing at 200 °C (Appleget et al., 2022).

It is well-known that Ag is the most reflective material (>95%) across the visible spectrum. In comparison, aluminium (Al) is slightly less reflective (>90%) in the visible but has higher reflection in the UV and the vacuum-ultraviolet (VUV) ranges (Yang et al., 2006). Al films naturally form a transparent oxide layer of approximately 5 nm thickness within 24 h of exposure to air. Such an oxide film is a sufficient natural protection layer preventing atmospheric corrosion of the underlying metallic aluminum (Hass, 1949). Mixed silver-aluminium (Ag-Al) mirrors were investigated previously (De Silva et al., 2017). It was reported (Appleget et al., 2022) that a small addition of Al (1–2 at%) is beneficial as it reduces surface roughness and does not have an adverse effect on optical losses. It was also shown (Zhang et al., 2017) that at such low Al concentrations, the Ag-Al film is more resistant to oxidation in air with minimal losses in reflectance. The alloying induces favorable changes in the dielectric function by increasing the electron-to-atom ratio; it also smoothens the film surface and enhances the film's thermal stability (Gu et al., 2014; Wang et al., 2024). Aluminum concentration above 2% in Ag-Al mixed film increases dielectric function values of the imaginary part. This increases the film's optical losses due to absorption (De Silva et al., 2017), despite further decreasing of surface roughness and hence of optical scattering (Gu et al., 2014). Decreased surface roughness induces Ag-Al film permittivity. Consequently, the film conductivity occurs at a film thickness of 6 nm, which is much lower compared to 11 nm in pure Ag films, it depends on deposition technique and conditions (Gu et al., 2014), which is an important factor for plasmonic devices and metamaterials.

Nowadays, there is an increased interest in quantum networking for which satellite-based receivers and transmitters are essential (Sidhu et al., 2021). While quantum communication networks based on low-Earth-orbit satellites is in the focus of today research, higher orbits open multiple future opportunities (Chapman and Peters, 2022). Such communication systems based on photon entanglement and transmission are essentially optical systems often relying on metal mirrors, which encounter various space-related degradation issues (Garoli et al., 2020; Sytchkova et al., 2024a). For deep-space missions, extreme temperatures and energetic charged particles represent the main damaging environmental factors for coated optical components. Cosmic rays consist of a continuous flux of charged particles - approximately 85% protons, 14% helium nuclei, and 1% heavy ions. Particles with keV-level energies can become implanted within coatings, inducing optical, structural, and morphological changes depending on their density (Di Sarcina et al., 2014; Sytchkova et al., 2023; Wang et al., 2023a, b; Corso et al., 2024; Sytchkova et al., 2024b). Higher-energy particles, capable of penetrating coatings up to 10 μm thick, can reach and affect the underlying substrate. Usually, charged particles influence thin film performance in the UV region, and their damage can be minimized using various protective coatings.

Coatings must be prepared and tested to withstand particle fluxes and energies encountered in earlier space missions. Having films that are radiation-stable and can be used for a specific amount of time is crucial. Specific standards have been elaborated by national and European space agencies. Their thoughtful implementation is necessary to perform environmental stability tests on coated optics with reliable results (Sytchkova et al., 2024b).

In this paper, we investigated various silver-aluminium mixed mirrors. The 150 nm-thick Ag-Al films with Al concentrations of 0–15% were manufactured by using magnetron sputtering. The dependence of surface roughness and reflectance of the films was investigated in detail. The present work mostly focuses on radiation durability improvements rather than optimization for specific laser comms wavelengths. Finally, an investigation of proton radiation effects on Ag-Al mixed space mirrors is conducted to understand how different Al concentrations affect film durability and performance for space applications.

2. Experimental details

All our films were manufactured using unbalanced magnetron sources Torus^{TM} in a Kurt J. Lesker sputtering system (PVD225). The sputtering system was initially pumped down to a base pressure below 3×10^{-7} Torr. All sputtering targets (Ag, 99.99%, Cr 99.95%, Al 99.999% and Si 99.9999% purity) were circular planar. The magnetrons were driven by a pulsed DC power supply (Advanced Energy Pinnacle Plus) and a Rf power supply (Kurt J. Lesker R601). The Rf power supply was operated at a

13.56 MHz frequency. All process gases were >99.999% pure. The argon (Ar) flow rate was 20 sccm, and the pumping speed was adjusted to attain the argon pressure at the same value of 2.2 mTorr. The settings of the Ar flow rate and the pumping speed were not changed during the experiments. Before every deposition, the target was pre-sputtered for 5 min to remove impurities and possible surface oxides. The experiments were done at room temperature and without substrate biasing. The deposition conditions for the 10 nm Cr adhesive layer are described in Refs. (Sytchkova et al., 2021; Belosludtsev et al., 2023). The metallic coatings were then protected with a 9 nm- thick SiO_2 layer using the deposition conditions described in Ref (Juškevičius et al., 2015). A protective coating is needed to prevent any Ag and Al reaction with atmosphere. It is well known about Al oxidation and Ag tarnishing, and their degradation when exposed to sulfur, oxygen, or other atmosphere contaminants. The thicknesses of the adhesive Cr layer, the Ag-Al reflective layers, and the protective layer were kept the same for all samples. The schematic of the coating structure is introduced in Fig. 1.

The 150 nm Ag-Al films with Al concentration varying from 0% to 15% were prepared using co-sputtering of two targets, at calibrated deposition rates. Deposition times were adjusted to reach equal thickness for all deposited samples. To determine the volume fraction of Al in the co sputtered Ag-Al films we first measured single target deposition rates for Al (Rf) and Ag (pulsed-DC) for the same chamber geometry and process conditions used in case of co sputtering. Films thickness (measured by profilometry) versus deposition time were used to obtain each target rates R_{Al} and R_{Ag} ($nm \cdot s^{-1}$). The volume fraction of Al was then calculated as $Vol\%_{Al} = 100\%$ x R_{Al} /(R_{Al} + R_{Ag}). Selected co deposited films were independently analyzed by profilometry to verify the calibration; agreement was within experimental uncertainty. This empirical calibration is necessary because sputter yield and discharge coupling differ between Rf and pulsed-DC operation and depend on tool geometry and process conditions. In all the experiments, for Ag, pulsed-DC power was fixed to 200 W, and for Al, Rf power ($Vol\%_{Al}$) were 0 W (0%), 20 W (5%), 30 W (8%), 40 W (10%), and 64 W (15%). Values in parentheses present corresponding calculated volume percentage of Al in Ag-Al mixed films.

Films were deposited on 1 mm-thick double-side polished fused silica (FS) substrates of 25.4 mm in diameter. Bare substrates' flatness was at least λ/10.

Reflectance spectra were measured in 320–1300 nm wavelength range using a Photon RT spectrophotometer. Wavelength accuracy is 0.5 nm for 185–990 nm wavelength range, and is 1 nm for the 990–1700 nm wavelength range. Surface topography was investigated using a Bruker, Dimension Edge, Atomic Force Microscope (AFM) in tapping mode, over a 10 μm × 10 μm scan area. For roughness evaluation, root mean square roughness (R_q) values were calculated. For space environment resistance tests, samples

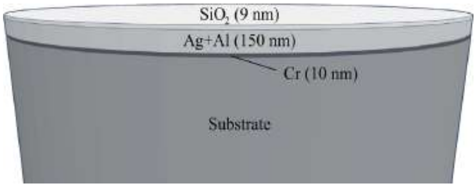

Fig. 1. Schematic of the deposited samples.

were irradiated with H^- ions of 20 keV energy and at fluences from 9.5×10^{14} cm^{-2} to 1.8×10^{16} cm^{-2}. Negative hydrogen ions were generated using a Hiconex-type cesium sputter ion source. Ions of the desired species were selected by an inflection magnet, focused using an Einzel lens, and directed into the experimental chamber equipped with a five-axis goniometer for precise sample positioning. The beam current was monitored continuously during irradiation using a Faraday cup connected to a picoampermeter with a 200 ms integration time. Total fluence was calculated by integrating the measured current over the entire irradiation period. Although beam current was not actively stabilized, the ion flux remained approximately constant at $\sim 10^8$ cm^{-2} s^{-1} throughout all irradiation sessions. During the irradiation, one-half of each sample was covered with a protective foil. Protected part of the sample was used as the reference.

The elemental composition of films was investigated by X-ray photoelectron spectroscopy (XPS). XPS characterization was carried out using a Kratos (Manchester, UK) AXIS Supra + spectrometer with monochromatic Al Kα (1486.6 eV) X-ray radiation powered at 225 W. The base pressure in the analysis chamber was less than 1×10^{-9}-mbar, and a low electron flood gun was used as a charge neutralizer. Survey spectra for each sample were recorded at pass energy 160 eV in 1 eV step and high-resolution spectra (pass energy 10 eV, in 0.1 eV steps) over individual element peaks. Binding energy scale was calibrated by setting the C1s hydrocarbon peak at 284.8 eV. For surface cleaning, the monoatomic Ar^+ ions gun (Minibeam 6) was used.

Depth profile calculations showing the concentrated distribution pattern within the coating layer were calculated using SRIM software (Ziegler et al., 2010).

Durability test were done according to the MIL-C-48616 standard. The samples underwent one thermal cycle test for 2 h, first being cooled to −62 °C, then heated to +71 °C. Afterwards, they were subject to humidity tests at 45 °C temperature and relative humidity of 95–100%, for 24 h. Coating adhesion was checked using the scotch-tape test.

3. Results and discussion

3.1. Optical properties of as-deposited Ag-Al mixed mirrors

Measured reflectance spectra of Ag-Al mixed mirrors are presented in Fig. 2.

A pronounced reflectance dip at about 360 nm is due to silver surface plasmon resonance, which spectral position depends on both the Ag-Al film composition and the refractive indices of the media surrounding the plasmonic film (Sytchkova et al., 2013a, 2013b; Hu et al., 2017).

Although Al is known for its excellent reflection in the UV range (Yang et al., 2006; Hernandez et al., 2005), the measured reflectance spectra clearly illustrate that reflectance for wavelengths over 325 nm decreases with increase of Al concentration in the coating. The reflectance drop may be explained by increase of electron-to-atom ratio, which red-shifts reflectance spectra due to intraband transitions (De Silva et al., 2017). Another mechanism that influences reflectance decrease of Ag-Al mixed films is the generation of intermetallic phase of Ag_3Al, which appears at higher Al concentration values and decreases reflectivity (Hummel, 1981a). Instead, for the wavelengths shorter than 322 nm (3.85 eV, the plasma resonance frequency of pure silver, (Huber and Marinero, 1988; Johnson and Christy, 1972), reflectance slightly increases with Al concentration caused by the blue shift of plasma frequency of mixed metals thanks to much higher plasma resonance spectral position of aluminum (15 eV) (Palik, 1985).

In accordance with the data reported in the literature (Gu et al., 2014; Wang et al., 2023a), we observed surface roughness decrease along with increase in the aluminum concentration in silver layers. Measured results are introduced in Fig. 3. Several wavelengths used in common applications are evidenced on this graph: two typical laser wavelengths of 355 nm and 532 nm, as well as 831 nm wavelength of SiV diamond quantum memories and 1300 nm of optical telecom. For the sample with 15% of Al, the surface roughness is similar to the roughness of the bare fused silica substrates (R_q = 0.6–0.8 nm) used for our film manufacturing.

Film roughness decreases with increase of Al concentration, which is associated with specificity of Al growth. Al tends to grow as a denser structure with smaller particles, compared to Ag (Gu et al., 2014). Such dense structure growth might be associated with lower Al diffusion rate, because metals with smaller diffusion rate exhibit higher nuclei density and smaller particle size.

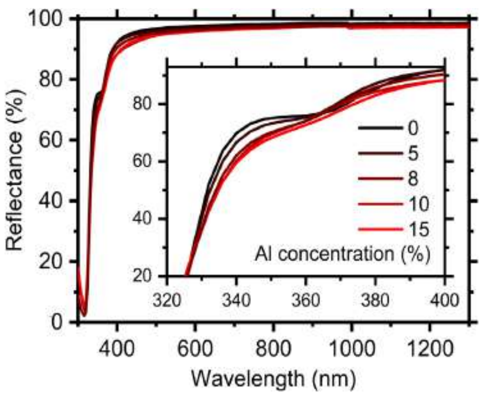

Fig. 2. Reflectance spectra of Ag-Al mixed films with 0–15% Al concentration. In inset it is shown zoomed UV spectra part.

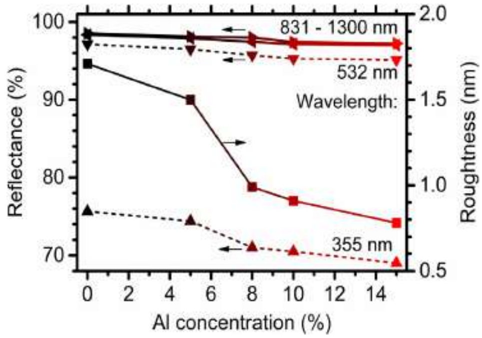

Fig. 3. Dependence of reflectance at various wavelengths and roughness values on the Ag-Al mixed films with 0–15% Al concentration.

3.2. Proton radiation impact on Ag-Al mixed mirrors

Proton implantation parameters for this experiment were selected for the assessment of Ag-Al mixed films at conditions representative to test coated optics for low-Earth orbits space missions. The average solar proton fluences ("worst week" conditions) across the 20–30 keV energy interval with a time exposure of 10 years at L1 Lagrange point of the Sun-Earth system can be estimated as $1.3 \cdot 10^{12}$ cm^{-2} (Sytchkova et al., 2024b). The radiation fluence values chosen for our tests correspond to radiation stress equal to several decades of exploitation in interplanetary space.

The simulation results presented in Fig. 4 illustrate the distribution of incident ions throughout the Ag-Al mixed film. Ion distribution profile shows that, at the chosen test conditions, coating receives the highest concentration of radiation dose, with a secondary distribution extending into the underlying substrate.

For further investigations on the irradiation impact on our coatings, the samples with 0%, 8% and 10% of Al concentration were selected. Both as-deposited and irradiated coatings passed the MIL-C-48616 standard. After completing adhesion (4.6.8.1), humidity (4.6.8.2), abrasion (4.6.8.3) and temperature (4.6.9.1) durability tests, coatings did not show any signs of deterioration such as flaking or peeling.

A decrease in reflectance was observed along with the increase of irradiation dose for all investigated concentrations, as shown in Fig. 5. This reflectance decrease (Fig. 5d) is especially pronounced at the 355 and 532 nm wavelengths while at 880 nm, it is nearly not noticeable. The overall light wider range decrease in reflectance is due to accumulation of carbon compounds on the sample

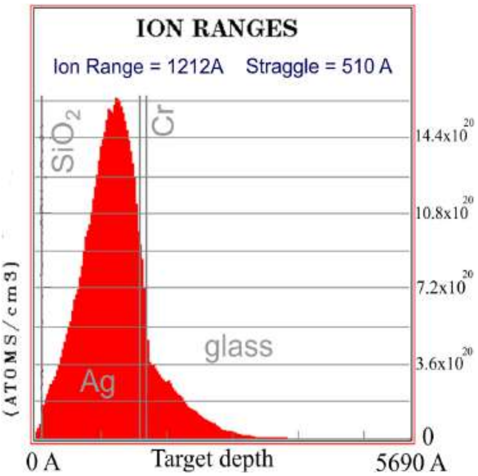

Fig. 4. Depth profile calculations showing the concentrated distribution pattern with the highest ion density occurring within the coating layer and decreasing concentration as ions penetrate into the substrate.

surface during the exposure to the ion bombardment (Wang et al., 2017).

For the reflectance decrease, a detailed surface investigation by AFM was performed. Surface scans are shown in Fig. 6.

As it was previously reported, the Ag-Al phase diagram (Hanson and Anderko, 1958; Hummel, 1981b) shows that for aluminum concentrations in silver ranging from 0 (pure Ag) to about 4 or 5 at.%, the α-phase is dominating. At higher aluminum concentrations, from about 4% to about 18 at.%, the α + μ phases mix is formed. The hexagonal close-packed (hcp) Ag_2Al phase formation was observed (Girka et al., 2017) and stated to be the reason for smoother surfaces of alloyed films.

Formation of cone-like structures and spikes (metal whiskers) like those illustrated in Fig. 6, is commonly observed under light ion plasma bombardment of metal surfaces (Girka et al., 2017; Doerner et al., 2014; Tanyeli et al., 2015) and depends strongly on the surface temperature and ion energy. Metal whiskers growth was studied in detail by Wehner (1985). That study reported that metal whiskers grow independently of ion beam angle and are true growth products, often followed as a seed for cone

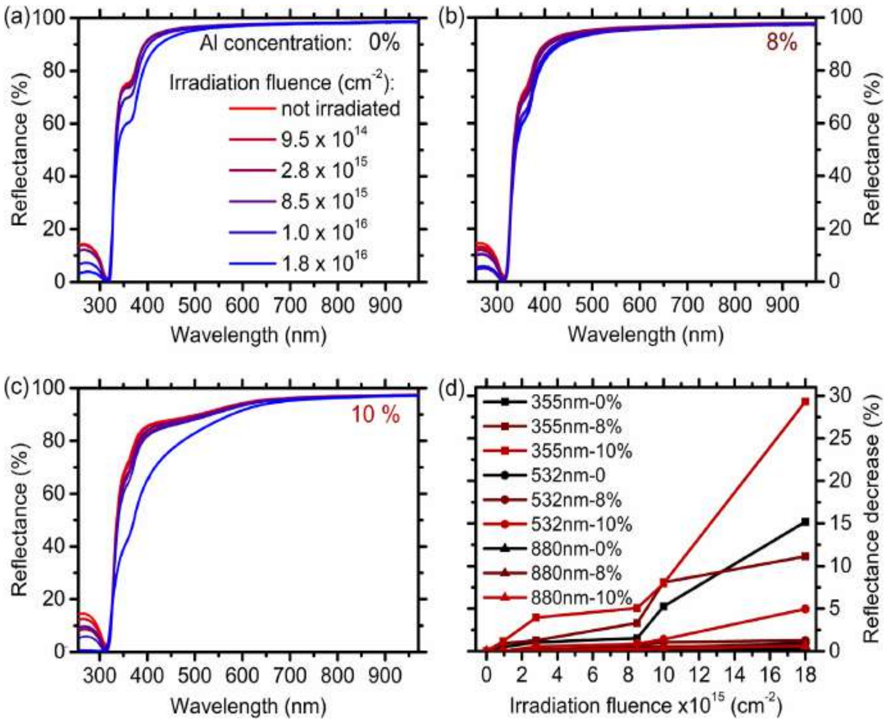

Fig. 5. Reflectance spectra of Ag-Al mixed films with a) 0%, b) 8% and c) 10% Al concentration before and after the irradiation. d) summary of Ag-Al mixed films reflectance decrease at various wavelengths caused by the irradiation.

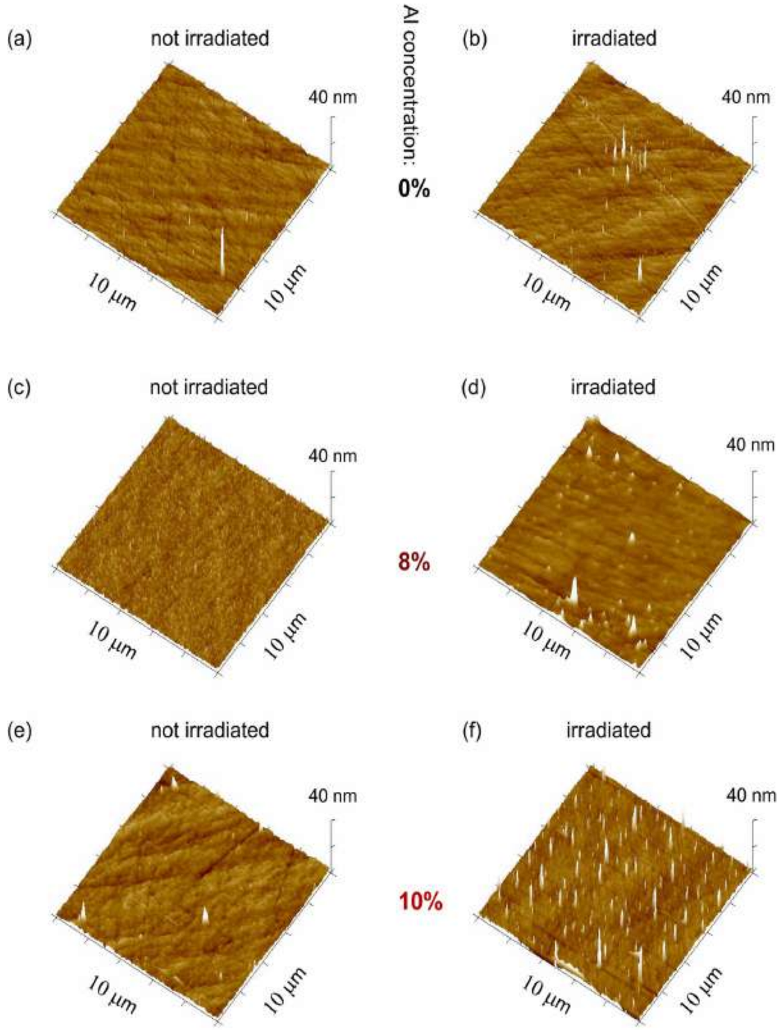

Fig. 6. AFM measurement of Ag-Al mixed films with 0%, 8% and 10% Al concentration before (left) and after (right) irradiation with 20 keV protons at fluency of 1.8×10^{16} cm^{-2}.

structure growth. Metal whiskers tend to form at lower ion energies before their growth becomes overpowered by the ion sputtering effect. In presence of oxygen and nitrogen-free plasma, metal whisker formation is enhanced, as those gases retard surface migration of atoms. Whiskers also grow only when rigid (higher melting point) substrates, particles or atoms are involved. Bombarding with ion energy near the sputtering threshold values, growth of straight single crystal whiskers was reported. Pure (non-mixed) metals should show no cone or whisker formation according to Wehner (1985). In fact, the conical structures observed on our pure silver film after proton bombardment, Fig. 6b, are most probably crystals of salt contaminant, as confirmed by the XPS analysis below (black curve in Fig. 7). Tiny irregularities on a relatively smooth surface may be enhanced during high-dose ion bombardment (Sigmund, 1973). This can occur both due to sputtering erosion and to surface heating and electric charging. While sputtering effect in case of proton irradiation is negligible, heating and charging can make a microscopically

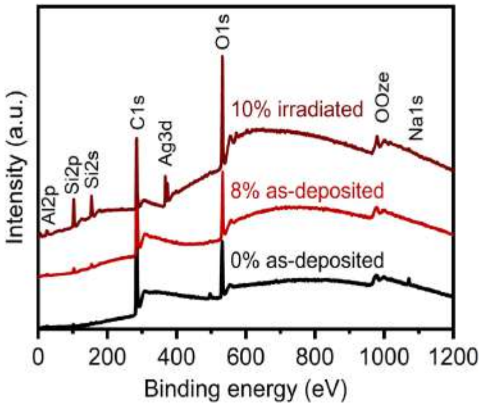

Fig. 7. XPS survey for three samples with different Al concentrations in Ag. The data for the sample with 10% Al in the silver layer middle curve) were acquired after the exposure to the irradiation with 20 keV protons at the fluency of 1.8×10^{16} $cm^{-2.}$

flat metallic surface unstable. The induced silver atom migration causes nanoparticle agglomeration which dominates over the relaxation smoothing effect.

As illustrated in Fig. 6, for the films with Al concentration up to 8%, whiskers formation is still negligible. Therefore, at such low concentrations, whiskers don't contribute significantly to optical scattering and the surface smoothing effect thanks to alloying prevails.

Oxidation of the cones and blisters occurs on the films upon exposure to air. The standard molar enthalpy of formation of $A1_2O_3$ is 1678.2 kJ/mol (Wang et al., 2021) while for Ag_2O it is 30.6 kJ/mol (Wang et al., 2021). Therefore, formation of aluminum oxide is energetically more favorable than that of silver oxide.

The XPS analysis provides an insight to the nature of the observed whiskers and conical structures. The typical probing depth of this technique is about 5 nm for the materials composing our coating. Therefore, the structures grown through the 9 nm-thick capping silica layer are well distinguished from the underlying mirror. Fig. 7 compares the surveys acquired on three samples with different levels of aluminum content: the as-deposited mirror of pure silver (bottom curve), the as-deposited mirror of silver mixed with aluminum at 8% (top curve) and the irradiated mirror of silver mixed with aluminum at 10% (middle curve). Although a detailed analysis of the surface chemistry is out of the scope of this study, we can state that the spectral position of elemental biding energy (BE) and quantification corresponds to the capping layer composition with some residual presence of carbon-containing pollutants. Both as-deposited samples do not show presence on their surfaces of neither silver nor aluminum. The Na1s peak observable in the black curve (BE peak position 1071.4 eV) witnesses the presence of salt crystals due to occasional pollution on the mirror surface, confirming the hypothesis on the origin of the conical structures on pure-silver mirrors illustrated by Fig. 6b.

After the irradiation, the peaks related to silver (Ag3d BE peak position 368.0 eV) and aluminum (BE peak position 75.8 eV) appear. Silicon peaks (Si2p BE peak position 103.5 eV) become relatively higher compared to those of oxygen and carbon and comparable with the silver peaks in height and broadening, indicating a mixed nature of the surface, where all the components have similar weight in the response to the probe, except for aluminum which amount corresponds to the alloying level in the silver layer.

Silica is known to be a sensitive oxide to low-energy protons (Sytchkova et al., 2023; Di Sarcina et al., 2014), while silver is known as a promptly diffusing metal in many oxides with few exceptions, which use as a capping layer would probably protect better the mirrors from whisker growth. In this study, however, we focus on the advantages of metal mixing for the mirror performance, and the film of 9 nm-thick silica acts mainly as a protective capping layer against the atmospheric gases. contribution of this layer to the overall optical absorption increase upon exposure to the proton radiation is negligible as the film is much thinner than the metal layer. Additionally, ion energy was choicen to ensure main ion implantation to the metal layer material. Thanks to this choice, we are able to find out silver alloying with aluminum further increases diffusing properties of silver.

4. Conclusions

We investigated Ag-Al mixed films with Al concentration varying from 0 to 15% and protected with a SiO_2 capping layer for their resistance to low-energy proton radiation at fluences typical for low-Earth orbits missions. We compared their optical properties and surface morphology before and after irradiation.

The addition of aluminum to silver films produces beneficial changes in surface morphology. While the surface roughness decreases with increasing aluminum concentration, the specular reflectance in the UV range slightly decreases due to enhanced electron-to-atom ratios and potential formation of intermetallic phases. Possible formation of a hcp Ag_2Al phase helps tailoring the film microstructure and improves significantly the optical scattering from the as-deposited films.

Ion irradiation testing using 20 keV H^- ions at fluences up to 1.8×10^{16} cm^{-2} revealed significant differences in radiation tolerance among the studied compositions. All samples experienced reflectance degradation in the UV range (320–500 nm), with the effect becoming more pronounced at 10% aluminum concentration. Post-irradiation surface analysis revealed the formation of cone-like structures and whiskers, phenomena characteristic of light ion bombardment of metal surfaces.

The aluminum doping at 8% represents the optimal balance between the optical performance, surface quality, and radiation tolerance. Although higher aluminum concentrations provide superior surface smoothness, such films have lower radiation resistance and their optical performance worsens over the wavelength ranges critical for space communication applications.

Declaration of competing interest

The authors declare the following financial interests/personal relationships which may be considered as potential competing interests: Alexandr Belosludtsev reports financial support was provided by Research Council of Lithuania. Anna Sytchkova reports financial support was provided by Italian Space Agency. If there are other authors, they declare that they have no known competing financial interests or personal relationships that could have appeared to influence the work reported in this paper.

Acknowledgment

We would like to thank Vitalija Jasulaitiene for XPS measurement. This work has received funding from the Research Council of Lithuania (LMTLT), agreement No [S-MIP-24-15] and was carried out within the Space It Up! project funded by the Italian Space Agency (ASI) and the Italian Ministry of University and Research (MUR) under contract No. 2024-5-E.0, CUP No. I53D24000060005.

References

Adams, R.O., Nordin, C.W., Fraikor, F.J., Masterson, K.D., 1979. Co-sputtering of aluminum–silver alloy mirrors for use as solar reflectors. Thin Solid Films 63, 151–154. https://doi.org/10.1016/0040-6090(79)90116-0.

Appleget, C.D., Folgner, K.A., Wissuchek, F., Dunscombe, S.L., Adams, P.M., Sitzman, S.D., Lingley, Z.R. and Barrie, J.D., 2022. Impact of aluminum alloying for improved optical performance in thick silver films, in Optical Interference Coatings Conference (OIC), R. Sargent and A. Sytchkova, eds., Technical Digest Series (Optica Publishing Group, 2022), paper FB.1; https://doi.org/10.1364/OIC.2022.FB.1.

Atad-Ettedgui, E., Dierickx, P., 2004. Optical fabrication, metrology, and material advancements for telescopes. Proc. SPIE 5494, Optical Fabrication, Metrology, and Material Advancements for Telescopes.

Bakar, A.A., Hashim, N.H., Tajuddin, H.A., Sadun, A.S., Abidin, Z.H. Z., 2025. Eliminating adhesive layers in silver metallization: a comparative study of glass cleaning methods for enhanced hydroxylation and adhesion. Curr. Appl Phys. 71, 138–143. https://doi.org/10.1016/j.cap.2025.01.002.

Belosludtsev, A., Sytchkova, A., Baltrusaitis, K., Vaicikauskas, V., Jasulaitienė, V., Gric, T., 2023. Growth of magnetron-sputtered ultrathin chromium films: in situ monitoring and ex situ film properties. Coatings 13, 347. https://doi.org/10.3390/coatings13020347.

Bondarev, A.V., Golizadeh, M., Shvyndina, N.V., Shchetinin, I.V., Shtansky, D.V., 2017. Microstructure, mechanical, and tribological properties of Ag-free and Ag-doped VCN coatings. Surf. Coat. Technol. 331, 77–84. https://doi.org/10.1016/j.surfcoat.2017.10.036.

Chapman, J.C., Peters, N.A., 2022. Paving the way for satellite quantum communications. Physics 15, 172. https://doi.org/10.1103/Physics.15.172.

Corso, A.J., Padovani, M., Santi, G., Hübner, R., Kentsch, U., Bazzan, M., Pelizzo, M.G., 2024. Optical thin films in space environment: investigation of proton irradiation damage. ACS Appl. Mater. Interfaces 16, 38645–38657.

De Silva, K.S.B., Keast, V.J., Gentle, A., Cortie, M.B., 2017. Optical properties and oxidation of α-phase Ag–Al thin films. Nanotechnology 28, 095202. https://doi.org/10.1088/1361-6528/aa5782.

Di Sarcina, I., Grilli, M.L., Menchini, F., Piegari, A., Scaglione, S., Sytchkova, A., Zola, D., 2014. Behavior of optical thin-film materials and coatings under proton irradiation. Appl. Opt. 53, A314–A320.

Doerner, R.P., Baldwin, M.J., Nishijima, D., 2014. Plasma-induced morphology of beryllium targets exposed in PISCES-B. J. Nucl. Mater. 455, 1–4. https://doi.org/10.1016/j.jnucmat.2014.02.010.

Formica, N., Ghosh, D.S., Carrilero, A., Lai Chen, T., Simpson, R.E., Pruneri, V., 2013. Ultrastable and atomically smooth ultrathin silver films grown on a copper seed layer. ACS Appl. Mater. Interfaces 5, 3048–3053. https://doi.org/10.1021/am303147w.

Garoli, D., De Marcos, L.V.R., Larruquert, J.I., Corso, A.J., Proietti Zaccaria, R., Pelizzo, M.G., 2020. Mirrors for space telescopes: degradation issues. Appl. Sci. 10, 7538. https://doi.org/10.3390/app10217538.

Girka, O., Bizyukov, O., Bogatyrenko, S., Bizyukov, I., 2017. Aluminium surface morphology behaviour under high-flux helium ion bombardment. Nucl. Instrum. Methods Phys. Res., Sect. B: Beam Interact. Mater. Atom 405, 31–35. https://doi.org/10.1016/j.nimb.2017.05.019.

Gu, D., Zhang, C., Wu, Y.-K., Guo, L.J., 2014. Ultrasmooth and thermally stable silver-based thin films with subnanometer roughness by aluminum doping. ACS Nano 8, 10343–10351. https://doi.org/10.1021/nn503577c.

Hanson, M., Anderko, K., 1958. Constitution of Binary Alloys. McGraw-Hill, New York.

Harris, L., Siegel, B.M., 1948. A method for the evaporation of alloys. J. Appl. Phys. 19, 739–741. https://doi.org/10.1063/1.1698199.

Hass, G., 1949. On the preparation of hard oxide films with precisely controlled thickness on evaporated aluminum mirrors. J. Opt. Soc. Am. 39, 532–540. https://doi.org/10.1364/JOSA.39.000532.

Hausner, M., 2019. In: Specifications and Standards for Optical Coating Durability. https://doi.org/10.1117/3.2537932.

Heaney, J.B., Kauder, L.R., Freese, S.C., Quijada, M.A., 2012. Preferred mirror coatings for UV, visible, and IR space optical instruments. In: Proc. SPIE 8510, Earth Observing Systems XVII, pp. 167–177. https://doi.org/10.1117/12.931005.

Hernandez, T., Moroño, A., Hodgson, E.R., 2005. Radiation enhanced degradation of SiO overcoated aluminium mirrors. Fusion Eng. Des. 74, 793–796. https://doi.org/10.1016/j.fusengdes.2005.06.098.

Hu, G., He, H., Sytchkova, A., Zhao, J., Shao, J., Grilli, M., Piegari, A., 2017. High-precision measurement of optical constants of ultra-thin coating using surface plasmon resonance spectroscopic ellipsometry in Otto-Bliokh configuration. Opt. Express 25, 13425–13434.

Huber, E., Marinero, E.E., 1988. Magneto-optical activity of Ag at the plasma frequency. Appl. Phys. A 47, 131–135. https://doi.org/10.1007/BF00618877.

Hummel, R.E., 1981a. Reflectivity of silver- and aluminium-based alloys for solar reflectors. Sol. Energy 27, 449–455.

Hummel, R.E., 1981b. Differential reflectometry of sputtered silver–aluminum films between 1.6 and 6.2 eV. Opt. Commun. 39, 55–58. https://doi.org/10.1016/0030-4018(81)90454-5.

Jacobson, M.R., Kneale, R.C., Gillett, F.C., Raybould, K., Filhaber, J.F., Carniglia, C.K., et al., 1998. Development of silver coating options for the Gemini 8-m telescopes project. In: Proc. SPIE 3352, Advanced Technology Optical Telescopes VI, pp. 477–502. https://doi.org/10.1117/12.319269.

Johnson, P.B., Christy, R.W., 1972. Optical constants of the noble metals. Phys. Rev. B 6, 4370–4379. https://doi.org/10.1103/PhysRevB.6.4370.

Juškevičius, K., Audronis, M., Subačius, A., Kičas, S., Tolenis, T., Buzelis, R., et al., 2015. Fabrication of Nb_2O_5/SiO_2 mixed oxides by reactive magnetron co-sputtering. Thin Solid Films 589, 95–104.

Navabpour, P., Ostovarpour, S., Hampshire, J., Kelly, P., Verran, J., Cooke, K., 2014. The effect of process parameters on the structure, photocatalytic and self-cleaning properties of TiO_2 and Ag–TiO_2

coatings deposited using reactive magnetron sputtering. Thin Solid Films 571, 75–83. https://doi.org/10.1016/j.tsf.2014.10.040.
Palik, E.D., 1985. Handbook of Optical Constants. Academic Press, San Diego.
Sheikh, D.A., Connell, S.J., Dummer, R.S., 2008. Durable silver coating for Kepler Space Telescope primary mirror. In: Proc. SPIE 7010, Space Telescopes and Instrumentation 2008: Optical, Infrared, and Millimeter, 70104E. https://doi.org/10.1117/12.789996.
Sidhu, J.S., Joshi, S.K., Gündoğan, M., Brougham, T., Lowndes, D., Mazzarella, L., et al., 2021. Advances in space quantum communications. IET Quant. Commun. 2, 182–217. https://doi.org/10.1049/qtc2.12015.
Sigmund, P., 1973. Mechanism of surface micro-roughening by ion bombardment. J. Mater. Sci. 8, 1545–1553. https://doi.org/10.1007/BF00754888.
Song, M.-G., Kim, K.-S., Yang, H.I., Kim, S.-K., Kim, J.-H., Han, C.-W., et al., 2020. Highly reliable and transparent Al-doped Ag cathode fabricated using thermal evaporation for transparent OLED applications. Org. Electron. 76, 105418. https://doi.org/10.1016/j.orgel.2019.105418.
Sytchkova, A., Grilli, M.L., Rinaldi, A., Vedraine, S., Torchio, P., Piegari, A., Flory, F., 2013a. Radio frequency sputtered Al:ZnO-Ag transparent conductor: A plasmonic nanostructure with enhanced optical and electrical properties. J. Appl. Phys. 114 (9) 094509.
Sytchkova, A., 2013b. 5 - Complex materials with plasmonic effects for optical thin film applications. Optical Thin Films and Coatings, 133–176. https://doi.org/10.1533/9780857097316.2.133.
Sytchkova, A., Schwinde, S., Protopapa, M.L., Palmisano, M., Piegari, A., Schürmann, M., Kaiser, N., 2018. Optical characterisation of silver mirrors protected with transparent overcoats. In: Proc. SPIE 10691, Advances in Optical Thin Films VI. https://doi.org/10.1117/12.2312077.
Sytchkova, A., Belosludtsev, A., Volosevičienė, L., Juškėnas, R., Simniškis, R., 2021. Optical, structural and electrical properties of sputtered ultrathin chromium films. Opt. Mater. 121, 111530. https://doi.org/10.1016/j.optmat.2021.111530.
Sytchkova, A.M.L., Grilli, A., Rinaldi, S., Vedraine, P.T., et al., 2013. Radio frequency sputtered Al: ZnO-Ag transparent conductor: a plasmonic nanostructure with enhanced optical and electrical properties. J. Appl. Phys. 114, 094509. https://doi.org/10.1063/1.4820266.
Sytchkova, A., Protopapa, M.L., Olivero, P., Tapfer, L., Burresi, E., Dunatov, T., Siketic, Z., Palmisano, M., Pesce, E., Wang, Y., Wang, Z., He, H., 2023. Optical characterization of the impact of 100 keV protons on the optical properties of ZrO2 films prepared by ALD on fused silica substrates. Appl. Opt. 62, B182–B187. https://doi.org/10.1364/AO.477965.
Sytchkova, A., Protopapa, M.L., Kolev, H., Burresi, E., Olivero, P., Dunatov, T., Siketić, Z., Tapfer, L., Wang, Z., He, H., Wang, Y., 2024a. Impact of proton irradiation on photoluminescent properties of C doped ZrO_2 films prepared by ALD. Vacuum 224, 113083. https://doi.org/10.1016/j.vacuum.2024.113083.
Sytchkova, A., Protopapa, M.L., Olivero, P., Shen, Z., Wang, Y., 2024b. On the representativeness of proton radiation resistance tests on optical coatings for interplanetary missions. Coatings 14, 898. https://doi.org/10.3390/coatings14070898.
Tanyeli, İ., Marot, L., Mathys, D., et al., 2015. Surface modifications induced by high fluxes of low energy helium ions. Sci. Rep. 5, 9779. https://doi.org/10.1038/srep09779.
Thomas, N.L., Wolfe, J.D., Farmer, J.C., 1998. Protected silver coating for astronomical mirrors. In: Proc. SPIE 3352, Advanced Technology Optical Telescopes VI, pp. 580–586. https://doi.org/10.1117/12.319243.
Vucina, T., Boccas, M., Araya, C., Hee, C.A., Cavedoni, C., 2008. Gemini primary mirror in situ wash. In: Proc. SPIE 7012, Ground-Based and Airborne Telescopes II, pp. 1059–1071. https://doi.org/10.1117/12.788388.
Wang, D., Hauptmann, J., May, C., Hofstetter, Y.J., Vaynzof, Y., Müller, T., 2021. Roll-to-roll fabrication of highly transparent Ca:Ag top-electrode towards flexible large-area OLED lighting application. Flex. Print. Electron. 6, 35001. https://doi.org/10.1088/2058-8585/abf159.
Wang, D., Qu, Z., Wang, Y., Liu, J., Wang, Q., 20233a. Effects of Al-doping concentration on the structure and electromagnetic shielding properties of transparent Ag thin films. Opt. Mater. 135, 113353. https://doi.org/10.1016/j.optmat.2022.113353.
Wang, D., Cheng, E., Qu, Z., Wang, Y., Wang, Q., 2024. The enhancement in microstructure, optical and electromagnetic shielding properties of Al-doped Ag thin films by annealing treatment. Surf. Interfaces 54, 105172. https://doi.org/10.1016/j.surfin.2024.105172.
Wang, J., Toloczko, M.B., Kruska, K., Schreiber, D.K., Edwards, D.J., Zhu, Z., Zhang, J., 2017. Carbon contamination during ion irradiation—accurate detection and characterization of its effect on microstructure of ferritic/martensitic steels. Sci. Rep. 7, 1–12. https://doi.org/10.1038/s41598-017-15669-y.
Wang, Z., Wang, Y., He, H., Sytchkova, A., Shen, Z., Protopapa, M.L., Zhang, Y., Chen, C., Chen, Y., Lu, Y., Zhu, M., Shao, Y., Shao, J., 2023b. Effect of residual impurities on the behavior and laser-induced damage of oxide coatings exposed to deep-space radiation. Opt. Mater. 140, 113838. https://doi.org/10.1016/j.optmat.2023.113838.
Weaver, C., Brown, L.C., 1968. Diffusion in evaporated films of silver–aluminium. Philos. Mag. A: Theor. Exp. Appl. Phys. 17, 881–897. https://doi.org/10.1080/14786436808223171.
Wehner, G.K., 1985. Cone formation as a result of whisker growth on ion-bombarded metal surfaces. J. Vac. Sci. Technol. A 3, 1821–1835. https://doi.org/10.1116/1.573386.
Wulff, J., 1934. The reflectivity of intermetallic systems. J. Opt. Soc. Am. 24, 223–226. https://doi.org/10.1364/JOSA.24.000223.
Yang, M., Gatto, A., Kaiser, N., 2006. Highly reflecting aluminum-protected optical coatings for the vacuum-ultraviolet spectral range. Appl. Opt. 45, 178–183. https://doi.org/10.1364/AO.45.000178.
Zhang, C., Zhao, D., Gu, D., Kim, H., Ling, T., Wu, Y.R., et al., 2014. An ultrathin, smooth, and low-loss Al-doped Ag film and its application as a transparent electrode in organic photovoltaics. Adv. Mater. 26, 5696–5701. https://doi.org/10.1002/adma.201306091.
Zhang, C., Kinsey, N., Chen, L., Ji, C., Xu, M., Ferrera, M., et al., 2017. High-performance doped silver films: overcoming fundamental material limits for nanophotonic applications. Adv. Mater. 29, 1605177. https://doi.org/10.1002/adma.201605177.
Ziegler, J.F., Ziegler, M.D., Biersack, J.P., 2010. SRIM – the stopping and range of ions in matter (2010). Nucl. Instrum. Methods Phys. Res., Sect. B: Bean Interact. Mater. Atom 268, 1818–1823. https://doi.org/10.1016/j.nimb.2010.02.091.

C. Reflectivity improvement of lightweight active cooled metal mirrors manufactured by additive manufacturing

I. Bitinaitis, K. Stravinskas, S. Borodinas, G. Mordas,
A. Belosludtsev

Optical Materials 169 (2026) 117570

Contents lists available at ScienceDirect

Optical Materials

journal homepage: www.elsevier.com/locate/optmat

Research Article

Reflectivity improvement of lightweight active cooled metal mirrors manufactured by additive manufacturing

Ignas Bitinaitis [a], Karolis Stravinskas [a], Sergejus Borodinas [b], Genrik Mordas [a], Alexandr Belosludtsev [a,*]

[a] Department of Laser Technologies, Center for Physical Sciences and Technology, Savanoriu Ave. 231, Vilnius, 02300, Lithuania
[b] Department of Applied Mechanics, Vilniaus Gedimino Technikos Universitetas, Vilnius, 10223, Lithuania

ARTICLE INFO

Keywords:
High reflective mirrors
Additive manufacturing
Selective laser melting
Polishing
Magnetron sputtering
Laser optics

ABSTRACT

In recent years, additive manufacturing (AM) has appeared as a revolutionary approach in designing and fabricating active-cooled mirrors (ACMs). In particular, selective laser melting (SLM) allows more design freedom (with high resolution) while reducing weight and material costs compared to conventional manufacturing methods. In the current research, SLM using a Ytterbium fiber laser (200 W, 1030 nm) and a high-speed scanner for precise active cooled mirror base manufacturing was used. Nevertheless, without a proper surface finish, the metal surface has relatively low reflectance. This limits the use of element for laser and space-based applications. In the present research, we show how HR silver-aluminum (Ag–Al) mixed coating deposited using magnetron sputtering may help. The final element reflectance was increased up to >95 % in the vis-IR range and the arithmetic average roughness was less than 3–5 nm. Optical performance and surface quality were evaluated in each manufacturing step. Fabricated coatings' properties are compared with those used in earlier space missions to assess their main parameters. Additive manufacturing approach successfully enabled the integration of complex internal cooling channels that cannot be achieved through conventional machining methods, providing a foundation for enhanced thermal management in high-power optical applications.

1. Introduction

In recent years, additive manufacturing (AM) has appeared as a revolutionary approach in designing and fabricating lightweight active-cooled mirrors (ACMs), with more design freedom while reducing weight and material costs compared to conventional manufacturing methods [1]. The development of mirrors that are lightweight, highly stable, and thermally efficient has been increasingly in demand for high-performance mirrors for space telescopes, adaptive optics, and laser systems, while the manufacturing technology challenge is calling for advanced solutions. Selective Laser Melting (SLM), also known as Laser Powder Bed Fusion (L-PBF/M) or Direct Metal Laser Sintering (DMLS), is one of the most widely used AM techniques that enables the creation of complex geometries, such as lattice structures and embedded cooling channels [2]. These features significantly enhance thermal performance by optimizing cooling paths directly within the mirror structure.

The integration of internal cooling channels, facilitated by AM, is crucial for managing thermal loads and minimizing deformations caused by temperature fluctuations. This capability is particularly beneficial in optical systems that require precise stability under varying thermal conditions. Unlike traditional fabrication methods that rely on external cooling solutions, AM enables the creation of intricate internal cooling geometries without additional assembly, reducing weight and enhancing durability [3].

Material selection is vital for any AM-based design of ACMs since the type of material employed determines the thermal conductivity, strength, and stability of the materials involved in the process. In this work, the material 17-4 PH stainless steel was selected for its properties, including high strength, good thermal conductivity, and corrosion resistance [4]. Compared to traditional materials such as aluminium, 17-4 PH stainless steel offers superior advantages under thermal cycling conditions, where structural integrity and thermal efficiency are demanded [5]. This material also supports the AM production of high-precision mirror structures with internal cooling channels capable of handling substantial heat loads while maintaining stability.

* Corresponding author.
E-mail address: Alexandr.Belosludtsev@ftmc.lt (A. Belosludtsev).

https://doi.org/10.1016/j.optmat.2025.117570
Received 29 May 2025; Received in revised form 4 September 2025; Accepted 27 September 2025
Available online 29 September 2025

Conventional manufacturing methods, such as machining and assembly, face inherent limitations in producing lightweight mirrors with integrated cooling solutions. These methods often add bulk due to the need for external cooling components and involve multiple assembly stages, resulting in increased weight and additional points of potential failure [6]. In contrast, AM provides a promising alternative by enabling the fabrication of compact and efficient ACMs. For instance, computational fluid dynamics (CFD) simulations have been applied to optimize the design of cooling channels within AM-produced mirrors, achieving substantial thermal stability improvements not feasible with traditional manufacturing methods.

To meet the evolving demands of ACM technology, the next generation of designs must address three critical areas: weight reduction, high thermal conductivity, and enhanced reflectance. Aerospace applications require weight reduction to improve mobility and efficiency. High thermal stability, achievable through materials such as 17-4 PH stainless steel, is also crucial for preserving optical accuracy by preventing thermal deformations [7]. Finally, ACMs must exhibit high reflectance to ensure efficient light management in optical systems. AM's capability to create lightweight structures with integrated cooling channels makes it an ideal solution for fulfilling these requirements.

There are several benefits of using metallic alternatives to glass mirrors [8]. The development of lightweight, actively cooled mirrors represents a critical advancement in space-based optical systems, particularly for large-scale telescopes aimed at detecting and characterizing exoplanets. These innovative mirror systems address several key challenges inherent in space telescope design, including mass constraints, thermal stability, and optical performance. By reducing overall mass while maintaining structural integrity, lightweight mirrors facilitate the deployment of larger apertures, thereby enhancing the telescope's light-gathering capability and resolution. Active cooling mechanisms, integrated into these mirror systems, play a crucial role in mitigating thermal distortions that can compromise image quality [9,10]. This thermal management is especially vital for infrared observations, where even minute temperature fluctuations can significantly impact data collection. The synergy between lightweight design and active cooling not only optimizes the telescope's performance but also extends its operational lifespan by minimizing thermal stress on critical components.

Although additive manufacturing allows for the production of complex geometries and integrated cooling channels, achieving the optical quality required for high-precision applications remains a challenge [11]. The surface roughness of AM-produced mirrors is generally higher than that of conventionally machined optics, making post-processing essential. Methods such as diamond turning [12,13], chemical polishing [14,15], and ion beam figuring [16] are commonly used to refine the surface and improve reflectance. Additional coatings might be applied to further enhance optical performance, ensuring that AM-fabricated mirrors meet optical requirements for laser and space-based applications. Post-processing techniques, including hot isostatic pressing combined with aluminum coating, have shown promising results in reducing surface roughness from typical AM values to an arithmetic average roughness below 2 nm [40]. In contrast, the electrolyte plasma polishing (EPP) technique achieved a final visible surface roughness value of 1.28 μm on selective laser melted 17-4 PH steel components [41]. While the laser polishing technique applied to LPBF AlSi10Mg parts achieved a surface roughness value as low as 0.32 μm, depending on the fabrication angle and laser parameters [42].

In our previous research [17], Ag–Al mixed coatings for space optics were developed. It was shown that, depending on Al concentrations in Ag–Al coating, mixing Al with Ag can enhance some of the properties that pure Ag films are lacking [18]. For example, with low Al concentrations, Ag–Al film is resistant to oxidation in air with minimal losses in reflectance [19]. In our previous research, 8 % Al mixing led to a surface roughness reduction compared to a pure Ag mirror. Moreover, we showed that such an HR coating may withdraw orbital radiation.

This study demonstrates the possibility of combining laser manufacturing and optical coating technologies for effective optical component engineering. Firstly, the geometric configuration of the actively cooled metallic mirror with internal cooling channels was designed. The efficiency of the cooling system was calculated. Secondly, an active cooled mirror structure was prepared using additive manufacturing. Further, the surface preparation and deposition of an optimized high-reflective coating were discussed. Optical performance is evaluated in each surface post-processing step. Finally, our HR coating surface properties are compared with those used in earlier space missions to assess their suitability.

2. Experimental details

2.1. Mirror design and manufacturing

The design of the mirror structure was carried out using Solidworks 2024 software. It was focused on creating a lightweight yet stable mirror optimized for integration with an active cooling system. After the design was finalized, an air flowability test using COMSOL Multiphysics software was conducted. It was done to validate the coolant's stable circulation within the Archimedean spiral channels, as it was shown the Archimedean spiral channel exhibits a better thermal performance at lower Reynolds numbers [20]. The material selected for this study was 17-4 PH stainless steel, a high-strength, precipitation-hardened stainless steel alloy known for its excellent thermal conductivity, corrosion resistance, and durability. These properties make 17-4 PH stainless steel particularly suitable for high-precision optical applications requiring stability under thermal stress. The powder used in the Selective Laser Melting (SLM) process was produced by Carpenter Additive. To ensure optimal performance in SLM, the powdered form of 17-4 PH stainless steel was carefully prepared to achieve a uniform particle size and distribution, which is essential for consistent melting and solidification. The composition of 17-4 PH stainless steel powder used in this work is detailed in Table 1. It shows the chemical composition of the alloy that meets the international ASTM standard for the 17-4 PH stainless-steel [21].

The mirror structure was fabricated using an EOS M280 SLM machine (EOS GmbH—Electro Optical Systems, Krailling, Germany), a high-precision system designed for the additive manufacturing of metal components. The EOS M280 is equipped with a 200 W, 1030 nm Ytterbium (Yb) fiber laser and a high-speed scanner with a precision galvanometer (11 μrad) and temperature compensation, which enables stable laser delivery. The laser is focused using an F-theta lens that maintains a consistent beam spot size across the build area. For this process, a focused laser spot size of 100 μm was used to ensure precision in fine details. The mirror was built layer by layer with a powder layer thickness of 40 μm, ensuring fine resolution and high surface quality. Fabrication took place in an inert nitrogen atmosphere on a preheated building platform, maintained at 80 °C to minimize residual stresses during printing. The mirror was constructed in a horizontal orientation, with an angle of 85° relative to the powder scraper's motion, a configuration that helped reduce distortion and ensured dimensional accuracy. A 0.3 mm soft support was used directly on the base plate to stabilize the mirror during the build. After fabrication, the facilitating support was removed. This orientation and support setup optimized the build for accuracy, minimized deformation, and preserved the integrity of the cooling channel design embedded within the mirror structure.

Eight printed mirror surfaces were polished using a Tegramin-25 system (Struers ApS, Denmark). The mirrors were mounted securely and polished sequentially with SiC abrasive papers (#320, #500, #800, #1200), with four samples undergoing further polishing with #4000 grit. Two samples, one polished with #1200 grit and one with #4000 grit abrasive paper, were chosen for further investigation to gain insight into how different polishing levels influence mirror properties before and after applying a high reflectivity coating layer.

Table 1
Chemical composition (at. %) of the 17-4 PH powder.

Element	Fe	Cr	Ni	Cu	Mn	Si	Nb	C
ASTM Standard 17-4 Stainless Steel (UNS S17400, AISI 630)	Bal.	15.0–17.0	3.0–5.0	3.0–5.0	<1.0	<1.0	0.15-0.45	<0.070
Carpenter Additive PowderRange® 17-4 (ASTM A564/A564 M compliant)	Bal.	15.0–17.0	3.0–5.0	3.0–5.0	<1.0	<1.0	–	<0.010

2.2. High reflective coating deposition parameters

All coatings were sputtered using an unbalanced magnetron sources Torus™ in a Kurt J. Lesker sputtering system (PVD225). The sputter system was initially pumped down to a base pressure below 3×10^{-7} Torr. All sputtering targets (Ag, 99.99 %, Cr 99.95 %, Al 99.999 % and Si 99.9999 % purity) were circular planar. The magnetrons were driven by a pulsed direct current (DC) power supply (Advanced Energy Pinnacle Plus) and a radio-frequency (Rf) power supply (Kurt J. Lesker R601). The Rf power supply was operated at 13.56 MHz frequency. All process gases were >99.999 % pure. The argon (Ar) flow rate was 20 sccm, and the pumping speed was adjusted to attain the argon pressure at the same value of 2.2 mTorr. The settings of the Ar flow rate and the pumping speed were not changed during the experiments. Before every experiment, the target was pre-sputtered for 5 min to remove impurities and possible surface oxides. The system was equipped with magnetron and substrate shutters. The experiments were done at room temperature and without substrate biasing. The deposition conditions for the 10 nm chromium (Cr) sublayer are described in Ref. [22]. On top, as a protective layer, 9 nm of silicon dioxide (SiO_2) was deposited. The oxide deposition conditions are described in Ref. [23]. The sublayer, Ag–Al layer, and protection layer thicknesses were the same for all the samples. The schematic drawing of the coating structure is introduced in Fig. 1.

The 150 nm Ag–Al layers were sputtered by using Rf power supply for Al and pulsed DC power supply for Ag simultaneously. The Ag (pulsed-DC) power was fixed to 200 W and for Al (Rf) the power was 30 W (8 %). In brackets is written the calculated volume percentage of Al in Ag–Al layers. Such an optimized composition was developed in a separate research [17]. Deposition rates were calibrated, and deposition times were correlated in order to reach the desired layer thickness and concentration. The coatings were deposited on machine-polished additive-manufactured structures of 25.4 mm diameter and 155 mm thickness. Additionally, the 1 mm-thick double-side optically polished fused silica (FS) substrate of 25.4 mm diameter was added in every deposition process as a reference sample.

2.3. Samples investigation techniques

Reflectance spectra were measured in the 220 nm–1500 nm wavelength range using Photon RT spectrophotometer (EssentOptics).

An optical profilometer (Sensofar Metrology) with a 3 × 4 mm scan area was used to measure the initial surface roughness. The SensoView software was used to evaluate the collected data. Areal average roughness (S_a) values have been obtained by measuring surface roughness in accordance with ISO 25178.

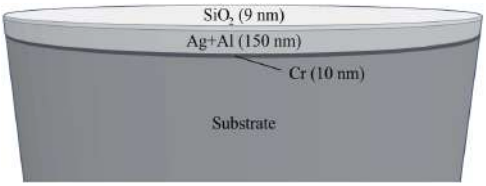

Fig. 1. Schematic drawing of the deposited high reflective (HR) coating. The drawing is not to scale: AM substrate diameter is 25.4 mm and thickness is 155 mm.

Surface topography after polishing and coating was measured using a Dimension Edge (Bruker), Atomic Force Microscope (AFM) in a tapping mode, over a 10 μm × 10 μm scan area. For roughness evaluation, root mean square roughness (R_q) and root mean square roughness (R_a) values were calculated.

The prepared surfaces underwent thorough examination utilizing a dark-field microscope (Leica DM6 M).

3. Results and discussion

3.1. Mirror design and numerical simulations

The geometric configuration of the actively cooled metallic mirror with internal cooling channels and structural details are shown in Fig. 2. The mirror was designed with a diameter of 25.4 mm (1 inch) and a thickness of 155.0 mm. The design contains Archimedean spiral cooling channels underneath the mirror surface with a uniform depth of 2.5 mm and a width of 0.67 mm. The top view shows a spiral channel layout with a central inlet (4.5 mm) for coolant entry and two symmetrical side outlets, 18.9 mm apart, for coolant exit. The spiral design allows for uniform coolant distribution across the mirror surface, minimizing thermal gradients and performance. A 3D cutaway view shows the compact integration of the cooling system within the 21.0 mm thick mirror, maintaining structural and optical integrity. The calculated mirror weighs 41.5 g, which is 34 % less than a solid core metallic mirror of the same size. This weight reduction without compromising mechanical robustness or thermal performance makes this design perfect for aerospace or optical laser systems. The design is optimized for SLM manufacturing, balancing material efficiency and mechanical robustness while having active cooling.

The efficacy of the cooling system is primarily shown by numerical simulations of the thermal and fluid dynamics of an air-cooled metallic mirror exposed to a Gaussian laser beam based on nonisothermal flow multiphysics coupled interfaces. With ambient air supplied at 1 bar and 20 °C, the model assumes a steady-state condition. The airflow enables a directed convective cooling mechanism by entering through lateral inlets and exiting centrally. The temperature distribution and airflow velocity profiles are shown in Fig. 3 for four different operational scenarios: a 200 W laser beam power with a 5 mm spot diameter for two reflective surfaces with reflectance of 60 % and 5 % (Fig. 3a, b respectively) and a 2000 W laser beam power with a 10 mm spot for two reflective surfaces with reflectance of 60 % and 5 % (Fig. 3c, d respectively). The distance from the laser source to the mirror surface is set at 150 mm. The distribution of surface temperatures under conditions of 200 W with HR coating (95 %) is shown in Fig. 3b. Directly beneath the laser spot, the highest temperature measured at the mirror's surface is 45.9 °C. The temperature drops quickly away from the irradiation zone, suggesting effective lateral heat removal. This outcome demonstrates that the cooling system can minimize thermally induced optical distortions or mechanical stresses by keeping temperature gradients within reasonable bounds. Accordingly, the airflow velocity field is depicted in Fig. 3e, where a peak velocity of 249 m/s was noted close to the central exit. Convective heat transfer is concentrated close to the high-flux area thanks to the velocity distribution's efficient air channeling through the cooling ducts. With a laser power of 2000 W and a beam diameter of 10 mm with HR coating (95 %), an increased thermal load is imposed in the second scenario. A peak surface temperature of 88.9 °C and the well-controlled temperature gradient are shown in Fig. 3d. Because the heat is more uniformly dispersed throughout the mirror's surface, this

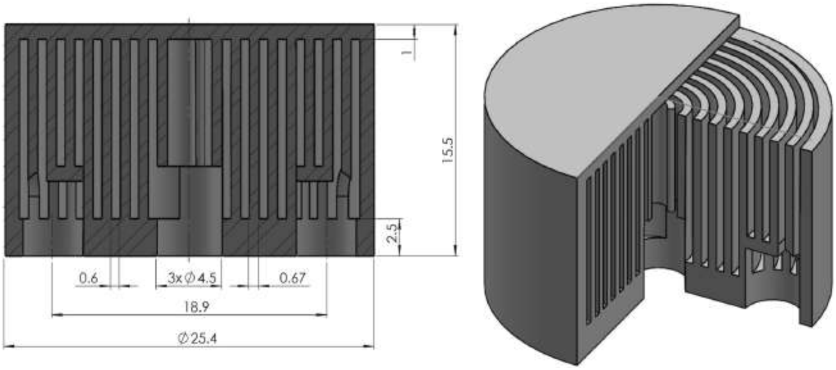

Fig. 2. Geometric configuration of active cooled metallic mirror - side view and isometric view.

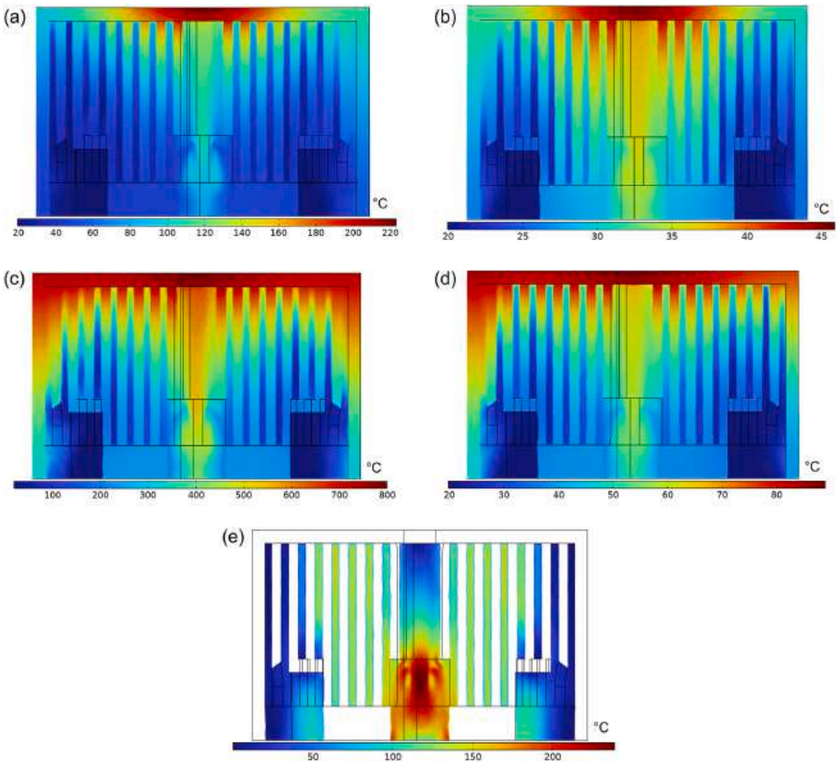

Fig. 3. Temperature (a–d) and airflow (e) distributions of actively cooled metallic mirror at different laser beam power, spot size and reflectance: a) 5 mm, 200 W, 60 %; b) 5 mm, 200 W, 95 %; c) 10 mm, 2000 W, 60 %; d) 10 mm, 2000 W, 95 %.

kind of mirror works well with high-power lasers and broader spot diameters, which is beneficial for maintaining the integrity of optical coatings [24]. An effective reflective optical coating significantly improves the thermomechanical stability and reliability of the proposed system.

3.2. Initial investigation of printed structure

The manufactured mirror (Fig. 4a) had a high degree of geometric accuracy and closely matched the intended design. Nevertheless, there were some minor deviations that were mainly associated with the SLM process's inherent thermal stresses. The manufactured diameter and thickness were 25.42 mm and 15.59 mm, respectively. There were minor variations resulted by powder spreading and thermal expansion during the printing process. The design's main benefit was that it had no external or internal support. Instead, it was supported by the printing platform. An Electrical Discharge Machining (EDM) technology was used to successfully remove the remaining supports, guaranteeing accuracy without adding further mechanical or thermal loads. Fig. 4b as-printed surface roughness was $S_a = 15.8$ µm. Such a surface requires post-processing operations, for example, polishing to satisfy optical application specifications. The mirror manufacturing process took 3 h, which included 1.4 h for laser printing, 0.3 h for post-processing and 1.3 h of coating deposition in a prepared magnetron sputtering chamber. Optical mirrors produced with conventional machining techniques, like CNC milling, have better initial surface quality and frequently don't require as much post-processing. These techniques, however, are not very effective at producing complex interior geometries, like cooling channels, without requiring multi-step assembly [25]. Although diamond turning is a very accurate subtractive manufacturing technique that produces surface finishes on the nanoscale, and it is frequently used for optical mirrors. Nevertheless, it is limited to softer materials like copper alloys and aluminum and requires expensive single-crystal diamond tools [26]. Another widely used method, casting, makes it possible to produce optical mirror blanks in large quantities, but it also introduces substantial porosity and shrinkage problems that require an extensive amount of machining and polishing [27]. Alternatively, SLM made it possible to fabricate intricate internal cooling structures that would be impossible to accomplish with subtractive manufacturing processes. Such an approach significantly reduces material waste when compared to traditional machining or casting. Despite the advantages, post-processing - in particular, polishing and support removal - added time as well as labor expenses, which are important considerations for the viability of large-scale production. These benefits show that the SLM technique is an excellent replacement for producing lightweight, thermally stable optical mirrors. It is especially important for use in laser-based and high-precision optical systems. To fully utilize the advantages of AM in optical applications, future studies should investigate more surface finishing technique optimization and material property improvements.

3.3. Post-processing of printed structure

After printing, the mirror surface was polished. In Fig. 5, the SLM as-printed metallic mirror and the sample after polishing with #4000 grit were compared. It is seen how polishing helped to remove dents and big scratches from the metal surface and created a smooth and shiny appearance. More detailed investigations are described further.

The SLM metallic mirror polishing efficiency was investigated in detail. Traditional manufacturing methods typically employ multiple grinding and polishing steps to achieve the desired surface roughness and reflection [28,29]. Reduction of required processing steps significantly improves production efficiency and technology economic viability.

As the final manufacturing step, samples were coated with the high-reflective (HR) Ag–Al mixed coating. For comparison, samples with different polishing levels were coated. The results of reflectance spectra measurements are introduced in Fig. 6.

In all investigated cases, the HR coating noticeably increases the

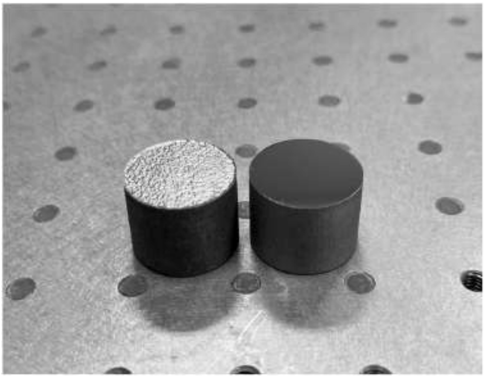

Fig. 5. SLM metal mirror as-printed (left) and after machine polishing (right). The samples diameter and thickness were 25.42 mm and 15.59 mm, respectively.

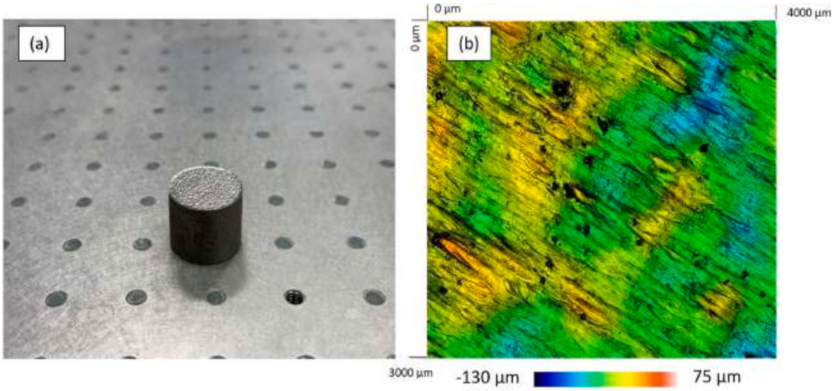

Fig. 4. SLM as-printed metallic mirror: a) general view photo, b) optical profilometer sample surface image. The sample diameter and thickness were 25.42 mm and 15.59 mm, respectively.

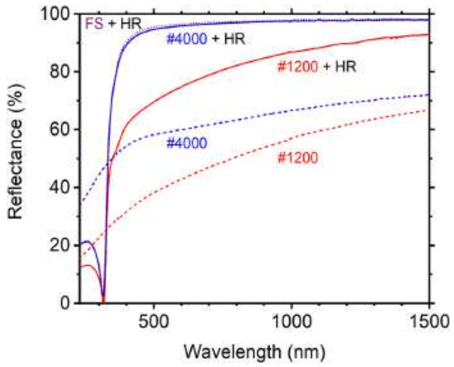

Fig. 6. Reflectance spectra of SLM metal mirror polished with #1200 grit and #4000 grit before and after high reflective (HR) coating deposition. Spectra of HR coated double-sided optically polished fused silica (FS) substrate are shown as reference.

samples' reflectivity. The pronounced reflectance dip observable at the 320 nm wavelength is attributed to the surface plasmon resonance phenomenon. Transmittance measurement of the silver surface plasmon resonance region (310–330 nm) is often employed as a reliable tool to perform diagnostic Ag film quality checks [30]. The best results were observed for HR coated SLM metal mirror polished with #4000 grit. Reflectance difference from reference coated fused silica (FS) sample is less than 1 % in the measurement range of 220–1500 nm. On the other hand, reflectance measurements of #1200 grid polished samples show poor correlation with the reference FS sample, exhibiting discrepancies of up to 60 %. This substantial deviation suggests that the surface preparation method significantly influences the optical characteristics of the deposited films, with machine polishing yielding more consistent and predictable results. So, polishing with #1200 grit left visible scratches, while #4000 grit achieved a smoother, reflective finish suitable for optical applications.

The surface morphology of machine-polished samples was investigated using a dark-field microscope (Leica DM6 M) before and after thin film deposition, see Fig. 7. Comparative analysis of the micrographs obtained before and after HR deposition revealed a significant reduction in the observable scratch density on the sample surfaces. This observation suggests that the coating deposition effectively mitigates surface imperfections, potentially through a planarization effect or by filling in microscopic scratches.

SLM metal mirror surface topography (Fig. 8) and surface roughness were evaluated using AFM before and after HR coating deposition. The arithmetic average roughness (R_a) was calculated to evaluate changes in surface morphology.

Analysis of the AFM data revealed a minor decrease in surface roughness after HR coating deposition. The coating process did not significantly impact the underlying substrate topography.

The observed changes are on the order of a few nanometers, which is within the expected range for thin film deposition processes. The consistency in roughness values before and after deposition suggests that the coating technique employed maintains the overall surface characteristics of the substrates.

3.4. *Investigated samples surface quality comparison*

Based on the measured reflectivity and surface roughness of the fabricated samples, the results were further evaluated against the performance parameters of silver mirrors previously employed in space missions (Table 2). Developed final AM structure surface quality demonstrates suitability for freeform geometry designs used in space optics, while maintaining comparable optical and surface properties.

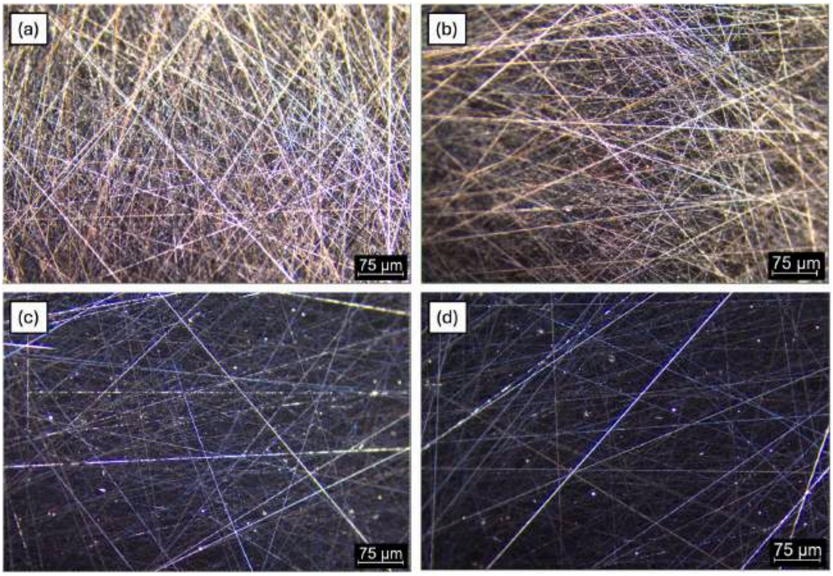

Fig. 7. Optical microscope micrographs of SLM metal mirror surface a) polished with #1200 grit, b) polished with #1200 grit and with high reflective (HR) coating, c) polished with #4000 grit, d) polished with #4000 grit and with HR coating.

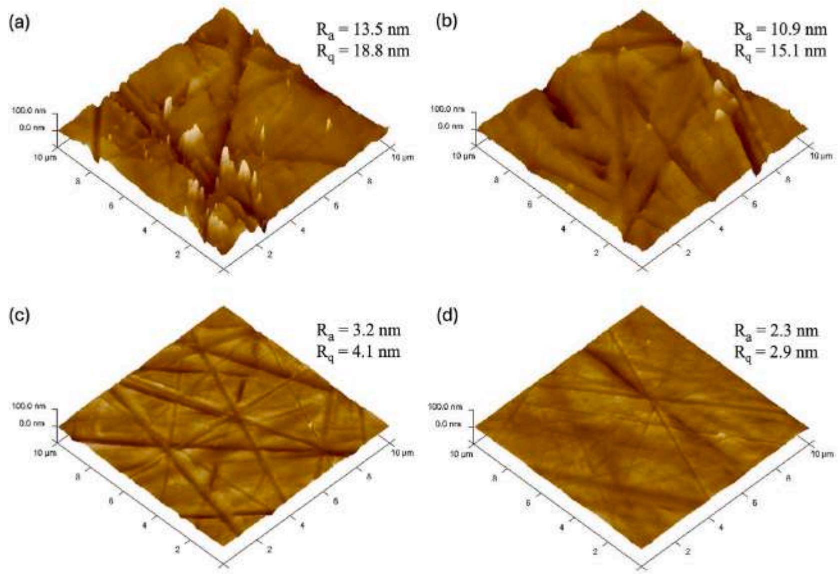

Fig. 8. AFM image of SLM metal mirror surface a) polished with grit #1200, b) polished with grit #1200 with high reflective (HR) coating, c) polished with grit #4000, d) polished with grit #4000 with HR coating.

Table 2
Data comparison of investigated samples surface quality in comparison to other silver based mirrors used in space missions.

Project Name	Reflectance Specifications	Coating Details	Surface Roughness
Kepler Space Telescope [31]	Reflectance >95 % for 400–1200 nm	Durable Ni-CrN_x coating with interference layer for enhanced reflectance.	N/A
Ariel mission [32]	Reflectance >93 % for 600–1000 nm	Protected Ag coating on Ni–Cr adhesion layer	R_q: 3–6.3 nm
Roman Space Telescope [33]	Reflectance >95 % for infrared light	Ag coating 400 nm	R_a: 1.2 nm
Gemini Observatory (Earth) [34–37]	Reflectance 92 % over 0.3–0.7 μm, and 98 % over 0.7–1.1 μm	Protected 4-layer Ag coating on Ni–Cr–Ni adhesion layer	R_a: 1.5–2 nm
Euclid Mission [38,39]	Reflectance N/A, for 0.55–2.1 μm	Protected Ag coating	R_a: <1 nm
Current investigation	Reflectance >95 % for 0.5–1.5 μm	Protected (SiO2) Ag–Al mixed coating on Cr adhesion layer	R_a: 2.3 nm R_q: 2.9 nm

Our fabricated SLM samples demonstrated reflectance exceeding 95 % in the measured 0.5–1.5 μm spectral range, aligning closely with the performance reported for mirrors from the Kepler, Roman, and Ariel missions. While the coating configuration in the current work proved effective in achieving high reflectivity, surface roughness value (R_a: 2.3 nm) remained slightly higher than those reported for mirrors in the Roman and Euclid missions (Ra ≤1.2 nm). These deviations are attributed to surface preparation limitations and highlight the need for further optimization in post-processing techniques to match the optical surface quality. Nonetheless, the obtained parameters remain within a comparable range, indicating the viability of the present approach for future SLM mirror implementation in space-focused optical systems such as free-form mirrors.

4. Conclusions

In the current investigation, an actively cooled metallic mirror with integrated Archimedean spiral channels was successfully designed and manufactured. Cooling performance under high-power laser irradiation was numerically studied. A 34 % weight reduction over a solid mirror is achieved without sacrificing structural integrity due to the spiral channel structure. Such a structure guarantees uniform coolant distribution and minimizes thermal gradients. There is room for further weight reduction for lightweight SLM mirror design or freeform designs if active cooling is not required, preserving identical optical surface properties.

Based on the simulation results, peak SLM mirror surface temperatures under 200 W and 2000 W CW laser loads were respectively 45.9 °C and 88.9 °C beneath the collimated laser spot, while cooling inner channels with 20 °C temperature air at 1 bar pressure. Results show scalability and thermal efficiency of the design, which could prove use in larger or more demanding optical systems.

The SLM as-printed mirror average arithmetic surface roughness was S_a = 15.8 μm, necessitating polishing for optical application. Surface polishing alone was insufficient to achieve high reflectance; the achieved reflectance was below 70 % vis-IR range. After coating, #4000 grit polished AM structures showed significantly higher reflectivity than #1200 grit polished samples. To achieve reflectance above 95 % vis-IR range, both precise polishing (arithmetic average roughness of R_a < 3–5 nm) and deposition of a highly reflective coating (aluminium-silver mixed) are essential.

It is shown that under good planning and preparation, the entire active cooled high reflective metal mirror fabrication can take approximately 3 h.

Final fabricated AM structure surface shows optical performance comparable to mirrors used in recent space missions and holds the prospect to be used in space applications utilizing optimized low-weight or free-form base structure design. Surface reflectivity above 95 % was measured in the 500–1500 nm range with the arithmetic average surface roughness of 2.3 nm.

CRediT authorship contribution statement

Ignas Bitinaitis: Writing – review & editing, Writing – original draft, Visualization, Methodology, Investigation, Data curation. **Karolis Stravinskas:** Writing – review & editing, Writing – original draft, Visualization, Methodology, Investigation. **Sergejus Borodinas:** Visualization, Investigation. **Genrik Mordas:** Writing – review & editing, Writing – original draft, Methodology. **Alexandr Belosludtsev:** Writing – review & editing, Writing – original draft, Supervision, Resources, Project administration, Funding acquisition, Conceptualization.

Declaration of competing interest

The authors declare the following financial interests/personal relationships which may be considered as potential competing interests: Alexandr Belosludtsev reports financial support was provided by Research Council of Lithuania. If there are other authors, they declare that they have no known competing financial interests or personal relationships that could have appeared to influence the work reported in this paper.

Acknowledgment

This project has received funding from the Research Council of Lithuania (LMTLT), agreement No [P-MIP-24-668].

Data availability

Data will be made available on request.

References

[1] Q. Wang, et al., Fabrication strategy of additively manufactured metal mirror based on multi-load topology optimization and single-point diamond turning, J. Optical Eng. (2023), https://doi.org/10.1089/3dp.2023.0106.
[2] P. Hu, H. Zhu, C. He, Optimization design of water-cooled mirror for low thermal deformation, Appl. Therm. Eng. 73 (1) (2014) 598–607, https://doi.org/10.1016/j.applthermaleng.2014.07.052. ISSN 1359-4311.
[3] K. Zhang, H. Qu, H. Guan, J. Zhang, X. Zhang, X. Xie, L. Yan, C. Wang, Design and fabrication technology of metal mirrors based on additive manufacturing: a review, Appl. Sci. 11 (2021) 10630, https://doi.org/10.3390/app112210630.
[4] P. Nezhadfar, M. Masoomi, S. Thompson, N. Phan, N. Shamsaei, Mechanical properties of 17-4 PH stainless steel additively manufactured under Ar and N2 shielding gas, in: Proceedings of the 29th Annual International Solid Freeform Fabrication Symposium—An Additive Manufacturing Conference, August 2018, pp. 13–15. Austin, TX, USA.
[5] W. Chen, B. Xiao, L. Xu, Y. Han, L. Zhao, H. Jing, Additive manufacturing of martensitic stainless steel matrix composites with simultaneously enhanced strength-ductility and corrosion resistance, Compos. B Eng. 235 (2022) 109776, https://doi.org/10.1016/j.compositesb.2022.109776.
[6] B. Zhong, et al., Process chain for ultra-precision and high-efficiency manufacturing of large-aperture silicon carbide aspheric mirrors, Micromachines (2023), https://doi.org/10.3390/mi14040737.
[7] J. Zhang, C. Wang, H. Qu, H. Guan, H. Wang, X. Zhang, X. Xie, H. Wang, K. Zhang, L. Li, Design and fabrication of an additively manufactured aluminum mirror with compound surfaces, Materials 15 (2022) 7050, https://doi.org/10.3390/ma15207050.
[8] Jean-Pierre Rozelot, Jean-M. Leblanc, Metallic alternative to glass mirrors (active mirrors in aluminum): a review, Proc. SPIE 1494, Space Astronomical Telescopes and Instruments (1991), https://doi.org/10.1117/12.46745, 1 September.
[9] C. Zhang, Z. Li, A review of lightweight design for space mirror core structure: tradition and future, Machines 10 (2022) 1066, https://doi.org/10.3390/machines10111066.
[10] M. DiPirro, P. Cleveland, D. Durand, A. Klavins, D. Muheim, C. Paine, K. Walyus, Cooling technology for large space telescopes, in: NSTC 2007/NASA-HQ Science Mission Directorate, 2007, January.
[11] K. Zhang, H. Qu, H. Guan, J. Zhang, X. Zhang, X. Xie, L. Yan, C. Wang, Design and fabrication technology of metal mirrors based on additive manufacturing: a review, Appl. Sci. 11 (2021) 10630, https://doi.org/10.3390/app112210630.
[12] L.H. Li, N.H. Yu, C.Y. Chan, W.B. Lee, Al6061 surface roughness and optical reflectance when machined by single point diamond turning at a low feed rate, PLoS One 13 (4) (2018) e0195083, https://doi.org/10.1371/journal.pone.0195083.
[13] Y. Ma, Z. Li, G. Jin, X. Zhang, L. Li, H. Lin, G. Wang, Z. Long, Investigation on aluminum alloy reflector mirror processing technology combining ultrasonic rolling and single-point diamond turning, Micromachines 15 (2024) 1527, https://doi.org/10.3390/mi15121527.
[14] Y.-T. Jhong, C.-Y. Chao, W.-C. Hung, J.-K. Du, Effects of various polishing techniques on the surface characteristics of the Ti-6Al-4V alloy and on bacterial adhesion, Coatings 10 (2020) 1057, https://doi.org/10.3390/coatings10111057.
[15] Z.F. Ma, L.H. Dong, Y.J. Sun, Y.B. Leng, Z. Chen, Research on chemical mechanical polishing technology of SiC mirror, KEM 552 (2013) 168–173. https://dx.doi.org/10.4028/www.scientific.net/kem.552.168.
[16] A. Majhi, R. Shurvinton, P.C. Pradhan, M. Hand, W. Gu, M.B. Da Silva, S. Moriconi, I. Nistea, S.G. Alcock, H. Wang, K. Sawhney, Sub-nanometre quality X-ray mirrors created using ion beam figuring, J. Synchrotron Radiat. 31 (2024) 706–715, https://doi.org/10.1107/S1600577524004594.
[17] A. Belosludtsev, I. Bitinaitis, J. Želudevičius, V. Kovalevskij, A. Sytchkova, High reflective silver-aluminium mirrors for deep-space quantum communication, Opt. Mater. (2025) submitted for publication.
[18] R.E. Hummel, Differential reflectometry of sputtered silver-aluminum films between 1.6 and 6.2 eV, Opt. Commun. 39 (1–2) (1981) 55–58, https://doi.org/10.1016/0030-4018(81)90454-5.
[19] C. Zhang, N. Kinsey, L. Chen, C. Ji, M. Xu, M. Ferrera, X. Pan, V.M. Shalaev, A. Boltasseva, L.J. Guo, High-performance doped silver films: overcoming fundamental material limits for nanophotonic applications, Adv. Mater. 29 (19) (2017) 1605177, https://doi.org/10.1002/adma.201605177.
[20] Hala Rashad, Younis Najim, Hatem Ismaeel, Hydrothermal analysis of archimedean spiral channel heat sink for CPU cooling. 6, 61-71, https://doi.org/10.18186/thermal.1429128, 2022.
[21] PowderRange 17-4PH Datasheet, Vol. 4548(2000).
[22] Anna Sytchkova, Alexandr Belosludtsev, Lina Vološevičienė, Remigijus Juškėnas, Rimantas Simniškis, Optical, structural and electrical properties of sputtered ultrathin chromium films, Opt. Mater. 121 (2021) 111530, https://doi.org/10.1016/j.optmat.2021.111530. ISSN 0925-3467.
[23] K. Juškevičius, M. Audronis, A. Subačius, S. Kičas, T. Tolenis, R. Buzelis, et al., Fabrication of Nb2O5/SiO2 mixed oxides by reactive magnetron co-sputtering, Thin Solid Films 589 (2015) 95–104, https://doi.org/10.1016/j.tsf.2015.04.075.
[24] Detlev Ristau, Marco Jupé, Kai Starke, Laser damage thresholds of optical coatings, Thin Solid Films 518 (5) (2009) 1607–1613, https://doi.org/10.1016/j.tsf.2009.07.150.
[25] M. Unger, N. Heidler, T. Peschel, C. Damm, R. Jende, P. Weide, K. Kleinbauer, R. Steinkopf, T. Porwol, S. Müller, M. Rohde, J. Hartung, C. Jäger, S. Shestaeva, R. Schlegel, S. Schwinde, M. Goy, F. Steinlechner, S. Risse, Design and manufacturing of a metallic telescope for ground-based quantum communication, Proc. SPIE 13021, Optical Fabrication and Testing VIII (2024) 1302105, https://doi.org/10.1117/12.3022982, 17 June.
[26] Y. Ma, G. Zhang, S. Cao, Z. Huo, J. Han, S. Ma, Z. Huang, A review of advances in fabrication methods and assistive technologies of micro-structured surfaces, Processes 11 (2023) 1337, https://doi.org/10.3390/pr11051337.
[27] Michael N. Sweeney, Advanced manufacturing technologies for light-weight post-polished snap-together reflective optical system designs, Proc. SPIE 4771 (9 September 2002), https://doi.org/10.1117/12.482154. Optomechanical Design and Engineering 2002.
[28] G. Ghosh, A. Sidpara, P.P. Bandyopadhyay, Review of several precision finishing processes for optics manufacturing, Journal of Micromanufacturing 1 (2) (2018) 170–188, https://doi.org/10.1177/2516598418777315.
[29] David D. Walker, David Brooks, Andrew King, Richard Freeman, Roger Morton, Gerry McCavana, Sug-Whan Kim, The 'precessions' tooling for polishing and figuring flat, spherical and aspheric surfaces, Opt. Express 11 (2003) 958–964, https://doi.org/10.1364/OE.11.000958.
[30] J.B. Heaney, L.R. Kauder, S.C. Freese, M.A. Quijada, Preferred mirror coatings for UV, visible, and IR space optical instruments, Earth Observing Systems 8510 (2012) 167–177, https://doi.org/10.1117/12.931005. XVII.
[31] D. A. Sheikh, S. J. Connell, R. S. Dummer "Durable Silver Coating for Kepler Space Telescope Primary Mirror". Surface Optics Corporation, 11555 Rancho Bernardo Road, San Diego, CA, USA, 92127. https://doi.org/10.1117/12.789996.
[32] Paolo Chioetto, Daniele Brienza, Rodolfo Canestrari, Paul Eccleston, Elisa Guerriero, Giuseppe Malaguti, Giuseppina Micela, Emanuele Pace, Enzo Pascale, Raffaele Piazzolla, Giampaolo Preti, Mario Salatti, Giovanna Tinetti, Elisabetta Tommasi, Andrea Tozzi, Paola Zuppella, "Long term durability of protected silver coating for the mirrors of ariel mission telescope," Proc. SPIE 12777, International Conference on Space Optics — ICSO 2022, 127776P (21 July 2023); https://doi.org/10.1117/12.2691351.
[33] Ashley Balzer, Primary mirror for nASA's roman space telescope completed. https://www.nasa.gov/missions/roman-space-telescope/primary-mirror-for-nasas-roman-space-telescope-completed/, 2020. (Accessed 29 April 2025).
[34] Maxime Boccas, Gemini newsletter #29. https://www.gemini.edu/files/docman/websplash/websplash2004-23/GN_silver_coating.pdf, 2004. (Accessed 29 April 2025).
[35] T. Schneider, T. Vucina, C. Ah Hee, C. Araya, C. Moreno, " The Gemini Observatory protected silver coating: ten years in operation ,", in: Ground-Based and Airborne Telescopes VI, vol 9906, 2016 990632, https://doi.org/10.1117/12.2233756.
[36] David A. Sheikh, Improved silver mirror coating for ground and space-based astronomy, Proc. SPIE 9912, Advances in Optical and Mechanical Technologies for

Telescopes and Instrumentation II (22 July 2016) 991239, https://doi.org/10.1117/12.2234380.
[37] https://noirlab.edu/public/news/gemini9801/, 1998. (Accessed 29 April 2025).
[38] https://sci.esa.int/web/euclid/-/57042-euclid-primary-mirror, 2019. (Accessed 29 April 2025).
[39] https://www.amos.be/project/euclid-mirror, 2023. (Accessed 29 April 2025).
[40] Songnian Tan, Yongsen Xu, Yefei Wang, Lei Shi, Optical surface roughness improvement using hot isostatic pressing and coating of additively manufactured mirrors. International Conference on Optoelectronic Information and Functional Materials (OIFM 2024), Proc. SPIE 13183, 5 July 2024, p. 131831W, https://doi.org/10.1117/12.3034060.
[41] Zechen Wang, Maximilian Grimm, Thomas Lindner, Frank Schubert, Kerstin Winkler, Tobias Weise, Thomas Lampke, Enhanced surface finishing of selective laser melted 17-4PH steel by a novel two-step electrolyte plasma polishing process, Mater. Today Commun. 44 (2025) 111934, https://doi.org/10.1016/j.mtcomm.2025.111934. ISSN 2352-4928.
[42] M. Hofele, A. Roth, J. Schanz, D. Harrison, A. De Silva, H. Riegel, Laser polishing of laser powder bed fusion AlSi10Mg parts—influence of initial surface roughness on achievable surface quality, Mater. Sci. Appl. 12 (2021) 15–41, https://doi.org/10.4236/msa.2021.121002.

D. Fano-Resonant Filtering by Chromium-Based Multilayer Stacks

S. Ilchenko, A. Belosludtsev, I. Bitinaitis,
V. Panasyuk, V. Taranenko

Letter Vol. 50, No. 22 / 15 November 2025 / Optics Letters 7019

Optics Letters

Fano-resonant filtering by planar chromium-based multilayer stacks

S. Ilchenko,[1,*] A. Belosludtsev,[2] I. Bitinaitis,[2] V. Panasyuk,[1] and V. Taranenko[1]

[1] Branch of Applied Optics, Institute of Physics, National Academy of Sciences of Ukraine, 10G Kudryavska St, 04053 Kyiv, Ukraine
[2] Optical Coating Laboratory, Department of Laser Technologies, Center for Physical Sciences and Technology, Savanorių ave. 231, Vilnius 02300, Lithuania
*svitlana-ilchenko@ukr.net

Received 20 June 2025; revised 13 August 2025; accepted 26 August 2025; posted 16 October 2025; published 7 November 2025

We demonstrate the design, fabrication, and experimental characterization of planar chromium-based metal–dielectric (Cr-MD) multilayer stacks that support sharp angular and spectral filtering via Fano-type resonances. Two configurations are investigated, differing in the sequence of dielectric layers above a chromium film. Under total internal reflection conditions, hybrid Tamm–waveguide modes yield bright and dark Fano resonances with angular widths of about 0.5 mrad. The high-contrast passband and stopband features are achieved, tunable via Cr thickness. Chromium's unique optical response enables broadband Tamm resonances, providing a compact platform for advanced optical filters. Potential applications include laser spatial mode control, optical sensing, and Raman spectroscopy.

https://doi.org/10.1364/OL.569973

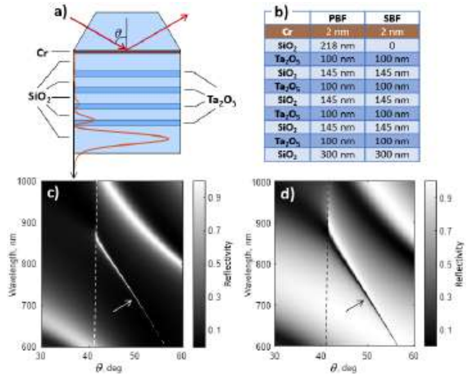

b)	PBF	SBF
Cr	2 nm	2 nm
SiO_2	218 nm	0
Ta_2O_5	100 nm	100 nm
SiO_2	145 nm	145 nm
Ta_2O_5	100 nm	100 nm
SiO_2	145 nm	145 nm
Ta_2O_5	100 nm	100 nm
SiO_2	145 nm	145 nm
Ta_2O_5	100 nm	100 nm
SiO_2	300 nm	300 nm

Fig. 1. Configurable Cr-MD stack. (a) Schematic illustration with overlaid resonant field distribution (red line). (b) Layer composition and thickness for passband (PBF) and stopband (SBF) filtering stack configurations. Reflectivity maps as functions of wavelength and incident angle θ showing (c) bright and (d) dark Fano resonances (highlighted by arrows). The critical angle is indicated by a dashed line.

Introduction. The integration of thin metallic layers with dielectric multilayers enables versatile light manipulation via resonant surface modes. A notable example is the photonic Tamm plasmon structure [1–3], which consists of a distributed Bragg reflector (DBR) topped with a thin metallic layer. This configuration supports Tamm plasmon polaritons (TPPs), which are resonant optical surface states localized at the metal–DBR interface. In contrast to conventional surface plasmon polaritons, TPPs can be excited by both transverse electric (TE) and transverse magnetic (TM) polarized light, and do not require momentum-matching techniques such as prisms or gratings. The Tamm mode appears as a resonance within the photonic bandgap, with properties that can be precisely tailored by engineering the multilayer stack. These features make metal–dielectric Tamm structures highly attractive for applications in optical sensing [4], surface-enhanced Raman spectroscopy [5], and absorption control [6].

Here, we investigate a metal–multilayer–dielectric stack deposited on a prism bottom base (Fig. 1(a)), with the metal layer in direct contact with the prism, followed by a quasiperiodic dielectric stack. This geometry supports narrow Fano-type resonances when the incidence angle exceeds the prism's critical angle [7–9]. In contrast to surface nanostructures [10], which also support Fano resonances but often require complex fabrication, our planar multilayer stack structure offers a simple and fabrication-friendly alternative. Previously, our MD designs based on silver demonstrated very narrow TE-polarized reflection dips (0.2 mrad) using several pairs of high and low-refractive index layers [8]. In this work, we show that replacing silver with chromium enables not only narrow dips (stopband filtering, SBF) but also sharp resonance peaks (passband filtering, PBF) with minimal optical loss, advantageous for applications such as laser mode filtering [11].

The observed resonances result from the interplay between two mode types, both excitable under TE or TM polarization. In this study, we focus on TE-polarized resonances, which exhibit sharper and more pronounced filtering features compared to their TM counterparts. At the metal–dielectric interface,

0146-9592/25/000001-04 Journal © 2025 Optica Publishing Group

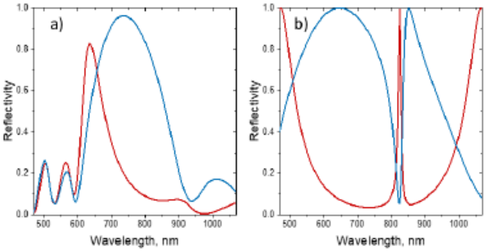

Fig. 2. Spectral reflectivity profiles of PBF sample (red) and SBF sample (blue) under different angles of incidence. (a) Broad resonant contours at 35° (below the critical angle). (b) Sharp spectral features at 45° (above the critical angle), indicative of hybrid Tamm–waveguide mode excitation.

optical Tamm modes are present across a broad angular range [1,2]. In contrast, high-Q leaky waveguide modes, resembling Gires–Tournois cavity resonances [12–14], appear only above the critical angle due to total internal reflection at the dielectric–air boundary.

A key feature of the Cr-MD system is the interference between a narrow waveguide mode and a broad Tamm mode [15], producing asymmetric Fano-type spectral profiles. Above the critical angle, this manifests as bright (Fig. 1(c)) and dark (Fig. 1(d)) resonances in the wavelength–angle reflectivity maps. Depending on the coupling strength and phase conditions, the resulting lineshapes vary from strongly asymmetric to nearly symmetric, forming Lorentzian peaks or inverted dips.

The resonance profiles can be described by the Fano formula [16]: $\sigma(\varepsilon) = (\varepsilon + q)^2 / (1 + \varepsilon^2)$, $\varepsilon = (\theta - \theta_0)/\Gamma$, where q defines the lineshape asymmetry, θ_0 is the resonance angle, and Γ is the half-width. Bright Fano resonances correspond to $|q| \to \infty$, while dark resonances occur at $q = 0$.

Numerics. The optical response of the Cr-MD stack was modeled using the transfer matrix method [17,18], which is well-suited for stratified media with optically homogeneous, isotropic layers, and plane-parallel interfaces. Within this formalism, the total transfer matrix relates the incident, reflected, and transmitted field amplitudes, enabling the calculation of both reflectance spectra and spatial field distributions under a unit-amplitude incident field. This provides direct insight into the resonant field behavior and mode formation. The optical constants (refractive index, n and extinction coefficient, k) of the ultrathin chromium films were taken from [19,20]. The optical constants (n, k) of Ta_2O_5 and SiO_2 were evaluated using OptiChar software [21].

Let us first examine how the reflection spectrum evolves as the angle of incidence crosses the critical angle. Figure 2 shows the simulated reflectance spectra for the PBF and SBF structures (Fig. 1(b)) at the fixed incident angles of 35° and 45°, which lie below and above the critical angle of the prism (41.46°), respectively. At 35°, the spectra are dominated by broad features associated with optical Tamm modes (Fig. 2(a)).

These broad dark bands for the PBF structure and bright bands for the SBF structure are also clearly visible in Figs. 1(c) and 1(d). In contrast, at 45°, sharp spectral resonances, peaks for the PBF structure and dips for the SBF structure, emerge atop the broader Tamm-mode background (Fig. 2(b)). These narrow resonances are indicated by arrows in Figs. 1(c) and 1(d), originate

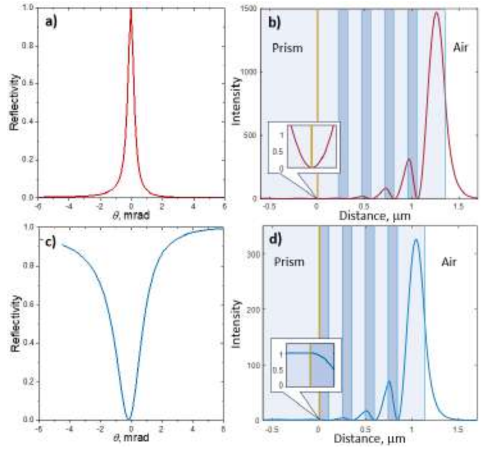

Fig. 3. Angular reflectivity contours at the fixed wavelength λ = 633 nm illustrating bright (a) and dark (c) Fano resonances in Cr-MD stacks, accompanied by the corresponding normalized light field intensity distributions inside the structures (b) and (d). Insets highlight the Cr layer's position at a field node (b, low-loss resonance) or field antinode (d, high-loss resonance).

from the hybridization of leaky waveguide modes with Tamm modes, giving rise to Fano-type resonances. The hybrid modes are localized within the terminal dielectric layer (Fig. 1(a)), similar to pure waveguide modes or Gires–Tournois cavity modes [13]. Notably, in the ideal lossless case, such waveguide modes exhibit unit reflectance with a rapid phase shift near resonance, a behavior mirrored by the hybrid Tamm-waveguide modes in the Cr-MD structure.

Figure 3(a) shows the angular reflectivity profile (R versus θ) for the PBF structure. Despite the multilayer consisting of only 10 layers (Fig. 1(b)), the full width at half maximum (FWHM) of the resonance is less than 0.5 milliradians. The high angular selectivity is due to the resonant field distribution within the structure. At resonance, the ultrathin Cr film coincides with a field node (inset in Fig. 3(b)), minimizing optical absorption and enabling near-total reflectance (Fig. 3(a)). As the incident angle detunes from resonance, the field distribution shifts, placing the Cr layer at an intensity antinode. This leads to a sharp increase in absorption and a rapid drop in reflectance. The transition is accompanied by a smooth π-phase shift in the reflected wave.

In the SBF structure, the field distribution is inverted. At the resonance, the Cr film lies at a field antinode (inset in Fig. 3(d)), resulting in maximum absorption and minimum reflectance (Fig. 3(c)). Upon angular detuning, the Cr layer moves toward a field node, restoring high reflectance. Notably, the dark Fano resonance at the center of the angular contour is characterized by a zero-intensity point and a discontinuous π-phase jump, indicative of a topological phase defect [22].

The results presented in Fig. 3 confirm the formation of bright (passband) and dark (stopband) resonances. They correspond to the Cr–MD stacks with optimized configurations shown in Fig. 1(b). Notably, the presence or absence of a low-refractive-index dielectric layer adjacent to the chromium film leads to an inversion in the symmetry of the resonance contour: a resonance

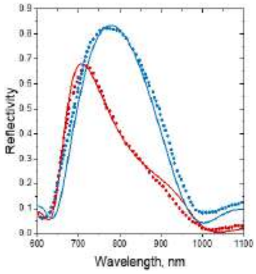

Fig. 4. Simulated (solid lines) and measured (dotted lines) spectral reflectance profiles of Cr-MD stacks: PBF sample with a 3.5 nm Cr layer (red) and SBF sample (blue), measured at an incidence angle below the critical angle.

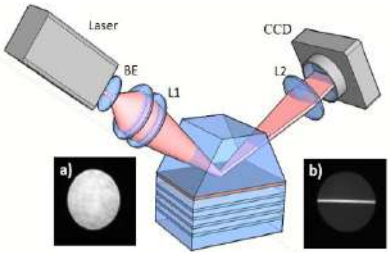

Fig. 5. Schematic of the experimental setup for angular filtering measurements under TE-polarized illumination. Insets show far-field cross-sectional profiles of the incident (a) and reflected (b) beams for the PBF sample.

peak (Fig. 3(a)) transforms into a resonance dip (Fig. 3(c)). Varying the thickness of this dielectric layer introduces asymmetry into the resonance profile, while modifying the thickness of the chromium layer primarily reduces the resonance contrast. These observations highlight the importance of precise control over the thicknesses of both layers, as it is essential for tuning the resonance characteristics and optimizing the spectral and angular filtering performance of the structure.

Experiment. The Cr-MD stacks were fabricated by magnetron sputtering. A detailed description of the chromium film deposition and characterization is provided in [19,20]. The optimization of reactive magnetron sputtering for dielectric layer deposition is discussed in [23]. Dielectric layers (Ta_2O_5 and SiO_2) formed quasiperiodic stacks atop ultrathin Cr films deposited on BK7 prisms (n = 1.515). The layer thicknesses were precisely monitored in real time using a quartz crystal microbalance and a broadband optical monitoring system. These well-established techniques [24], widely adopted in precision multilayer deposition, ensured reproducible control over film thickness and optical properties. Two samples were fabricated and analyzed (Fig. 1(b)): PBF sample, where a low-index SiO_2 layer was placed directly on the Cr film, and SBF sample, where the low-index layer adjacent to Cr was omitted.

Figure 4 shows simulated and measured spectral reflectance profiles for the PBF and SBF samples (Fig. 1(b)). Measurements were performed with a SPECOL 1500 spectrophotometer at a 45° incidence in air, corresponding to an angle below the critical angle inside the prism. The experimental setup and procedure are detailed in [25]. Simulations account for the unpolarized incident beam. Theoretical and experimental spectra agree well, confirming broad optical Tamm resonances characteristic of Cr–MD structures. These broad features underlie the high-contrast passband and stopband filtering observed in the Cr–MD stacks.

Angular filtering was studied using an experimental setup depicted in Fig. 5. A linearly polarized Gaussian beam from a He–Ne laser ($\lambda = 633$ nm, TEM_{00} mode), with horizontal polarization, was expanded using a beam expander (BE) and then focused onto the sample by a lens (L1). By translating L1 along the optical axis, both near-field (within the Rayleigh range) and far-field filtering characteristics of the reflected beam were studied. The far-field angular distribution of the reflected beam was captured using a charge-coupled device (CCD) camera positioned at the focal plane of a second lens (L2).

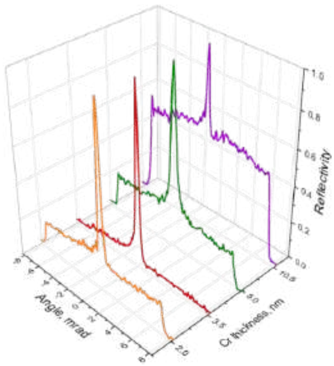

Fig. 6. Experimental angular filtering characteristics of PBF samples as a function of Cr layer thickness.

As discussed above, the resonance contrast in Cr–MD structures is sensitive to the thickness of the chromium layer. To investigate this effect experimentally, a series of PBF and SBF samples were fabricated with Cr thicknesses of about 2.0 nm, 3.5 nm, 5.0 nm, and 10.5 nm.

Figure 6 shows the measured angular reflectivity spectra of PBF samples with different Cr layer thicknesses. The peak reflectance remains nearly constant, but the baseline reflectance changes noticeably with Cr thickness, consistent with the calculated optical field distributions. At resonance, the Cr layer coincides with a field node (inset in Fig. 3(b)), minimizing absorption losses. Detuning shifts the field, increasing absorption that depends on Cr thickness and thus altering the resonance contrast, $C = (R_{max} - R_{min})/R_{max}$. Experimentally, C was 0.83, 0.93, 0.78, and 0.44 for Cr thicknesses of 2.0, 3.5, 5.0, and 10.5 nm, respectively, versus theoretical values of 1.00, 0.94, 0.84, and 0.57. The trends agree well with simulations, with minor deviations due to fabrication and measurement errors. Increasing Cr thickness reduces overall reflectance [19,20]. Thus, by adjusting Cr thickness, one can readily tune the resonance contrast, demonstrating the flexibility of the Cr–MD platform for high-contrast, tunable optical filtering.

Experimental verification of the angular filtering effect predicted by numerical modeling (Figs. 3(a) and (c) is presented

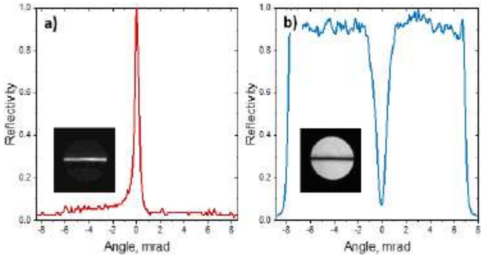

Fig. 7. Angular characteristics of Cr-MD structures: (a) high-contrast passband filtering for the PBF sample with a 3.5 nm Cr layer; (b) stopband filtering for the SBF sample with a 3.5 nm Cr layer. Insets show the corresponding cross-sections of the reflected beams in the far field.

in Figure 7. Consistent with simulations, the measured FWHM of the bright Fano resonance is approximately 0.5 milliradians. Notably, this filtering performance is maintained across both the near field (at the lens focus) and the far field (beyond the Rayleigh range). Figure 7(a) demonstrates the first experimental realization of high-contrast passband filtering in a Cr-MD structure. This behavior arises from the distinctive optical properties of thin Cr films, where a high extinction coefficient facilitates engineered interference between optical modes. The structure achieves exceptional angular selectivity using only 10 layers with a total thickness of 1 µm, several orders of magnitude thinner than the 1 mm typically required in one-dimensional transmission Bragg gratings [26] for similar performance. These results underscore the potential of Cr-based multilayers for integration into compact laser resonators requiring angular mode-selective spatial filtering.

Conclusion. Chromium-based planar metal–multilayer–dielectric stacks support bright and dark Fano-type resonances via Tamm–waveguide mode hybridization. Angular widths of about 0.5 mrad and high contrast are demonstrated using only ten layers. Tuning Cr thickness and dielectric sequences allows control over resonance shape and position. By carefully engineering the structural parameters, Cr–MD stacks can achieve near-ideal high-contrast passband and stopband filtering responses.

This ability to tailor resonant characteristics underscores the promise of Cr–MD stacks for a range of photonic applications, including laser spatial mode filtering, microlaser brightness enhancement, high-resolution optical sensing, and spectral filtering in Raman spectroscopy.

Acknowledgment. We gratefully acknowledge R.A. Lymarenko for valuable discussions and insightful suggestions that contributed to this work. A.B. and I.B. have received funding from the Research Council of Lithuania (LMLTT), agreement No [S-LU-24-3].

Disclosures. The authors declare no conflicts of interest.

Data availability. The data that support the findings of this study, including experimental and numerical results, are available within the article.

REFERENCES

1. M. Kaliteevski, I. Iorsh, S. Brand, *et al.*, Phys. Rev. B **76**, 165415 (2007).
2. M. E. Sasin, R. P. Seisyan, M. A. Kaliteevski, *et al.*, Appl. Phys. Lett. **92**, 251112 (2008).
3. C. Kar, S. Jena, D. V. Udupa, *et al.*, Opt. Laser Technol. **159**, 108928 (2023).
4. O. Buchnev, A. Belosludtsev, and V. A. Fedotov, Opt. Lett. **47**, 4036 (2022).
5. X. Qian, X.-H. Peng, D. O. Ansari, *et al.*, Nat. Biotechnol. **26**, 83 (2008).
6. Y. Gong, X. Liu, H. Lu, *et al.*, Optics Express **19**, 18393 (2011).
7. S. G. Ilchenko, R. A. Lymarenko, and V. B. Taranenko, Nanoscale Res. Lett. **11**, 42 (2016).
8. S. G. Ilchenko, R. A. Lymarenko, and V. B. Taranenko, Nanoscale Res. Lett. **12**, 295 (2017).
9. S. Hayashi, D. V. Nesterenko, A. Rahmouni, *et al.*, Phys. Rev. B **95**, 165402 (2017).
10. B. Luk'yanchuk, N. Zheludev, S. Maier, *et al.*, Nature Mater. **9**, 707 (2010).
11. D. Gailevičius, V. Koliadenko, V. Purlys, *et al.*, Sci. Rep. **6**, 34173 (2016).
12. F. Gires and P. Tournois, C. R. Acad. Sci. Paris **258**, 6112 (1964).
13. B. Golubovic, R. R. Austin, M. K. Steiner-Shepard, *et al.*, Opt. Lett. **25**, 275 (2000).
14. R. C. Nesnidal and T. G. Walker, Appl. Opt. **35**, 2226 (1996).
15. A. M. Vyunishev, R. G. Bikbaev, S. E. Svyakhovskiy, *et al.*, J. Opt. Soc. Am. B **36**, 2299 (2019).
16. M. F. Limonov, M. V. Rybin, A. N. Poddubny, *et al.*, Nat. Photonics **11**, 543 (2017).
17. A. J. Yuffa and J. A. Scales, J. Comput. Phys. **231**, 4823 (2012).
18. T. G. Mackay and A. Lakhtakia, *The Transfer-Matrix Method in Electromagnetics and Optics* (Morgan Claypool, 2020).
19. A. Sytchkova, A. Belosludtsev, L. Volosevicien, *et al.*, Opt. Mater. **121**, 111530 (2021).
20. A. Belosludtsev, A. Sytchkova, K. Baltrusaitis, *et al.*, Coatings **13**, 347 (2023).
21. OptiLayer, About OptiLayer, OptiLayer GmbH, 2025, https://www.optilayer.com
22. S. V. Boriskina and Y. Tsurimaki, J. Phys.: Condens. Matter. **30**, 224003 (2018).
23. A. Belosludtsev, K. Juškevičius, L. Ceizaris, *et al.*, Appl. Surf. Sci. **427**, 312 (2018).
24. A. Tikhonravov, M. Trubetskov, and T. Amotchkina, in *Optical Thin Film Coatings*, A. Macleod, ed. (Woodhead, 2013), p. 62.
25. S. Ilchenko and V. Taranenko, Semicond. Phys., Quantum Electron. Optoelectron. **27**, 090 (2024).
26. B. M. Anderson, E. Hale, G. Venus, *et al.*, Proc. SPIE **9726**, 97261W (2016).

E. The method of Total Internal Reflection Ellipsometry for Multilayer Plasmon Waveguide Resonance Sensors

T. Rakickas, I. Bitinaitis, V. Reshetnyak, L. Shmeleva,
E. Voitechovič, A. Belosludtsev

Sensors & Actuators: B. Chemical 452 (2026) 139454

Contents lists available at ScienceDirect

Sensors and Actuators: B. Chemical

journal homepage: www.elsevier.com/locate/snb

Total internal reflection ellipsometry for multilayer plasmon waveguide resonance sensors

Tomas Rakickas [a,*], Ignas Bitinaitis [a], Victor Reshetnyak [b], Edita Voitechovič [a], Alexandr Belosludtsev [a]

[a] Center for Physical Sciences and Technology, Savanoriu ave. 231, Vilnius, LT-02300 Lithuania
[b] Taras Shevchenko National University of Kyiv, Volodymyrska St. 64/13, Kyiv 01601, Ukraine

A R T I C L E I N F O

Keywords:
Optical biosensor
Plasmon waveguide resonance
Surface plasmon resonance
Bulk sensitivity
Surface sensitivity
Kinetic analysis

A B S T R A C T

The importance of biosensors lies in their ability to detect early stages of diseases, facilitate personalized medicine, provide real-time patient monitoring, and aid in drug discovery, leading to better health outcomes and quality of life. Nowadays, surface plasmon resonance (SPR) is a widely used technique that is label-free and can provide the imaging options like common microscopy. In current research, we report on a significant technique improvement. Our novel SPR biosensor – a combination of plasmon waveguide resonance (PWR) and total internal reflection ellipsometry (TIRE) readout, facilitating phase interrogation, is reported. We used specially designed sensor chips with multilayer metal-dielectric coatings that were theoretically simulated and optimized for use with a standard Kretschmann configuration SPR cell and a commercial imaging null-ellipsometer. We introduce detailed research from the sensor chip structure modelling to measurements. We simulate how the sensor layer structure influences the signal response. Further, the optimized multilayer structure was controllably deposited by the magnetron sputtering and the sensor chip was analyzed with the commercial measurement setup. Firstly, the bulk refractive index sensitivity of the obtained sensor was estimated from ellipsometric parameters Δ and Ψ as a function of angle of incidence (AOI) in water and different refractive index glycerol solutions. With the phase interrogation setup, we obtained 8.5×10^{-7}refractive index unit (RIU) bulk sensitivity with PWR, which is comparable to classical SPR sensitivity. Secondly, the surface sensitivity was demonstrated with lipid bilayer formation and estimated to be better than 3.5 pg mm^{-2}.

1. Introduction

Many bioanalytical techniques that exist today, not only detect protein-ligand interactions or nucleic acids hybridization but also characterize molecular movements inside cells or on their membranes. All these achievements helped in fundamental research and practical applications, e.g., for disease diagnosis. The absolute majority of bioanalytical methods rely on optical detection and the application of fluorescence probes for the labeling of desired biomolecules. Despite the widespread use of fluorescence tags in biological research communities, they still have important limitations including photobleaching, quenching, signal interference, limited spatial resolution and dependence on fluorophores' properties [1]. Therefore, many efforts for the improvement of labeling techniques and optical detection methods are implemented and are still under development [2]. Another approach for the bioanalysis is based on the label-free detection, where surface plasmon resonance (SPR) and electrochemical techniques are the most popular. When the electrochemical methods suggest robust analysis and cost-effective setups, they are usually limited by the detection of only electrical changes in biological objects. In contrast, SPR techniques can overcome those limitations and even provide the imaging options like common microscopy (SPR imaging, SPRi) [3,4]. Since the first use of the SPR effect for biosensing [5], it became a powerful label-free tool to study the interactions between the target and biorecognition molecules [6,7].

Plasmon-waveguide resonance (PWR) is one of the possible modifications to SPR technique. Similar to classical SPR, it features a thin metal film (typically silver, Ag), but PWR additionally has a dielectric waveguide layer, typically silicon dioxide (SiO_2). Similar to SPR, it can be used for characterizing the kinetics and affinity of molecular interactions. It is also tracking the mass density increase on the sensor surface. Like classical SPR, when resonance conditions are fulfilled, light

* Corresponding author.
E-mail address: tomas.rakickas@ftmc.lt (T. Rakickas).

https://doi.org/10.1016/j.snb.2026.139454
Received 6 November 2025; Received in revised form 5 January 2026; Accepted 7 January 2026
Available online 8 January 2026

excites coupled plasmon–waveguide modes at the metal–dielectric interface of the PWR sensor. This resonance could be seen as a reflectivity minimum, called dip, in wavelength or angle of incidence (AOI) spectra for *p*-polarized (*p*-pol, also called transverse magnetic, TM mode) light. Due to additional waveguide resonance, PWR has a narrower reflectivity dip. Moreover, PWR has a second reflectivity dip for incident *s*-pol (transverse electric, TE mode) light. This opens the possibility to monitor the structural properties such as anisotropy of adsorbed adlayers[8–10]. However, it is well known that PWR type biosensors have lower sensitivity than conventional SPR type biosensors, when sensitivity is defined purely in terms of a resonance angle or wavelength shift estimates. In this case, PWR sensor sensitivity can be from 2 [11] up to 10 times [12] lower than conventional SPR. But, PWR sensor spectra feature substantially narrower dips, so when resonance angle or wavelength shift is normalized by the dip full width at half maximum (FWHM), the sensitivity of the PWR sensor could be in the same order or even better than SPR [13,14]. Convert et al. noticed the potential of narrow dip and stated that these sensors are better suited for kinetics measurements at fixed wavelength and AOI [13].

In general, both classical SPR and PWR sensors are total internal reflection devices. Their operation is based on tracking the reflectivity change above the total internal reflection angle. For example, in the visible spectral range the total internal reflection for BK7 glass – water interface appears at angles above 61.5°. In the meantime, high spatial resolution for imaging ellipsometry and imaging SPR requires good image quality, which is easier to obtain at a small AOI. For conventional SPR with a thin Ag layer on BK7 glass, water as ambient and 658 nm wavelength, surface plasmon resonance appears close to 68°. Therefore, to maintain sufficiently good image quality with an imaging ellipsometer and work above the total internal reflection angle, it is desirable to have a sensor with resonances at AOI from 62° to 68°. For PWR sensors, both *p*- and *s*-pol light peaks should be within this range. In addition, a narrow resonance dip or peak is advantageous. A possible solution, how to manipulate the position and width of SPR resonance, was proposed by Lin et al. [15]. They introduced the multilayer coatings (distributed Bragg reflector, DBR) over the SPR sensor to tune the FWHM and position of the resonance dip. This design already resembled PWR sensors. The signal recording technique is another potential way to enhance sensor sensitivity and resolution. Most coupled waveguide sensors, including PWR, and especially in imaging setups, track the intensity of reflected light as a readout signal. This requires a very stable device light source. In the case of classical SPR, a possible and advisable solution is to use the phase of light as a sensing parameter. The phase signal noise can be significantly lower than amplitude/intensity noise [16] It is also compatible with the imaging setup. Therefore, phase interrogation is acknowledged to be an efficient method to increase sensitivity [17]. One of the possible methods to record the phase of reflected light is total internal reflection ellipsometry (TIRE) [18,19]. TIRE is a combination of ellipsometry with Kretschmann type SPR. Moreover, Nabok et al. showed that TIRE is about 10 times more sensitive towards the thickness and refractive index changes as compared to conventional external reflection ellipsometry [19]. TIRE setup is simple and straightforward phase detection setup, and it gives relatively simple approach to imaging setup, thus opening the possibility to detect arrays (multiple areas) at the same time [17].

This study presents a novel design and approach for PWR sensors that can improve their detection sensitivity and resolution. We applied the TIRE setup for PWR sensors and demonstrated the superiority of the phase interrogation method. To the best of our knowledge, this is the first time when TIRE readout is applied for plasmon waveguide resonance sensors. In addition, we used multilayer coating as a waveguide layer instead of a traditional single layer. Introduction of multilayer coating made the resonances even narrower and allows us to tune the angle position of both resonances by varying the thickness of the last high and low refractive index layers. We demonstrate how these narrow resonances could be utilized with a phase interrogation setup and higher sensitivity and resolution can be obtained. The proposed multilayer PWR sensors could be particularly useful for the analysis of pure or multi-component lipid layers. This was demonstrated with the adsorption of lipid bilayer, and the potential to evaluate the lipid layer anisotropy was shown with 1,2-dioleoyl-sn-glycero-3-phosphocholine (DOPC) lipids.

2. Materials and methods

2.1. Materials

All reagents and solvents used in this work are commercially available and used as received. Niobium (99.95 % purity), silicon (99.9999 % purity) and silver (99.99 % purity) sputtering targets were purchased from K.J. Lesker. All gases used for deposition process were > 99.999 % pure and purchased from ELME MESSER LIT. For all experiments, ultrapure water (resistivity 18.2 MΩ cm at 25 °C) was used and taken directly from a Synergy 185UV water purification system (Merck KGaA, Germany). Glycerol was obtained from Carl Roth GmbH (Germany). Na_2HPO_4, NaH_2PO_4, Triton X-100, Heptakis(2,6-di-O-methyl)-β-cyclodextrin were obtained from Sigma-Aldrich. The lipid 1,2-dioleoyl-sn-glycero-3-phosphocholine solution in chloroform (DOPC, 25 mg ml^{-1}) was obtained from Avanti Polar Lipids. Ethanol (>99.9 %) was obtained from Honeywell. 0.1 M phosphate buffer (PB, pH 8.0) was prepared by mixing appropriate ratios of Na_2HPO_4 and NaH_2PO_4 in ultrapure water. Vesicle solution was prepared following the published protocol [20] in PB buffer. Following the protocol, two stock solutions were made. For the first one, the required amount of lipid in chloroform was dispensed into a clean glass bottle and dried. Then lipids were suspended in PB buffer at 5 mM concentration, with 20 mM Triton X-100 detergent. The second stock solution contained 10 mM Heptakis(2,6-di-O--methyl)-β-cyclodextrin in PB buffer. Between use, stock solutions were stored in the fridge. Final vesicle solution was prepared right before the experiment. For that, 50 μl of lipid stock solution was dispensed into the vial and 200 μl of cyclodextrin stock solution was added. After 5 min incubation, solution was diluted to final concentration, 50 μM of DOPC (about 39.3 mg ml^{-1}). Glycerol solutions were prepared in ultrapure water, concentration is given in % by weight.

2.2. Theoretical calculations

The modeling of sensor chip properties was performed with two different software packages. AOI spectra calculation was performed with the software, provided together with ellipsometer – Accurion EP4Model (now Park Systems Gmbh, Göttingen). Electric field distribution was calculated in COMSOL Multiphysics software (Electromagnetic Waves, Frequency Domain). Also, it was used to calculate the reflectivity of *s*- and *p*- polarized incident light, ellipsometric parameters, and electric and magnetic fields distribution in the chip. We used Perfectly Matched Layers at the top and bottom of the modelling domain to have a non-reflecting boundary and effectively absorb outgoing waves. To excite the incoming waves, the domain backed port with slip condition was used.

The initial sensor chip simulation and optimization of layer structure before fabrication was performed with EP4Model software, using the optical constants from inbuilt database. It is well known that the optical constants (refractive index, *n*, and extinction coefficient, *k*) of different materials, particularly noble metals such as Ag, can be significantly different due to different fabrication procedures and conditions [21]. Therefore, optical constants of materials in fabricated chip were fitted. For that, the fabricated sensor chip was mounted into SPR cell and AOI spectra in the range from 61.5 to 65.0° was measured. The cell was filled with ultrapure water. Then, optical constants were fitted with EP4Model software, keeping the sensor chip layer thicknesses constant. The model layer structure was kept the same as obtained from initial layer optimization. Afterwards, these optical constants were used for both models and are summarized in Table 1.

2.3. Sensor chip fabrication

The sensor chip preparation and coating deposition experiments were carried out in the ISO6 standard cleanroom. High refractive index (H) niobium oxide (Nb_2O_5), low refractive index (L) silicon oxide (SiO_2) and silver (Ag) layers were deposited using an unbalanced magnetron source (Torus™ sputter gun) with a planar niobium, silicon and silver targets in a PVD225 sputtering system (Kurt J. Lesker). The system was initially pumped down to a base pressure below 3×10^{-7} Torr. Ar flow rate was 20 sccm and pumping speed was adjusted to attain the argon pressure at the same value of 2.2 mTorr. Settings of Ar flow rate and pumping speed were not changed during the process. Prior to every deposition, target was pre-sputtered for 5 min in Ar to remove any possible target surface oxides. Detailed description of reactive magnetron sputtering and characterization of niobium oxide and silicon oxide layers is given in previous work [22]. The deposition of thin Ag layers has also been previously investigated [23]. In the present work, every deposited layer thickness was controlled by in-situ broadband optical monitoring system (Insoptics Sp.z.O.O.). This monitoring strategy is well known and widely applied for precise optical coating depositions. All the coatings were sputtered on optically polished BK7 glasses. Before the sputtering experiment, glasses were ultrasonically cleaned.

2.4. TIRE measurements

The schematic drawing of the TIRE experimental setup is shown in Fig. 1. The measurements were performed with a commercial imaging ellipsometer (Accurion Nanofilm_ep3, now Park Systems Gmbh, Göttingen), equipped with a laser, emitting at a 658 nm wavelength, 10 × objective and a motorized sample stage. This is nulling type ellipsometer with PCSA (polarizer, compensator, sample, analyzer) configuration. The laser light is passed through the polarizer and compensator, to obtain elliptically polarized light. The polarizer and compensator angles are adjusted to such positions, that upon reflection from the sample, light becomes linearly polarized and polarization state is probed with an analyzer. CCD camera is used as a detector. In addition, microscope objective is used in the optical path to project the sample image onto the CCD camera. For SPR and PWR measurements, a

Table 1
Sensor chip layer structure used for theoretical calculations, the distance from the glass surface and optical constants of materials at λ= 658 nm wavelength.

Layer	Thickness, nm	Distance z, μm	Refractive index (n)	Extinction coefficient (k)
BK7 glass	1000.0/ ambient[a]	-1.0	1.5137[b]	0
Ag	45.0	0.0	0.3126[c]	3.8670[c]
SiO_2 (L1)	10.0	0.045	1.4755[c]	0
Nb_2O_5 (H1)	93.0	0.055	2.2820[c]	0
SiO_2 (L2)	150.8	0.148	1.4755[c]	0
Nb_2O_5 (H2)	99.6	0.2988	2.2820[c]	0
SiO_2 (L3)	150.8	0.3984	1.4755[c]	0
Nb_2O_5 (H3)	99.6	0.5492	2.2820[c]	0
SiO_2 (L4)	150.8	0.6488	1.4755[c]	0
Nb_2O_5 (H4)	183.7	0.7996	2.2820[c]	0
SiO_2 (L5)	219.5	0.9833	1.4755[c]	0
H_2O	1000.0/ substrate[a]	1.2028	1.3312	0

[a] value1000.0 nm value was used for COMSOL simulations and semi-infinite definitions of "ambient" and "substrate" for EP4Model simulations,
[b] value, fitted from total internal reflection angle, with water medium,
[c] fitted values, obtained with water and n(BK7)= 1.5137.

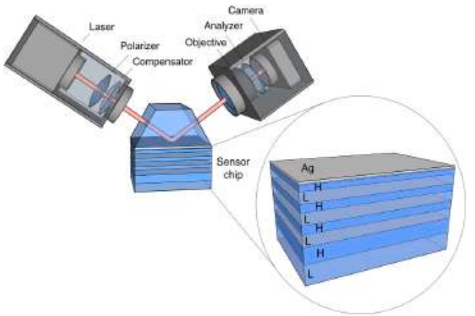

Fig. 1. Schematic of the experimental total internal reflection ellipsometry (TIRE) setup with multilayer PWR biosensor that consists of silver (Ag), niobium pentoxide (H), silicon dioxide (L) layers.

standard Kretschmann configuration Kinetics/SPR cell (now Park Systems Gmbh, Göttingen) with 60° angle BK7 prism was used. Before mounting into the cell, sensor chips were rinsed with ethanol, water and dried with the nitrogen gas stream. Then, they were treated in a plasma cleaner at the 100 W power (Femto, Diener Electronic GmbH, Germany) for 1 min to make them hydrophilic. The optical contact between the prism and sensor chip was made by an index matching liquid (Cargille Laboratories, NJ, USA). The AOI values are given as internal angles – angles of incidence within the prism. Small AOI error, which could appear because of manual prism positioning in the Kinetics/SPR cell, was calibrated with well-known refractive index solution. We assumed that the refractive index of ultrapure water at 22.5 °C temperature is well known (n=1.3312 at λ=658 nm wavelength). According to Snell's law, the total internal reflection angle depends only on the ratio of refractive indices, in our case *n* of the prism and water. Therefore, we measured the position of total internal reflection angle with 0.02° AOI step resolution and calculated the *n* value of the prism. Such angle resolution gives 0.0003 RIU resolution of the prism *n* (with *n* (prism)= 1.5127). For further simulations, *n* of prism was kept constant. In this way, we also compensated the inaccurate AOI within the prism value. This calibration procedure was repeated after each prism movement. The *n* of the prism and sensor chip substrate was assumed to be the same.

The *n* of glycerol solutions with concentration ≥ 0.1 % were measured with the same imaging ellipsometer and sensor chip, mounted into SPR cell, finding the position of total internal reflection angle. First, the SPR cell was filled with ultrapure water, total internal reflection angle was found and the substrate (BK7 glass) *n* value was fitted. Then, glycerol solutions with concentrations from 0.1 % to 10 % were sequentially injected into the cell. Total internal reflection angles were found, and *n* values were fitted for each glycerol solution. The experimental results were fitted with linear function: $n = A{*}c{+}B$, where *c* is solution concentration in % by weight, coefficients *A* and *B* were obtained from linear fit (Fig. S1). At $T = 21.7$ °C they were A= 0.001162, B= 1.33124. This formula was used to calculate *n* of glycerol solutions with concentration < 0.1 %.

Measured data was fitted using QtiPlot Pro software. To determine the resonance positions, Δ plots were fitted using Boltzmann function and Ψ plots were fitted using Sigmoid-Asymmetric function from [24] and min/max was found.

Kinetic measurements were performed at fixed AOI and the evolution of Δ and Ψ parameters over time was recorded. For clearer data representation, the baseline was subtracted from raw data. The baseline drift throughout the experiment (about 5 h) was about 2° in Δ signal and 0.1° in Ψ signal (see raw data in Supplementary material, Fig. S2). The drift mainly appeared due to slight temperature change during the experiment (1°C temperature change corresponds to approximately 0.0001 RIU change of water [25]). Also, slight sensor chip degradation over time (roughly +1 nm per 24 h) was observed. To account for this drift, we repeated water injections after each injection. The flow of water or buffer in the cell was assured with peristaltic pump (Reglo Digital, Ismatec) with flow rate from 9 to 25 μl min^{-1}.

3. Results and discussions

3.1. Theoretical optimization

To optimize the properties of the sensor chip, we employed numerical calculations. We used two modelling software packages, based on different calculation methods. EP4Model software is based on the Fresnel formalism, while COMSOL uses the finite element method (FEM) to solve the frequency domain form of Maxwell's equations.

Initially, the layer structure of multilayer PWR chip was simulated with EP4Model. Optical constants were used from the inbuilt materials database. We were looking for the maximal angular sensitivity to adlayer thickness increase on the sensor surface. In practice, this was realized by maximizing the calculated spectra shift due to addition of 10 nm thickness layer with $n = 1.5$, $k = 0$, thus imitating the adsorption of proteins or lipids to the sensor surface. The starting sensor chip structure was composed of 45 nm Ag, optimal thickness for classical SPR, 10 nm L layer (L1) to protect the Ag from oxidation and 4 pairs of high and low refractive index layers (distributed Bragg reflector, DBR). The used DBR layer structure was similar to Tamm plasmon structure [26–28], with 150 nm thickness L and 100 nm thickness H layers. Such structure had photonic bandgap at around 70° AOI and 658 nm wavelength. Then, the thicknesses of last H and L layers (H4 and L5) were modified to obtain both *p*- and *s*-pol resonances above the total internal reflection angle in water (about 61.5° AOI) and bellow 66° AOI. Finally, the thickness of Ag layer was adjusted to obtain low reflection at resonance for both polarizations.

To get the better agreement between the model and experiment, the optical constants of materials were fitted using the experimental data of fabricated sensor chip. Thus, the first iteration of multilayer PWR sensor chip was fabricated and measured with the TIRE setup, described further in the text (see details in Fig. 1). The dependencies of ellipsometric parameters Δ and Ψ on AOI at the λ= 658 nm were obtained (Fig. 2, black dots) and optical constants were fitted. As the sensor chip is composed of Ag and multiple repeating H and L layers, we kept the layer thicknesses fixed and fitted the optical constants (n and k) of Ag, H and L materials. The layer thicknesses were taken from the initial layer structure calculations. Noteworthy, it was assumed that $k = 0$ for H and L materials. The obtained calculated spectra are shown in Fig. 2, blue curves. The curves showed two resonances, for *p*-pol light at 62.91° AOI and *s*-pol at 64.27° AOI. The positions of resonances were fitted well, but the measured Δ curve has slightly higher values. It is likely because our model is still a simplification and does not account for all factors, like surface roughness, scattering, etc. The sensor chip layer structure, used for modelling, materials, their thicknesses and fitted optical constants are given in Table 1. The obtained fitted values of n and k were reasonably close to database values and calculated Δ and Ψ spectra agreed well with the experimental data, so our ellipsometric model (layer structure with refractive indices) is reasonable and suitable. The obtained model and optical constants were used for further simulations.

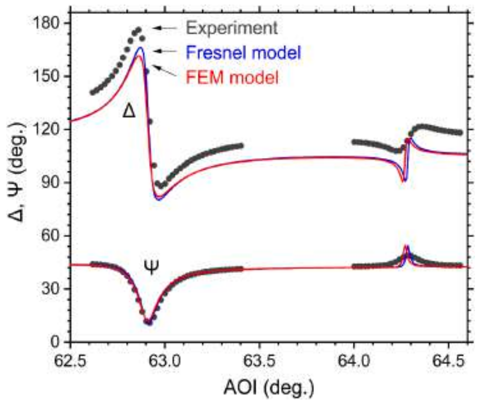

Fig. 2. Ellipsometric parameters Δ and Ψ of the multilayer PWR sensor chip as a function of angle of incidence (AOI) in water. Black dotted line – experimentally measured spectra, blue lines – Fresnel equations-based EP4Model, red lines – COMSOL FEM-based model, λ= 658 nm.

The EP4Model software is dedicated to ellipsometry data modelling and has limited capabilities. To check the correctness of EP4Model results and to obtain a deeper understanding of the operation of the PWR sensor chip, we utilized COMSOL software. To verify the calculated results between two models, the dependencies of Δ and Ψ on AOI were simulated (Fig. 2, red curves) with COMSOL software using the same layer structure and obtained optical constants that are given in Table 1. As it is shown in Fig. 2, the agreement between the two models and the experimental data was very good. There is only a very slight shift of the *s*-pol resonance that can be noticed. Nevertheless, the small difference between the two models is smaller than between models and measurements. Notably, the width of experimentally measured *s*-pol resonance is much wider than theoretically simulated. The reason for experimental resonance widening is likely due to certain imperfections of the real sensor chip, finite laser beam divergence and wavelength. Models considered only perfect laser beam and did not consider finite surface roughness, slight layer thickness or density irregularities on the real sensor chip.

There is an optimal Ag layer thickness when the highest efficiency plasmonic resonance is achieved. At such conditions, the reflectance should approach 0. However, a multilayer PWR sensor has two resonances for different polarizations and the optimal Ag layer thickness for each resonance is different. Therefore, to find the optimal Ag layer thickness for both resonances, we simulated the reflectance dependence on Ag thickness and AOI for *p*- and *s*-pol with EP4Model software (Fig. 3). The *p*-pol has a sharp peak between 62.8° – 63.0° AOI, and *s*-pol has a sharp peak between 64.2° – 64.4° AOI. From the obtained plots, it is well seen that both *p*- and *s*-pol resonances are very narrow with respect to AOI. Also, both resonance angle positions are almost constant when the Ag layer thickness changes. This was observed before for conventional PWR sensors with single waveguide layer [14]. However, the minimal value of reflectance highly depends on the Ag layer thickness. The *p*-pol resonance shows behavior similar to conventional SPR and has a minimum at 40 nm. The *s*-pol reflectance also has a minimum, but at 22 nm thickness of Ag. Still, with 35 nm Ag layer, *s*-pol reflectance is sufficiently low. In addition, when the Ag layer thickness is slightly lower than plasmon resonance, the Δ curve obtains an optimal shape for kinetics measurements at fixed AOI (will be discussed later). Therefore, 35 nm Ag layer thickness is optimal for our multilayer PWR sensor chip.

The performance of evanescent field-type biosensors, including plasmonic and PWR, is largely affected by the electric field distribution at the interface with the sensing medium [6]. Enhancing the evanescent field at the interface is a direct way to improve the performance of the biosensor [29–31]. We used COMSOL software to simulate the electric field distribution of the proposed multilayer PWR at resonance positions, 62.910 ° AOI for *p*-pol and 64.271 ° AOI for *s*-pol at λ= 658 nm. The obtained electric field distribution maps are depicted in Fig. 4. They are similar to electric field distribution of standard PWR sensors [8,11, 12,21]. The electric field concentrates at the interface between the last waveguide layer, layer L5 (Table 1, distance from 0.98 to 1.20 μm), and

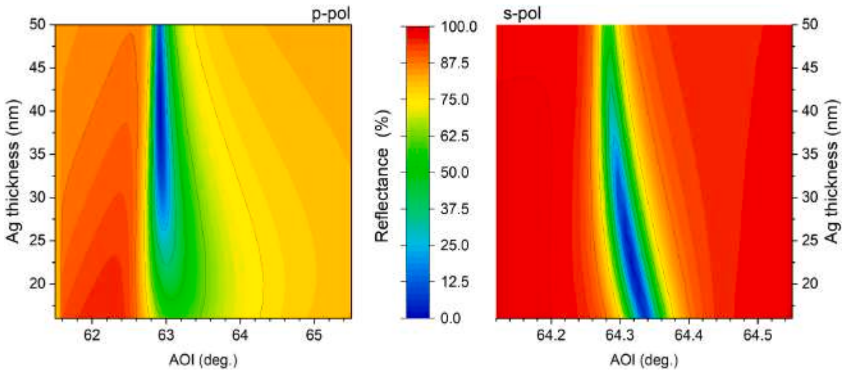

Fig. 3. Reflectance (*s*- and *p*- polarizations) contour plot as the function of the Ag film thickness and angle of incidence (AOI), λ= 658 nm.

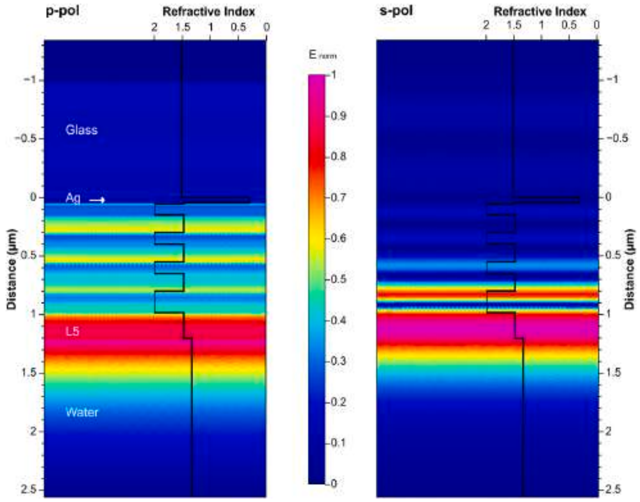

Fig. 4. Normalized electric field distribution profiles of multilayer PWR sensor for *p*-pol (left) and *s*-pol (right) as a function of distance along the *z* axis (normal to the layer plane) from the glass/Ag interface ($z = 0$ nm). Angle of incidence (AOI) for *p*-pol is 62.910 °, for *s*-pol - 64.271 °, λ= 658 nm. Black solid line shows the refractive index profile.

water. It is close to its maximum value at the border. Going further away from the interface, the electric field diminishes. However, a substantial amount of electric field is located in the water layer, close to the border with L5, and this indicates that this multilayer PWR sensor chip should perform well as a biosensor, like ordinary PWR sensor.

3.2. *TIRE measurements and bulk refractive index sensing*

3.2.1. *Variable angle*

The TIRE measurement setup is sketched in Fig. 1. The measurables of ellipsometry are so-called ellipsometric parameters Δ and Ψ, which represent phase change and amplitude change upon reflection between *p*- and *s*- components of polarized light, respectively [18,19,32]. These parameters are extremely sensitive to changes in optical constants of the reflecting surface, its substrate, and ambient. Besides, they also vary with changing incident light wavelength and AOI. To gather more information, usually a variation of Δ and Ψ parameters on wavelength or AOI is recorded. However, our ellipsometer has only fixed wavelength (λ=658 nm), therefore, we will focus only on AOI spectra of Δ and Ψ.

The batch of multilayer PWR sensor chips with a thinner, 35 nm, Ag layer was fabricated. The remaining H and L layers structure was maintained the same as in Table 1. First, the surface morphology of the biosensor was analyzed with AFM (Fig. S3). The sensor surface was smooth and uniform, no sharp features were observed. The calculated root mean square (RMS) surface roughness was very similar to initial BK7 substrate roughness, about 0.5 nm. Then, the AOI spectra of Δ and Ψ of the fabricated multilayer PWR sensor were measured in the SPR cell filled with water (Fig. 5a and b, blue symbols). The corresponding resonances are slightly shifted to higher AOI from the previously simulated and measured values. It might be caused by small differences in the thicknesses of the dielectric layers, which appeared during coating deposition. As was mentioned before, parameter Ψ is proportional to the

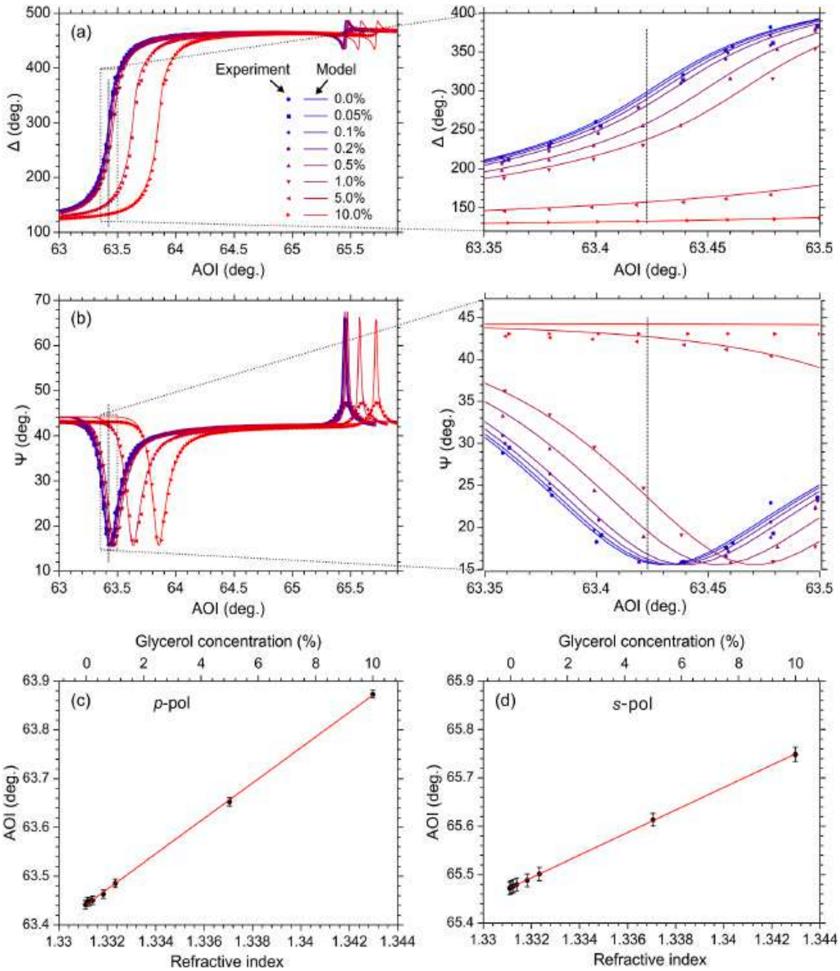

Fig. 5. Multilayer PWR sensor chip bulk refractive index sensitivity measurement in TIRE setup. Experimentally measured a) Δ and b) Ψ vs angle of incidence (AOI) spectra of multilayer PWR sensor chip with water (blue) and increasing glycerol concentrations, as indicated in the legend. Symbols – experimental points, lines – EP4Model fit. Zoom-in of the *p*-pol resonance area is shown on the right. Vertical dashed line indicates AOI position for kinetics measurements. c) and d) Bulk refractive index sensitivity calculation of multilayer PWR sensor. Error bars indicate the standard deviation between measurement values on 6 regions of interest on the same sensor chip. λ= 658 nm, T = 25 °C.

intensity change upon reflection. Therefore, its curve resembles a traditional SPR curve, especially for *p*-pol. The obtained Ψ curve has a dip at 63.423° AOI (Fig. 5b, right plots). The second, *s*-pol, resonance can be seen at 65.456° AOI, where the Ψ curve shows a peak instead of a dip. This is because at the resonance, *s*-pol light has a minimum and $\tan\Psi = |R_p|/|R_s|$, where R_p and R_s are complex Fresnel reflection amplitudes of *p*- and *s*-pol light, respectively [19,32]. The fabricated multilayer PWR sensor chips show very sharp resonances. The FWHM of measured Ψ AOI spectra resonances are 0.172° for *p*-pol and 0.151° for *s*-pol. For comparison, the FWHM of classical SPR spectra with a 50 nm Ag layer, deposited on BK7 glass, measured using the same device and the same conditions, is 0.766° (see supplementary material, Fig. S4). We also simulated the AOI spectra of a classical PWR sensor with single 460 nm thick SiO_2 waveguide layer (Fig. S5). So, the width of the *p*-pol resonance of the multilayer PWR sensor is approximately 4.4 times narrower than the resonance of classical SPR and slightly more than 2 times narrower than PWR sensor with single layer waveguide. Notably, the width of theoretically simulated resonances is even narrower (Fig. 5b, solid lines), especially for the *s*-pol. The FWHM of *s*-pol peak in the simulated spectra is only 0.03°. As was noted before, small inhomogeneities in the coatings, like surface roughness, uneven layer thickness, finite laser beam divergence and wavelength may be the reason for the widening of experimental spectra.

The Δ plot has a completely different shape. At resonance, it has a sharp increase. The narrower and deeper the resonance dip is, the steeper the Δ increase is, with the maximum derivative value at the center of resonance. Therefore, at optimal resonance conditions, Δ variation can be maximized. In such a case, the Ψ minimum should approach 0°. In our case, the fabricated multilayer PWR sensor chip has a slightly thinner Ag layer than required for optimal resonance at *p*-pol. Nevertheless, with a slightly thinner Ag layer, we obtain a monotonic Δ increase with AOI. When the Ag layer thickness is higher than optimal, the Δ curve changes shape and has a sudden drop at a resonance (see Fig. 2). The Δ curve with a monotonic increase is more suitable for kinetic measurements. Namely, when the refractive index of the bulk medium (bulk *n*) increases, resonance and curves shift towards higher angle values. Thus, staying at constant AOI, typical situation for kinetics measurements, measured Δ value smoothly decreases with increasing bulk *n*. In other words, looking at the Δ values along the fixed AOI (vertical dashed line in Fig. 5a) with different concentration glycerol solutions, one could see the monotonic Δ value decrease. The measured *s*-pol resonance is rather shallow, substantially lower than in the simulated spectra. In our opinion, there are two reasons for that. Firstly, the Ag layer thickness was not optimal for this resonance and quality of the resonance was lower. Secondly, the peak may be very narrow, as theoretically simulated peak was substantially narrower than the measured one. But, because of fabrication inaccuracies and limited resolution of the measurement system, the *s*-pol peak widened at the expense of peak sharpness. Nevertheless, ellipsometer has sufficient sensitivity to measure this second *s*-pol resonance accurately.

To evaluate the sensitivity of the multilayer PWR sensor and to compare it with other plasmonic sensors, we measured the response to a bulk *n* value change. For demonstration purposes, we chose a common approach – glycerol solutions in water (Fig. 5). The increase in concentration from 0.0 % to 10.0 % gave a 0.01184 refractive index unit (RIU) change at λ= 658 nm wavelength and 25 °C temperature. The sensitivity of plasmonic sensors is usually reported as an angular or spectral shift of resonance position per RIU. These are amplitude-sensitive parameters [17]. We first demonstrate traditional amplitude-related sensitivity, and we used Ψ curves to calculate it. The response of the multilayer PWR sensor to a 0.01184 RIU bulk *n* value increase was 0.434° and 0.274° for *p*- and *s*-pol, respectively. Measured *p*- and *s*-pol resonance positions were plotted against different refractive index solutions (Fig. 5c and d) to determine the angular sensitivities. The evolutions of both resonance positions fitted well using a linear dependence. The slope of the obtained fit curves gave angular sensitivities, which were $36.3 \pm 0.3° \ \text{RIU}^{-1}$ for *p*-pol and $23.3 \pm 0.1° \ \text{RIU}^{-1}$ for *s*-pol. For comparison, the sensitivity of classical SPR with an Ag layer, measured with the same device, was $130.5° \ \text{RIU}^{-1}$ (supplementary material, Fig. S4). Therefore, if we make a straightforward comparison between the angular sensitivity of multilayer PWR and classical SPR sensors, then the classical SPR sensor outperforms the multilayer PWR sensor. But if we take into account the width of plasmon resonance peaks and normalize the sensitivity to FWHM, then the normalized bulk sensitivity of the multilayer PWR sensor is $211.0 \ \text{RIU}^{-1}$ for *p*-pol and $154.3 \ \text{RIU}^{-1}$ for *s*-pol, while for classical SPR it is $170.4 \ \text{RIU}^{-1}$. The PWR sensor's sensitivity is comparable and even slightly better for *p*-pol resonance than classical SPR, already when comparing the usual amplitude-related parameters.

The smallest, 0.05 % glycerol concentration change in Fig. 5b, which corresponds to 6×10^{-5} refractive index increase, induced a merely visible resonance shift. The *p*-pol resonance was shifted by 0.0058° AOI and the *s*-pol resonance by 0.0019° AOI only. Considering that the angular resolution of our device is declared to be 0.001° AOI, the measured resonance shifts are very close to the limit of device. The resolution of the proposed sensor, if we use this device's angular resolution and divide it by the calculated sensitivity, is 2.75×10^{-5} RIU for *p*-pol. This would be the bulk *n* sensitivity with a very popular angle interrogation setup and 0.001° angular resolution. Such sensitivity of a multilayer PWR is inferior to classical SPR.

3.2.2. Fixed angle, kinetics

Up to now, we have investigated the resonance position shift only and disregarded the peak shape itself. However, multilayer PWR sensors have very sharp resonances. This means that sensor measurables (such as reflectivity, resonance wavelength, etc.) change very rapidly as the sensor approaches the resonance conditions. As mentioned earlier, the resonance peak of the classical SPR is 4.4 times wider. Thus, the rate at which sensor measurements change is significantly reduced. The sensitivity of the multilayer PWR sensor to bulk *n* value change with more sensitive *p*-pol is 3.6 times lower than classical SPR. Therefore, the higher sensor measurables' change rate of multilayer PWR should compensate and slightly outperform the lower angular sensitivity. Earlier calculated bulk sensitivity, normalized to FWHM, also shows this.

To take an advantage of the sharp resonances of multilayer PWR and the resulting rapid sensor measurable change, we can track their evolution at a fixed AOI. The starting AOI should be chosen very close to the resonance angle, where the rate of measurable change is the highest. Furthermore, the use of the TIRE configuration provides the possibility to track the phase change. This is known to be more sensitive than intensity-related parameter change. Indeed, taking a closer look at a zoom-in of *p*-pol part of the curves (Fig. 5a, b), one can notice that at a fixed AOI, that is, going along the vertical dashed line in Fig. 5a, b, the values of parameters Δ and Ψ change with increasing concentration and bulk *n* value. This change is substantially better visible than the resonance angle shift. Even the smallest 0.05 % concentration change can be noticed, especially in the Δ plot (Fig. 5a). This indicates that a multilayer PWR sensor could be very well suited for kinetics measurements at a fixed AOI. To demonstrate this, we recorded parameter Δ and Ψ kinetics – evolution over time at fixed AOI and injected into the cell various concentrations glycerol solutions with known *n* values (Fig. 6).

This time we started with 4 times smaller, 0.0125 % concentration glycerol solution, which corresponds to 1.5×10^{-5} RIU change. This injection was well seen in the kinetics and clearly distinguished from the baseline for both Δ and Ψ parameters (inset in Fig. 6a). Δ signal increased by 1.2° and Ψ by 0.06°. The phase-sensitive parameter Δ gives substantially higher signals than the amplitude-sensitive parameter Ψ. But signal amplitude alone does not show the sensor quality. Another important parameter is signal-to-noise ratio (SNR). Already in the inset of Fig. 6a it can be seen that Ψ gives lower SNR than Δ. We measured the sensor noise during the 20 min right before the main measurements, with the same conditions as for further kinetics measurements, with the pump on and water flowing through the flow cell. Noise was calculated as a standard deviation σ_{so} of the sensor output. It was $\sigma_{so\Delta}$= 0.070° and $\sigma_{so\Psi}$= 0.012° for Δ and Ψ signals, respectively. Even though the noise of Ψ signal is lower, the substantially higher Δ signal increment leads to a much better signal-to-noise ratio for the Δ signal, SNR_{Δ}= 17.1 vs SNR_{Ψ}= 5.0. This demonstrates the superiority of the phase-sensitive parameter Δ.

To calculate the sensitivity, the Δ and Ψ signals were plotted versus solution concentration and resulting bulk *n* value increment (Fig. 6d). The Δ signal shows non-linear behavior and sensitivity decreases with increasing glycerol concentration, while the Ψ response is close to linear in the concentration range from 0 % to 1.0 %. To determine the Δ signal's sensitivity, we used the concentration range of 0–0.5 %, which is nearly linear, and fitted it with a linear function. The obtained sensitivity was $S_{RI\Delta}= 82047 \pm 1758° \ \text{RIU}^{-1}$. For Ψ signal, we used the entire range and obtained $S_{RI\Psi}= 9557 \pm 238° \ \text{RIU}^{-1}$ sensitivity. The most important characteristic of the sensor is the smallest amount of analyte that can be detected. In our case, the smallest change in bulk *n* value that can be readily detected by a sensor is called resolution. We used the description of sensor resolution defined by Piliarik et al. [33], where it was defined as the standard deviation of signal noise, translated to the *n* value of the bulk medium, or, simply saying, signal noise divided by sensitivity ($\sigma_{RI}=\sigma_{so}/S_{RI}$). We calculated the resolution of a multilayer PWR sensor working at a fixed AOI from the kinetics data. It was found

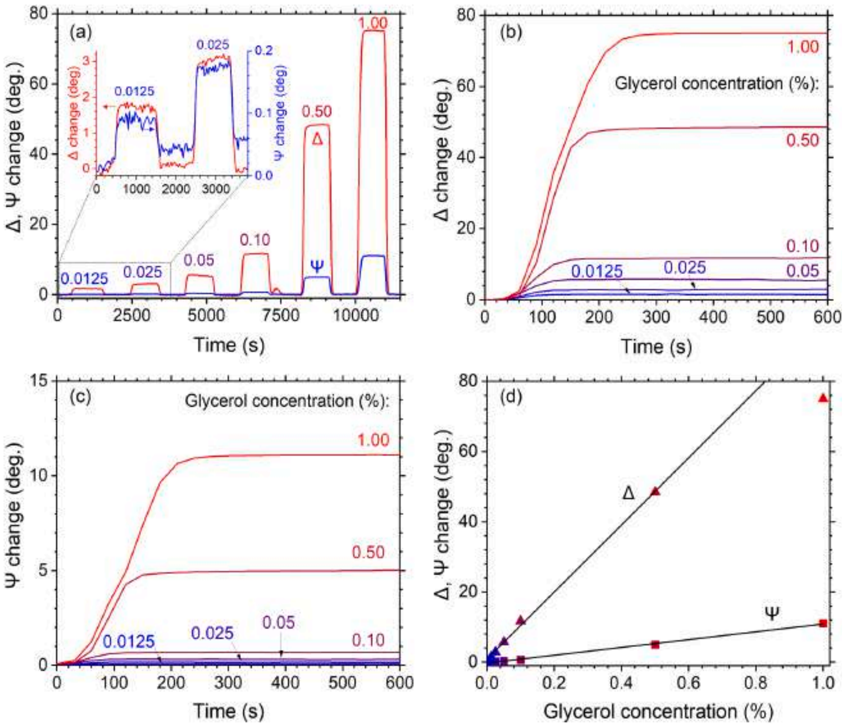

Fig. 6. Kinetics measurements with multilayer PWR sensor. Different glycerol concentration injections were made. a) Δ and Ψ plot with glycerol injection sequence, b) Δ and c) Ψ parameter response to different glycerol concentration solutions. d) Parameters Δ and Ψ change vs glycerol solution concentration with known refractive index, λ= 658 nm, T = 22.5 °C.

to be $\sigma_{RI\Delta}$= 8.5 × 10^{-7} RIU and $\sigma_{RI\Psi}$= 1.3 × 10^{-6} RIU. Accepting the convention of 3σ, that limit of detection (LOD) is 3 times the standard deviation, the LOD of multilayer PWR sensor is $LOD_{RI\Delta}$= 2.5 × 10^{-6} RIU and $LOD_{RI\Psi}$= 3.9 × 10^{-6} RIU for Δ and Ψ signals, respectively.

The bulk refractive index resolution was used to compare the multilayer PWR sensor from this study with those reported previously. Even though the bulk refractive index resolution does not account well for the measurement sensitivity very close to the sensor surface, it is still popular parameter for comparison. The literature review is given in Table 2. As mentioned above, using only the angular interrogation, the resolution was 2.75 × 10^{-5} RIU per 0.001° AOI. Similar, 1.28 × 10^{-5} RIU resolution was obtained with a multilayer SPR sensor on the same model ellipsometer as was used in this study [15]. Comparing the proposed multilayer PWR sensor with previously published PWR sensors, obtained angular sensitivity was similar – 36.3° RIU^{-1} vs 32° RIU^{-1}[11] or 30° RIU^{-1}[34] for *p*-pol, when for *s*-pol it was 23.3° RIU^{-1} vs 10° RIU^{-1} [34]. The resolution of the commercial Biacore 3000 device, which is based on the angle interrogation classical SPR, is reported to be up to 1 × 10^{-7} RIU (Table 2). Higher resolution than classical SPR can be obtained with phase interrogation and interferometric setups (Table 2). In the case of plasmonic waveguide biosensors, only sophisticated phase detection schemes, such as Goos–Hänchen shift and/or hetero-metasurface coatings can provide resolution parameters, comparable with classical SPR (Table 2). The proposed multilayer coating strategy, which offers a simpler approach for practical implementation, resulted in the development of the multilayer PWR sensor with sensitivity suitable for biosensing applications. The multilayer PWR sensor chip, featuring the sharp resonance peak and phase (Δ) interrogation, achieved resolution of $\sigma_{RI\Delta}$ = 8.5 × 10^{-7} RIU. Although, this performance is slightly lower than the top commercial devices, it remains within a comparable range. It is important to note that the Δ signal noise observed in this study's setup ($\sigma_{so\Delta}$=0.070°) was higher than the values previously reported in the literature. Therefore, there is potential for improvements, like obtaining sharper/narrower and deeper resonance peaks and minimizing detection system noise. The proposed multilayer PWR structure would also have two resonances in reflection spectra at fixed AOI. Therefore, this layer structure could be used for Kretschmann setups with wavelength readout and even for optical fiber setups, based on lossy mode resonance readout [35]. Multilayer structure would particularly beneficiary here, as multilayer structure would narrow the resonance spectra and allow tuning the position of both resonances.

3.3. *Surface sensitivity - Lipid bilayer measurements*

The newly developed multilayer PWR sensor chip was evaluated with respect to its biosensing capabilities. Physical properties (discussed above), such as the refractive index of the bulk medium, are not the primary factors in this case. Bioanalytical research commonly examines the density and thickness of biomolecules adsorbed on the sensor surface, as well as the binding reactions involving these molecules. Therefore, the surface sensitivity is another important parameter, which

Table 2
Comparison of multilayer PWR sensor with published results.

Detection technique	Interrogation	Sensor chip composition	Sensitivity *S*	LOD	Resolution σ, RIU	Noise	Ref.	Comments
Classical SPR, with commercial Biacore 3000	Angle	Quartz with 46 nm Au Quartz with 46 nm Au + 10.5 nm SiO_2	Theoretical: Bare Au: 164.57° RIU^{-1} Au + 3.5 nm TiO_2+ 10.5 nm SiO_2: 205.52° RIU^{-1} Experimental: 1.014–1.049 × 10^6 RU RIU^{-1} (≈ 162–168° RIU^{-1})	With PSA assay: 1.5 nM (bare Au) 2.5 nM (SiO_2/Au)	3 × 10^{-7}	0.29–0.39 RU RMS	[36]	1 RU= 0.00016°
Classical SPR, with commercial Biacore 3000	Angle	N/A	N/A	N/A	1 × 10^{-7}		[33]	
Classical SPR, with rotating-mirror, palm-sized	Angle	47 nm Au on BK7	8.4 × 10^{-5} RIU $pixel^{-1}$ S_{RI}= 109.5° RIU^{-1}	2.5 × 10^{-6} RIU	7.5 × 10^{-7}	±0.009 pixel	[37]	1 pixel= 0.0092°
Classical SPR	Angle	BK7, 52 nm Ag, 3–6 nm SiO_2	S_{RI}= 68°×RIU^{-1} S_s= 0.120°×nm^{-1}	N/A	N/A	N/A	[11]	S_s With lipid bilayer
Classical SPR, measured with spectroscopic ellipsometer	Wavelength	Quartz with 45 nm Au	S_{RI}= 3858 nm RIU^{-1}	N/A	1.6 × 10^{-5}	0.064 nm	[38]	Measures Ψ & Δ spectra vs wavelength, although track wavelength shift only
Classical SPR with imaging setup	Intensity	BK7, 4 nm Cr, 43 nm Au	Normalized reflectivity S_{RI}= 4044.62 ± 35.69 % RIU^{-1}	LOD_{RI}= 9.2 × 10^{-6} RIU	3.07 ± 0.97 × 10^{-6}	0.01 %	[39]	
Classical SPR with digital micro-mirror device scanning	Angle	BK7, 50 nm Au	S_{RI}= 735° RIU^{-1}	9 ng ml^{-1} with BSA/anti-BSA	3.54 × 10^{-6}	0.0026°	[40]	Sensitivity at the most sensitive region, 0–0.0625 % glycerol concentration
Classical SPR with Mach-Zehnder interferometer configuration	Phase	BK7, 47 nm Ag, 5 nm Au	21.88° per 0.00012 RIU, S_{RI}= 182333° RIU^{-1}	LOD = 7.4 ng ml^{-1} with anti-BSA	5.5 × 10^{-8}	0.01°	[41]	Sensitivity at the most sensitive region
Classical SPR sensor with laser feedback interferometry setup	Phase	BK7, 40 nm Au	S_{RI}= 1.33 × $10^{5\circ}$ RIU^{-1}	N/A	1.0 × 10^{-7}	0.013°	[42]	Sensitivity at the most sensitive region, 0–0.05 % glycerol
Classical SPR with combined phase and angular interrogation	Phase	BK7, 46 nm Au	S_{RI}= 89766° RIU^{-1} (Calculated 5000°/0.0577 RIU) S_{RI}= 5.6 × $10^{6\circ}$ RIU^{-1} [a]	N/A	2.2 × 10^{-7}	0.02°	[43]	
Classical SPR with phase-shifted polarimetric readout scheme	Phase	SF11, 2 nm Cr, 42 nm Ag, 5 nm Au	Angular sensitivity S_{RI}= 118.7° RIU^{-1}	N/A	1.03 × 10^{-7}	N/A	[44]	
Classical SPR, measured with spectroscopic ellipsometry	Phase	BK7, 42 nm Au	$S_{RI,Δ}$= 5839 ± 229° RIU^{-1}	3 pM with anti-BSA	1.712 × 10^{-7}	0.001°	[45]	
Classical SPR with interferometric, wavelength-multiplexing readout, imaging	Phase	BK7, 47 nm Au	N/A	N/A	2.7 × 10^{-7}	N/A	[46]	
Rectangular nano-plasmonic interferometer	Wavelength	Slit and groove structure in 300 nm Au on glass, distance = 850 nm,	S_{RI}= 4923 nm RIU^{-1}	N/A	2.2 × 10^{-6}	0.011 nm	[47]	
Fiber-optic SPR sensor	Wavelength	Multimode fiber with 550 Å Ag film coating	N/A	N/A	2.5 × 10^{-4} – 7.5 × 10^{-5}	N/A	[48]	First demonstration of fiber-optic SPR
Optical-fiber-nanowire microcoil resonator	Wavelength	300 nm fiber coil in teflon	700 nm RIU^{-1}	N/A	10^{-7}	N/A	[49]	Theoretical estimation
Long-range SPR	Wavelength	360 nm MgF_2 on 40 nm Au 700 nm Teflon on 24 nm Au	S_{RI}= 5.0 × 10^3 nm RIU^{-1} S_{RI}= 3.0 × 10^4 nm RIU^{-1}	N/A	2.4 × 10^{-7} 2.5 × 10^{-6}	1.2 × 10^{-3} nm 7.4 × 10^{-2} nm	[50]	

(continued on next page)

Table 2 (*continued*)

Detection technique	Interrogation	Sensor chip composition	Sensitivity S	LOD	Resolution σ, RIU	Noise	Ref.	Comments
Ellipsometric sensor based on the Bloch surface wave	Phase	1D photonic crystal on BK7	Angular sensitivity S_{RI}= 49.47° RIU^{-1}	1.6 × 10^{-5} RIU	1 × 10^{-5}	N/A	[51]	For 622.7 nm wavelength.
Coupled waveguide–surface plasmon resonance biosensor with subwavelength grating	Wavelength	Pyrex with grating, 285 nm Ta_2O_5, 40 nm Au	N/A	N/A	1 × 10^{-6}	0.01 nm	[52]	Normal incidence via objective
Ag-PWR	Angle	BK7, 52 nm Ag, 510 nm SiO_2	S_{RI}= 32° RIU^{-1} (0.32° per 0.01 RIU) S_s= 0.018° nm^{-1}	N/A	N/A	N/A	[11]	S_s With lipid bilayer
Waveguide coupled surface plasmon resonance imaging	Intensity	BK7, 4 nm Cr, 24 nm Au, 900 nm PC, 24 nm Au	Normalized reflectivity S_{RI}= 5960.34 ± 58.42 % RIU^{-1}	5.9 × 10^{-6} RIU	1.90 ± 0.28 10^{-6}	0.01 %	[39]	PC - polycarbonate
PWR	Angle	SF11, 50 nm Ag, 450 nm SiO_2	S_{RI}(*p*-pol)= 30° RIU^{-1} S_{RI}(*s*-pol)= 10° RIU^{-1}	N/A	N/A	N/A	[34]	
PWR PWR + Ag nanoparticles	Wavelength	BK7, 45 nm Ag, 600 nm SiO_2 BK7, 45 nm Ag, 600 nm SiO_2, 50 nm SiO_2:Ag	S_{RI}(PWR)= 368.5 nm RIU^{-1} S_{RI}(Ag np+PWR)= 1396.85 nm RIU^{-1}	N/A	N/A	N/A	[53]	
PWR, imaging setup	Intensity	BK7, 3 nm Ni, 23 nm Ag, 5 nm Au, 220 nm KMPR core	S_{RI}(PWR)= 96 RIU^{-1} Normalized intensity/RIU	N/A	N/A	N/A	[21]	Called in paper "Metal clad waveguide (MCWG)" For cell imaging
Symmetric metal cladding plasmonic waveguide (SMCW)	Phase, via Goos–Hänchen (GH) shift	Silica, 35 nm Au, 1.1 mm gap, 110 nm Au	2.33 × 10^4 µm RIU^{-1}	N/A	1 × 10^{-8}	N/A	[54]	
Nanomaterial (hetero-metasurface)-Enhanced classical SPR sensor	Phase, via GH shift	SF11, Au, 2 nm 2D $Ge_2Sb_2Te_5$ (GST)	5.95 × 10^4 µm RIU^{-1}	LOD(TNF-α cancer marker)= 10^{-15}M LOD(biotin)= 10^{-14}M	N/A	N/A	[55]	
Classical SPR with Goos-Hänchen shift detection	Phase, via GH shift	BK7, 42 nm Au	1.82 × 10^{-8} RIU nm^{-1} 5.5 × 10^7 nm RIU^{-1}	N/A	4 × 10^{-7}	Position resolution 20 nm	[56]	
SPR with multilayer coating	Angle and intensity	BK7, Au/$(SiO_2/TiO_2)_4$/ Au	S_{RI}= 75.617° RIU^{-1}	N/A	1.28 × 10^{-5}	Angle resolution 0.001°	[15]	Measured with EP^3 ellipsometer
Multilayer PWR	Angle	Multilayer PWR	S_{RI}(*p*-pol)= 36.3 ± 0.3°×RIU^{-1} S_{RI}(*s*-pol)= 23.3 ± 0.1°×RIU^{-1}	N/A	2.75 × 10^{-5} for *p*-pol	Angle resolution 0.001°	present work	
TIRE on multilayer PWR	Phase	Multilayer PWR	$S_{RI\Delta}$= 82047 ± 1758° RIU^{-1}, $S_{RI\Psi}$= 9557 ± 238° RIU^{-1}	$LOD_{RI\Delta}$= 2.5 × 10^{-6} RIU $LOD_{RI\Psi}$= 3.9 × 10^{-6} RIU	$\sigma_{RI\Delta}$= 8.5 × 10^{-7} $\sigma_{RI\Psi}$= 1.3 × 10^{-6}	$\sigma_{so\Delta}$= 0.070°, $\sigma_{so\Psi}$= 0.012°	present work	

N/A = not available in the cited article, S_{RI} – bulk refractive index sensitivity, S_s – surface sensitivity, [a] Sensitivity with optimized Au thickness is defined as a sensor signal change per increase of the adlayer thickness. It can differ significantly from the bulk sensitivity. The distribution of electric fields near the optical biosensor surface has a significant impact on this parameter [29]. The convenient formation of lipid bilayer was applied for the evaluation of the surface sensitivity of the multilayer PWR sensor. The lipid bilayer is ideal for this purpose due to its simple formation on a hydrophilic SiO_2 surface through lipid vesicle fusion. Moreover, this layer can be used as a thickness standard. The DOPC lipids that were applied in this study, are known to form a uniform and fluid lipid bilayer, with thickness of 5 nm [57,58]. In the beginning

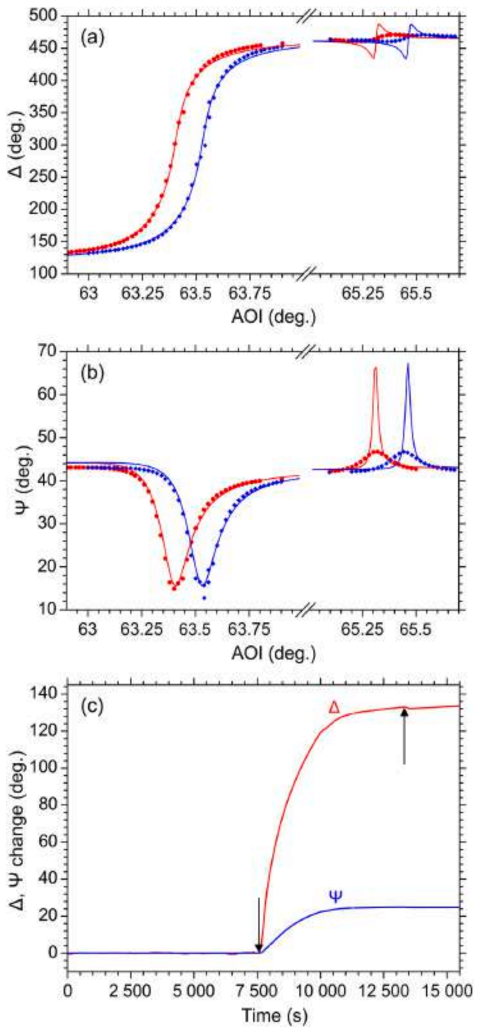

Fig. 7. DOPC lipid bilayer formation on multilayer PWR sensor. a) Angle of incidence (AOI) spectra before lipid injection (red) and after DOPC bilayer formation (blue). b) Kinetics of DOPC vesicle formation. The injection beginning and end are marked with arrows. Running buffer – PB, λ= 658 nm, T = 21.6 °C. Kinetics AOI= 63.378°.

clean multilayer PWR AOI spectra in PB buffer without lipids were recorded (Fig. 7a and b). As the thickness of the lipid layer was assumed to be 0 nm (no lipids), the thickness of the last low refractive index layer L5 (Table 1) was fitted and adjusted to obtain a match between experimental and simulated spectra. Then, the kinetics measurements were carried out at the AOI angle slightly (0.02°) below the *p*-pol resonance (Fig. 7c). Before loading DOPC vesicles, a baseline was recorded in the running PB buffer in the fluid cell. Subsequently, DOPC vesicles at a concentration of 39.3 μg ml^{-1}, in PB buffer with Triton X100 and cyclodextrin, were injected. After 98 min, the vesicle adsorption approached saturation. At this point the vesicle injection was discontinued and only PB buffer was loaded again. In the end of the experiment, another AOI spectra in PB buffer was recorded to find multilayer PWR sensor resonances with the adsorbed lipid layer (blue symbols in Fig. 7a and b). The adsorption of the lipids substantially shifted both *p*- and *s*-pol resonances. Analyzing the experimental spectra, the obtained resonance shift was 0.125° for *p*-pol and 0.131° for *s*-pol. The adlayer thickness was the same because both polarization resonances were measured at the same position on the sample. The observed surface sensitivity of the multilayer PWR sensor is slightly higher for *s*-pol than for *p*-pol. The swap between more sensitive polarization for bulk *n* value and adlayer sensing can be explained by different electric field distribution for *p*- and *s*-pol resonances. This can be seen in the theoretical electric field distribution calculations (Fig. 4), where the electric field in the water medium diminishes faster for *s*-pol than for *p*-pol. Alongside the evaluation of the theoretical model with experimentally obtained spectra, the same fitting can give the information about the thickness of the adsorbed lipid layer. In this study, for the sake of simplicity, we used a single, isotropic *n* value of lipid layer and assumed it to be $n = 1.50$ [59–61]. Initially, for the lipid layer thickness fitting, we concentrated only on the *p*-pol resonance and disregarded the *s*-pol. The best fit was obtained with a lipid layer thickness of 5.88 nm (blue curves in Fig. 7a and b). This thickness was slightly higher than expected 5 nm, but from the camera image, it was seen that the lipid layer was not uniform and some unruptured vesicles were still bound to the lipid layer on the surface, thus increasing the average layer thickness. The shift of *p*-pol resonance in the calculated spectra was 0.126°, almost the same as in the experimental spectra, so the agreement was good. The entire spectra, including and *s*-pol resonance, was calculated with the obtained model and parameters as for *p*-pol. The shift of the calculated *s*-pol resonance was 0.151°, significantly higher than the 0.131° shift in experimental spectra. In other words, in experimental data the *s*-pol resonance shifted slightly less than calculated by the model, if all model parameters are kept the same for both polarizations and adsorbed layer is treated as isotropic. This discrepancy for *s*-pol can be easily explained by anisotropy in the ordered lipid bilayer and slightly lower *n* value for *s*-pol. This was observed with PWR sensors quite some time ago [62]. At the same time, this demonstrates the possibility to detect optical anisotropy in a formed lipid bilayer with a multilayer PWR sensor. The surface sensitivity was calculated from AOI spectra and kinetics data. More common, angle interrogation, surface sensitivity was calculated from Fig. 7b as resonance angle shift per 1 nm of adsorbed layer with $n = 1.5$ and they are S_s(*p*-pol)= 0.021° nm^{-1} and S_s(*s*-pol)= 0.022° nm^{-1}. Similarly, from the kinetics measurement data (Fig. 7c), we could calculate the surface sensitivities as Δ and Ψ signal change per 1 nm of adsorbed layer. Linear Δ and Ψ ranges should be used for such simple estimation. But from the kinetics measurement data (Fig. 7c) we see that the 5.88 nm of adsorbed lipids layer shifted Δ signal by 132° and Ψ signal by 24.7°. Such values were substantially higher than the linear range of sensitivity, especially for Δ (see Fig. 6d). This proves high surface sensitivity of multilayer PWR sensor. The less sensitive but more linear Ψ signal was used to roughly estimate surface sensitivity, giving $S_{s\Psi}$(*p*-pol)= 4.21° nm^{-1}. Surface layer thickness resolution was also calculated: $\sigma_{s\Psi}$= 0.01475°/(24.76°/5.88 nm)= 0.0035 nm. The 0.01475° is a Ψ noise for this particular measurement. Assuming that lipid density is 1.01 g cm^{-3}[63], it could be recalculated to surface density units. Therefore, surface density resolution is 3.5 pg mm^{-2}.

4. Conclusions

In this work, a novel combination of plasmon waveguide resonance (PWR) and total internal reflection ellipsometry (TIRE) readout for sensing was introduced. To increase the resolution of such sensor, multilayer coating as a waveguide layer and phase interrogation with TIRE setup was implemented and tested. The designed alternating metal, high and low refractive index coatings can act as a waveguide and support guided modes. The chip optical response was demonstrated by the theoretical modelling and experimental results. Our sensor with multilayer coating maintained two sharp resonances for *p*- and *s*-pol, additionally allowing a tuning of the resonance positions by changing the thicknesses of last layers. The narrow resonances (FWHM in AOI is 0.172° for *p*-pol) and the use of TIRE setup for multilayer PWR sensor chips enabled rapid phase change exploitation with sensitivity $S_{RI\Delta}$= 82047 ± 1758° RIU^{-1} and achieved high-resolution (up to 8.5 $\times 10^{-7}$ RIU) sensor performance, particularly in kinetics measurements at fixed AOI. This was demonstrated experimentally with different concentration of glycerol water solutions and DOPC lipid bilayers, obtaining the information not only about the thickness of the layer but also its anisotropy. The analysis of biological membranes still remains of high interest, mainly due to their complexity, arising from heterogeneity in structure and composition. Therefore, the more sensitive label-free analysis methods, capable to study mass increase and conformational changes with lateral resolution have a great potential. Especially for the studies of conformation transitions within the lipid membranes, caused by various natural or artificial factors, starting from metal ion concentrations to antimicrobial peptides and artificial pollutants like microplastic. We believe that with improved temperature control and more precise layer deposition methods the proposed multilayer PWR sensor would be helpful in this area.

CRediT authorship contribution statement

Edita Voitechovič: Writing – review & editing, Writing – original draft, Visualization, Funding acquisition, Conceptualization. **Victor Reshetnyak:** Visualization, Software, Methodology. **Ignas Bitinaitis:** Visualization, Validation, Investigation, Formal analysis. **Tomas Rakickas:** Writing – review & editing, Writing – original draft, Visualization, Validation, Supervision, Methodology, Investigation, Formal analysis, Data curation, Conceptualization. **Alexandr Belosludtsev:** Writing – review & editing, Writing – original draft, Visualization, Validation, Supervision, Project administration, Investigation, Funding acquisition, Formal analysis, Conceptualization.

Declaration of Competing Interest

The authors declare the following financial interests/personal relationships which may be considered as potential competing interests: Tomas Rakickas reports financial support was provided by Research Council of Lithuania. Victor Reshetnyak reports financial support was provided by Ministry of Education and Science of Ukraine. Victor Reshetnyak reports financial support was provided by University of Warwick. If there are other authors, they declare that they have no known competing financial interests or personal relationships that could have appeared to influence the work reported in this paper.

Acknowledgments

This project has received funding from the Research Council of Lithuania (LMTLT), agreement No S-LU-24–3. From Ukrainian party the project has received funding from the Ministry of Education and Science of Ukraine (MES), agreement No M/60–2024. V.R. is supported by an IAS Fernandes Fellowship and the University of Warwick (UK). Image of lipid bilayer in graphical abstract was adapted from Guilherme Bauer Negrini, SciDraw (https://scidraw.io/doi.org/10.5281/zenodo.3926481).

Appendix A. Supporting information

Supplementary data associated with this article can be found in the online version at doi:10.1016/j.snb.2026.139454.

Data availability

Data will be made available on request.

References

[1] J. Jonkman, C.M. Brown, G.D. Wright, K.I. Anderson, A.J. North, Tutorial: guidance for quantitative confocal microscopy, Nat. Protoc. 15 (2020) 1585–1611, https://doi.org/10.1038/s41596-020-0313-9.

[2] N. Radmacher, O. Nevskyi, J.I. Gallea, J.C. Thiele, I. Gregor, S.O. Rizzoli, J. Enderlein, Doubling the resolution of fluorescence-lifetime single-molecule localization microscopy with image scanning microscopy, Nat. Photonics 18 (2024) 1059–1066, https://doi.org/10.1038/s41566-024-01481-4.

[3] V. Kodoyianni, Label-free analysis of biomolecular interactions using SPR imaging, Biotechniques 50 (2011) 32–40, https://doi.org/10.2144/000113569.

[4] T. Söllradl, F.A. Banville, U. Fröhlich, M. Canva, P.G. Charette, M. Grandbois, Label-free visualization and quantification of single cell signaling activity using metal-clad waveguide (MCWG)-based microscopy, Biosens. Bioelectron. 100 (2018) 429–436, https://doi.org/10.1016/J.BIOS.2017.09.002.

[5] B. Liedberg, C. Nylander, I. Lunström, Surface plasmon resonance for gas detection and biosensing, Sens. Actuators 4 (1983) 299–304, https://doi.org/10.1016/0250-6874(83)85036-7.

[6] X. Fan, I.M. White, S.I. Shopova, H. Zhu, J.D. Suter, Y. Sun, Sensitive optical biosensors for unlabeled targets: a review, Anal. Chim. Acta 620 (2008) 8–26, https://doi.org/10.1016/J.ACA.2008.05.022.

[7] M. Couture, S.S. Zhao, J.F. Masson, Modern surface plasmon resonance for bioanalytics and biophysics, Phys. Chem. Chem. Phys. 15 (2013) 11190–11216, https://doi.org/10.1039/C3CP50281C.

[8] Z. Salamon, H.A. Macleod, G. Tollin, Coupled plasmon-waveguide resonators: a new spectroscopic tool for probing proteolipid film structure and properties, Biophys. J. 73 (1997) 2791–2797, https://doi.org/10.1016/S0006-3495(97)78308-5.

[9] Z. Salamon, M.F. Brown, G. Tollin, Plasmon resonance spectroscopy: probing molecular interactions within membranes, Trends Biochem Sci. 24 (1999) 213–219, https://doi.org/10.1016/S0968-0004(99)01394-8.

[10] P. Calmet, M. De Maria, E. Harté, D. Lamb, M. Serrano-Vega, A. Jazayeri, N. Tschammer, I.D. Alves, Real time monitoring of membrane GPCR reconstitution by plasmon waveguide resonance: on the role of lipids, Sci. Rep. 6 (2016) 1–12, https://doi.org/10.1038/srep36181.

[11] A. Abbas, M.J. Linman, Q. Cheng, Sensitivity comparison of surface plasmon resonance and plasmon-waveguide resonance biosensors, Sens Actuators B Chem. 156 (2011) 169–175, https://doi.org/10.1016/J.SNB.2011.04.008.

[12] F.C. Chien, S.J. Chen, A sensitivity comparison of optical biosensors based on four different surface plasmon resonance modes, Biosens. Bioelectron. 20 (2004) 633–642, https://doi.org/10.1016/J.BIOS.2004.03.014.

[13] L. Convert, V. Chabot, P.J. Zermatten, R. Hamel, J.P. Cloarec, R. Lecomte, V. Aimez, P.G. Charette, Passivation of KMPR microfluidic channels with bovine serum albumin (BSA) for improved hemocompatibility characterized with metal-clad waveguides, Sens Actuators B Chem. 173 (2012) 447–454, https://doi.org/10.1016/J.SNB.2012.07.061.

[14] N. Skivesen, R. Horvath, H.C. Pedersen, Optimization of metal-clad waveguide sensors, Sens Actuators B Chem. 106 (2005) 668–676, https://doi.org/10.1016/J.SNB.2004.09.014.

[15] C.W. Lin, K.P. Chen, C.N. Hsiao, S. Lin, C.K. Lee, Design and fabrication of an alternating dielectric multi-layer device for surface plasmon resonance sensor, Sens Actuators B Chem. 113 (2006) 169–176, https://doi.org/10.1016/J.SNB.2005.02.044.

[16] A.V. Kabashin, S. Patskovsky, A.N. Grigorenko, Phase and amplitude sensitivities in surface plasmon resonance bio and chemical sensing, , Pp. 21191-21204 17, Opt. Express 17 (23) (2009) 21191–21204, https://doi.org/10.1364/OE.17.021191.

[17] A.V. Kabashin, V.G. Kravets, A.N. Grigorenko, Label-free optical biosensing: going beyond the limits, Chem. Soc. Rev. 52 (2023) 6554–6585, https://doi.org/10.1039/D3CS00155E.

[18] H. Arwin, M. Poksinski, K. Johansen, Total internal reflection ellipsometry: principles and applications, Appl. Opt. 43 (2004) 3028–3036, https://doi.org/10.1364/AO.43.003028.

[19] A. Nabok, A. Tsargorodskaya, The method of total internal reflection ellipsometry for thin film characterisation and sensing, Thin Solid Films 516 (2008) 8993–9001, https://doi.org/10.1016/J.TSF.2007.11.077.

[20] W.J. Degrip, J. Vanoostrum, P.H.M. Bovee-Geurts, Selective detergent-extraction from mixed detergent/lipid/protein micelles, using cyclodextrin inclusion

compounds: a novel generic approach for the preparation of proteoliposomes, Biochem. J. 330 (1998) 667–674, https://doi.org/10.1042/BJ3300667.
[21] T. Söllradl, F.A. Banville, V. Chabot, M. Canva, M. Grandbois, P.G. Charette, Metal clad waveguide (MCWG) based imaging using a high numerical aperture microscope objective, Opt. Express 25 (2017) 1666–1679, https://doi.org/10.1364/OE.25.001666.
[22] K. Juškevičius, M. Audronis, A. Subačius, S. Kičas, T. Tolenis, R. Buzelis, R. Drazdys, M. Gaspariunas, V. Kovalevskij, A. Matthews, A. Leyland, Fabrication of Nb2O5/SiO2 mixed oxides by reactive magnetron co-sputtering, Thin Solid Films 589 (2015) 95–104, https://doi.org/10.1016/J.TSF.2015.04.075.
[23] A. Belosludtsev, A. Sytchkova, N. Kyžas, I. Bitinaitis, R. Simniškis, R. Drazdys, Ultrathin sputtered silver films protected by ALD alumina: comparison of in-situ investigation with ex-situ resistance and ellipsometric measurements, Vacuum 195 (2022) 110669, https://doi.org/10.1016/J.VACUUM.2021.110669.
[24] D. Jang, G. Chae, S. Shin, Analysis of surface plasmon resonance curves with a novel sigmoid-asymmetric fitting algorithm, Sensors 15 (2015) 25385–25398, https://doi.org/10.3390/S151025385.
[25] I. Thormählen, J. Straub, U. Grigull, Refractive index of water and its dependence on wavelength, temperature, and density, J. Phys. Chem. Ref. Data 14 (1985) 933–945, https://doi.org/10.1063/1.555743.
[26] O. Buchnev, V.A. Fedotov, A. Belosludtsev, Polarization discrimination and surface sensing with a near-IR nanostructured hybrid mirror, Opt. Lett. 47 (2022) 4036–4039, https://doi.org/10.1364/OL.464684.
[27] O. Buchnev, A. Belosludtsev, V. Reshetnyak, D.R. Evans, V.A. Fedotov, Observing and controlling a Tamm plasmon at the interface with a metasurface, Nanophotonics 9 (2020) 897–903, https://doi.org/10.1515/NANOPH-2019-0514.
[28] S.G. Ilchenko, A. Belosludtsev, I. Bitinaitis, V. Panasyuk, V. Taranenko, Fano-resonant filtering by chromium-based multilayer nanostructures, Opt. Lett. 50 (2025) 7019–7022, https://doi.org/10.1364/OL.569973.
[29] F. Mazzotta, T.W. Johnson, A.B. Dahlin, J. Shaver, S.H. Oh, F. Höök, Influence of the evanescent field decay length on the sensitivity of plasmonic nanodisks and nanoholes, ACS Photonics 2 (2015) 256–262, https://doi.org/10.1021/ph500360d.
[30] H. Cai, S. Shan, X. Wang, High sensitivity surface plasmon resonance sensor based on periodic multilayer thin films, Nanomaterials 11 (2021) 3399, https://doi.org/10.3390/NANO11123399.
[31] J. Homola, Surface plasmon resonance sensors for detection of chemical and biological species, Chem. Rev. 108 (2008) 462–493, https://doi.org/10.1021/CR068107D.
[32] Maria Losurdo, Kurt Hingerl. Ellipsometry at the nanoscale, 1st ed., Springer, Berlin, Heidelberg, 2013 https://doi.org/10.1007/978-3-642-33956-1.
[33] M. Piliarik, J. Homola, Surface plasmon resonance (SPR) sensors: approaching their limits? Opt. Express 17 (2009) 16505–16517, https://doi.org/10.1364/OE.17.016505.
[34] S. Isaacs, E. Harté, I.D. Alves, I. Abdulhalim, Improved detection of plasmon waveguide resonance using diverging beam, liquid crystal retarder, and application to lipid orientation determination, Sensors 19 (2019) 1402, https://doi.org/10.3390/S19061402.
[35] X. Dai, S. Wang, Y. Wang, X. Wang, X. Wu, X. Liu, J. Jiang, T. Xu, T. Liu, Dual-resonance optical fiber lossy mode resonance immunoprobe for serum PSA detection, Biosens. Bioelectron. 271 (2025) 117049, https://doi.org/10.1016/J.BIOS.2024.117049.
[36] J. Ryken, J. Li, T. Steylaerts, R. Vos, J. Loo, K. Jans, W. Van Roy, T. Stakenborg, P. Van Dorpe, J. Lammertyn, L. Lagae, Biosensing with SiO2-covered SPR substrates in a commercial SPR-tool, Sens Actuators B Chem. 200 (2014) 167–172, https://doi.org/10.1016/J.SNB.2014.04.060.
[37] Y.B. Shin, H.M. Kim, Y. Jung, B.H. Chung, A new palm-sized surface plasmon resonance (SPR) biosensor based on modulation of a light source by a rotating mirror, Sens. Actuators B Chem. 150 (2010) 1–6, https://doi.org/10.1016/J.SNB.2010.08.006.
[38] S. Zangenehzadeh, E. Agocs, F. Schröder, N. Amroun, R. Biedendieck, D. Jahn, A. Günther, L. Zheng, B. Roth, H.H. Johannes, W. Kowalsky, Polarization modulated spectroscopic ellipsometry-based surface plasmon resonance biosensor for E. coli K12 detection, Sci. Rep. 14 (2024) 1–11, https://doi.org/10.1038/s41598-024-78535-8.
[39] L. Song, Z. Wang, D. Zhou, A. Nand, S. Li, B. Guo, Y. Wang, Z. Cheng, W. Zhou, Z. Zheng, J. Zhu, Waveguide coupled surface plasmon resonance imaging measurement and high-throughput analysis of bio-interaction, Sens. Actuators B Chem. 181 (2013) 652–660, https://doi.org/10.1016/J.SNB.2013.01.096.
[40] D. Wang, F.-C. Loo, H. Cong, W. Lin, S.K. Kong, Y. Yam, S.-C. Chen, H. Ho, Pui, Real-time multi-channel SPR sensing based on DMD-enabled angular interrogation, Opt. Express 26 (2018) 24627–24636, https://doi.org/10.1364/OE.26.024627.
[41] S.Y. Wu, H.P. Ho, W.C. Law, C. Lin, S.K. Kong, Highly sensitive differential phase-sensitive surface plasmon resonance biosensor based on the Mach–Zehnder configuration, Opt. Lett. 29 (2004) 2378–2380, https://doi.org/10.1364/OL.29.002378.
[42] M. Kashif, M.H.H. Mokhtar, N.H. Azeman, F.H. Hashim, N. Arsad, A.A. G. Abushagur, A.A.A. Bakar, Phase-interrogated surface plasmon resonance sensor based on laser feedback interferometry, Opt. Lasers Eng. 141 (2021) 106564, https://doi.org/10.1016/J.OPTLASENG.2021.106564.
[43] Y.H. Huang, H.P. Ho, S.Y. Wu, S.K. Kong, W.W. Wong, P. Shum, Phase sensitive SPR sensor for wide dynamic range detection, Opt. Lett. 36 (2011) 4092–4094, https://doi.org/10.1364/OL.36.004092.
[44] I. Watad, I. Abdulhalim, Phase-shifted polarimetric surface plasmon resonance sensor using a liquid crystal retarder and a diverging beam, Pp. 1607-1610 44, Opt. Lett. 44 (7) (2019) 1607–1610, https://doi.org/10.1364/OL.44.001607.
[45] N. Mandal, S.D. Mayanglambam, R.S. Moirangthem, 3D- printed modular spr platform integrated with ellipsometer for in-situ label-free optical sensing applications, Opt. Lasers Eng. 181 (2024) 108422, https://doi.org/10.1016/J.OPTLASENG.2024.108422.
[46] Y. Shao, Y. Li, D. Gu, K. Zhang, J. Qu, J. He, X. Li, S.-Y. Wu, H.-P. Ho, M.G. Somekh, H. Niu, Wavelength-multiplexing phase-sensitive surface plasmon imaging sensor, Opt. Lett. 38 (2013) 1370–1372, https://doi.org/10.1364/OL.38.001370.
[47] Z. Khajemiri, D. Lee, S.M. Hamidi, D.S. Kim, Rectangular plasmonic interferometer for high sensitive glycerol sensor, Sci. Rep. 9 (2019) 1–7, https://doi.org/10.1038/s41598-018-37499-2.
[48] R.C. Jorgenson, S.S. Yee, A fiber-optic chemical sensor based on surface plasmon resonance, Sens Actuators B Chem. 12 (1993) 213–220, https://doi.org/10.1016/0925-4005(93)80021-3.
[49] G. Brambilla, P. Horak, F. Xu, Optical microfiber coil resonator refractometric sensor, Opt. Express 15 (2007) 7888–7893, https://doi.org/10.1364/OE.15.007888.
[50] G.G. Nenninger, P. Tobiška, J. Homola, S.S. Yee, Long-range surface plasmons for high-resolution surface plasmon resonance sensors, Sens Actuators B Chem. 74 (2001) 145–151, https://doi.org/10.1016/S0925-4005(00)00724-3.
[51] R. Kanok, M. Abuleil, P. Hlubina, I. Abdulhalim, Bloch surface wave fast ellipsometric sensor utilizing a polarization camera with an improved detection limit, Opt. Laser Technol. 179 (2024) 111218, https://doi.org/10.1016/J.OPTLASTEC.2024.111218.
[52] F.C. Chien, C.Y. Lin, J.N. Yih, K.L. Lee, C.W. Chang, P.K. Wei, C.C. Sun, S.J. Chen, Coupled waveguide–surface plasmon resonance biosensor with subwavelength grating, Biosens. Bioelectron. 22 (2007) 2737–2742, https://doi.org/10.1016/J.BIOS.2006.11.021.
[53] X.D. Jiang, W.R. Xu, N. Ilyas, M.C. Li, R.K. Guo, R. khan, W. Li, J.M. Wang, High-Performance coupled plasmon waveguide resonance optical sensor based on SiO2: Ag film, Results Phys. 26 (2021) 104308, https://doi.org/10.1016/J.RINP.2021.104308.
[54] M. Hedhly, Y. Wang, S. Zeng, F. Ouerghi, J. Zhou, G. Humbert, Highly sensitive plasmonic waveguide biosensor based on phase singularity-enhanced goos–hänchen shift, 2022, Vol. 12, Page 457, Biosensors 12 (2022) 457, https://doi.org/10.3390/BIOS12070457.
[55] Y. Wang, S. Zeng, A. Crunteanu, Z. Xie, G. Humbert, L. Ma, Y. Wei, A. Brunel, B. Bessette, J.C. Orlianges, F. Lalloué, O.G. Schmidt, N. Yu, H.P. Ho, Targeted sub-attomole cancer biomarker detection based on phase singularity 2D nanomaterial-enhanced plasmonic biosensor, Nanomicro Lett. 13 (2021) 1–11, https://doi.org/10.1007/S40820-021-00613-7.
[56] X. Yin, L. Hesselink, Goos-Hänchen shift surface plasmon resonance sensor, Appl. Phys. Lett. 89 (2006) 261108, https://doi.org/10.1063/1.2424277.
[57] Z. Salamon, S. Devanathan, I.D. Alves, G. Tollin, Plasmon-waveguide resonance studies of lateral segregation of lipids and proteins into microdomains (Rafts) in solid-supported bilayers, J. Biol. Chem. 280 (2005) 11175–11184, https://doi.org/10.1074/JBC.M411197200.
[58] Z.V. Leonenko, E. Finot, H. Ma, T.E.S. Dahms, D.T. Cramb, Investigation of temperature-induced phase transitions in DOPC and DPPC phospholipid bilayers using temperature-controlled scanning force microscopy, Biophys. J. 86 (2004) 3783–3793, https://doi.org/10.1529/BIOPHYSJ.103.036681.
[59] M.C. Howland, A.W. Szmodis, B. Sanii, A.N. Parikh, Characterization of physical properties of supported phospholipid membranes using imaging ellipsometry at optical wavelengths, Biophys. J. 92 (2007) 1306–1317, https://doi.org/10.1529/BIOPHYSJ.106.097071.
[60] M.M.B. Nielsen, A.C. Simonsen, Imaging ellipsometry of spin-coated membranes: mapping of multilamellar films, hydrated membranes, and fluid domains, Langmuir 29 (2013) 1525–1532, https://doi.org/10.1021/LA3046675.
[61] M. Gavutis, V. Navikas, T. Rakickas, Š. Vaitekonis, R. Valiokas, Lipid dip-pen nanolithography on self-assembled monolayers, J. Micromech. Microeng. 26 (2016) 025016, https://doi.org/10.1088/0960-1317/26/2/025016.
[62] Z. Salamon, G. Tollin, Optical anisotropy in lipid bilayer membranes: coupled plasmon-waveguide resonance measurements of molecular orientation, polarizability, and shape, Biophys. J. 80 (2001) 1557–1567, https://doi.org/10.1016/S0006-3495(01)76128-0.
[63] V. Balhara, R. Schmidt, S.U. Gorr, C. Dewolf, Membrane selectivity and biophysical studies of the antimicrobial peptide GL13K, Biochim. Et. Biophys. Acta (BBA) Biomembr. 1828 (2013) 2193–2203, https://doi.org/10.1016/J.BBAMEM.2013.05.027.

Tomas Rakickas received the Master's degree in Laser Physics and Optical Technologies from Vilnius University, Lithuania. Currently, he is working as a junior researcher at the Center for Physical Sciences and Technology, Lithuania. His current research interests are micro and nano-patterning, biofabrication, self-assembles monolayers and optical biosensors.

Ignas Bitinaitis received his Master degree in Laser Technology at the Vilnius University in 2021. He is currently finishing a PhD studies at the Center for Physical Sciences and Technology (FTMC). His research focuses on thin metal–dielectric films, optical coatings, photonics, lasers and sensors. Professionally, he is involved in the R&D of laser cleaning and welding systems at MB FEMTA, with an emphasis on high-precision applications.

Victor Reshetnyak received his PhD and DSc in theoretical physics from Taras Shevchenko National University of Kyiv (Ukraine) in 1985 and 1994 respectively. He is currently Emeritus Professor at Taras Shevchenko National University of Kyiv, Visiting Professor at the University of Leeds (UK) and Visiting Academic at the University of Warwick (UK). His current research interests include modelling of tunable liquid crystal lenses, liquid crystal elastomers, ferroelectric nematics, temporal metamaterials, surface, spoof and Tamm plasmons.

Dr. Edita Voitechovic received her PhD in biochemistry from Vilnius University (Institute of Biochemistry, Lithuania) in 2013 for the thesis devoted to amperometric biosensors. She has since undertaken several postdoctoral research projects, including at the Institute of Chemistry of Saint Petersburg State University (Russian Federation) and the Institute of Microelectronics of Barcelona (IMB-CNM, CSIC, Spain). Currently she is working as the research scientist at the Department of Nanoengeneering in the Center for Physical Sciences and Technology (Lithuania). Her research interests center on the design and application of electrochemical and optical biosensors for the analysis of complex biological media.

Dr. Alexandr Belosludtsev has finished the Ph.D. in a field "Plasma Physics and Physics of Thin Films" at the University of West Bohemia, Czech Republic. Currently, he is working as a Senior Researcher and magnetron sputtering group leader at the Center for Physical Sciences and Technology, Lithuania. The main topics of interest are thin films, material science, optics, photonics, lasers, sensors.

MAIN RESULTS AND CONCLUSION

1. The growth mechanisms of ultrathin magnetron-sputtered silver films were systematically investigated using complementary in-situ and ex-situ characterization techniques. Broadband Monitoring (BBM) was shown to provide a reliable method for identifying coalescence and continuity formation during deposition, with the percolation threshold occurring at approximately 6 nm and complete film continuity at approximately 12 nm thickness [A].

2. Ellipsometric analysis revealed that the sputtered silver films develop non-uniformly through the film thickness, indicating that percolation begins near the film surface and subsequently propagates toward the substrate interface. These findings improve the understanding of ultrathin metallic film formation and provide guidance for fabrication of plasmonic and resonant optical structures [A].

3. The incorporation of aluminium into silver coatings was shown to reduce surface roughness and improve stability in low earth orbit (LEO) environment while maintaining high optical reflectance in VIS-IR range. Ag–Al coatings containing approximately 5–8% aluminium demonstrated the most favourable combination of optical performance and resistance to proton-induced degradation relevant to space applications [B].

4. A technological route combining selective laser melting, precision polishing, and magnetron sputtering was demonstrated for time efficient fabrication of lightweight actively cooled high-reflective mirrors with reflectivity of >95% in VIS-IR range and arithmetic average roughness of Ra <3–5 nm [C].

5. Planar chromium-based metal–dielectric multilayer structures supporting Fano-type resonances were designed, fabricated, and experimentally characterized. The developed structures exhibited narrow Fano-type resonances with angular width close to 0.5 milliradians and high contrast, demonstrating the potential of chromium-based coatings for advanced optical filtering and sensor applications [D].

6. The combination of plasmon waveguide resonance structures with Total Internal Reflection Ellipsometry (TIRE) demonstrated significantly enhanced optical sensor performance in fixed-angle ellipsometric measurements. The developed multilayer sensor architecture achieved fixed angle of incidence TIRE readout sensitivity improvement to 8.5×10^{-7} RIU, up to four times compared with conventional gold-based surface plasmon resonance sensors, highlighting the potential of magnetron-sputtered metal–dielectric coatings for next-generation optical sensing applications [E].

REFERENCES

1. T.F. Kuech, "4.01 Integration of Dissimilar Materials", Comprehensive Semiconductor Science and Technology, Elsevier, 2011, Pages 1-24, ISBN 9780444531537, https://doi.org/10.1016/B978-0-44-453153-7.00106-1.
2. Brune, H. "Growth modes." Encyclopedia of Materials: Science and Technology, Sect. 1.9, Physical Properties of Thin Films and Artificial Multilayers (2001): 3683-3693.
3. Kiwi, M. and Rössler, J. " The drude model". 2024, Revista Brasileira de Ensino de Física, 46, p.e20240199. https://doi.org/10.1590/1806-9126-RBEF-2024-0199
4. V. G. Karpov, A. D. Compaan, Diana Shvydka; Effects of nonuniformity in thin-film photovoltaics. Appl. Phys. Lett. 3 June 2002; 80 (22): 4256–4258. https://doi.org/10.1063/1.1483118
5. Fujiwara, H., Koh, J., Rovira, P.I. and Collins, R.W. (2000), Assessment of effective-medium theories in the analysis of nucleation and microscopic surface roughness evolution for semiconductor thin films. Physical Review B, 61(16), pp.10832–10844. https://doi.org/10.1103/PhysRevB.61.10832
6. Alvarez, M.M., Khoury, J.T., Schaaff, T.G., Shafigullin, M.N., Vezmar, I. and Whetten, R.L., 1997. Optical absorption spectra of nanocrystal gold molecules. The Journal of Physical Chemistry B, 101(19), pp.3706-3712.
7. Kooyman, R.P., 2008. Physics of surface plasmon resonance

SANTRAUKA

Įvadas

Nuo pirmųjų piešinių urvuose žmonės naudojo plonas grafito dangas pakeisdami paviršiaus atspindimos šviesos savybes. Šiandien grafito bei tauriųjų metalų, ypač sidabro ir chromo dangos yra vienos svarbiausių medžiagų optikoje, elektronikoje ir gamybos įrangoje. Sidabras pasižymi išskirtinėmis optinėmis savybėmis – didžiausiu atspindžiu regimojoje ir artimojoje infraraudonojoje spektro srityse bei palankiomis plazmoninėmis charakteristikomis, todėl yra plačiai naudojamas aukšto atspindžio veidrodžiuose, skaidriuose laidininkuose ir optiniuose jutikliuose. Chromas, dėl savo mechaninio atsparumo, cheminio stabilumo ir optinių savybių, yra svarbi medžiaga apsauginėse dangose, optiniuose filtruose bei sukibimą gerinančiuose tarpsluoksniuose.

Itin plonų metalinių dangų formavimas apima sudėtingus branduoliavimosi, salelių augimo, koalescencijos ir perkoliacijos procesus, kurie lemia galutines optines, elektrines ir mechanines sluoksnių savybes. Šių procesų supratimas ir valdymas reikalauja pažangių tyrimo metodų, leidžiančių realiuoju laiku stebėti dangų augimą ir savybių kitimą.

Šioje disertacijoje ir su ja tiesiogiai susijusiuose moksliniuose straipsniuose nagrinėjami fundamentalūs plonųjų dangų fizikos klausimai ir kartu kuriami praktiniai sprendimai pažangių optinių sistemų kūrimui bei optinių sensorių jautrumo tobulinimui. Tyrimai apima visą technologinę grandinę – nuo plonųjų dangų formavimosi fizikinių procesų ir pažangių charakterizavimo metodų iki sukurtų struktūrų integravimo į modernias taikomąsias sistemas, tokias kaip biosensoriai, optikos komponentai kosmoso komunikacijai ir didelės galios lazerinės sistemas. Sistemingai tiriant magnetroninio dulkinimo procesus, kuriant naujus charakterizavimo metodus ir demonstruojant jų taikymą praktinėse sistemose, šis darbas prisideda tiek prie fundamentalaus plonųjų metalinių dangų supratimo, tiek prie jų technologinės pažangos.

Tyrimų tarpdiscipliniškumas jungia medžiagų mokslą, optinę inžineriją ir pažangias gamybos technologijas, todėl gauti rezultatai yra aktualūs įvairioms sritims – nuo kosminių technologijų ir kvantinės optikos iki biomedicininių jutiklių bei tiksliosios gamybos. Sukurtos metodikos, prototipai ir pademonstruoti taikymai atveria naujas galimybes plonųjų dangų optimizavimui ir jų integravimui į naujos kartos optines sistemas.

Darbe pateikiamos naujos įžvalgos apie aliuminio priemaišų įtaką sidabro dangų stabilumui, plonųjų dangų charakterizavimui pritaikytą efektyviosios terpės aproksimacijos modeliavimą bei naujų chromo pagrindu sukurtų metalo–dielektrinių filtrų kūrimą. Gauti rezultatai leidžia optimizuoti plonųjų dangų medžiagas ir technologinius procesus, tiesiogiai prisidedančius prie naujos kartos optinių sistemų kūrimo, kai būtinas didelis našumas, ilgaamžiškumas ir patikimumas biosensorikos, kosminės optikos bei didelės galios lazerinių sistemų srityse.

DISERTACIJOS TIKSLAS IR UŽDAVINIAI

Disertacijos tikslas

Šio darbo tikslas – ištirti magnetroninio dulkinimo būdu suformuotų plonųjų metalinių sluoksnių fizikines ir optines savybes, jų atspindžio ir pralaidumo charakteristikas priklausomai nuo sluoksnio storio, medžiagos grynumo (legiravimo), optimizuotos daugiasluoksnės struktūros bei pritaikyti gautus rezultatus kosminės optikos, lazerinių sistemų ir biosensorių srityse.

Disertacijos uždaviniai

1. Taikant in-situ ir ex-situ metodus ištirti itin plonų magnetroninio dulkinimo būdu nusodintų sidabro sluoksnių formavimosi etapus bei palyginti šių metodų jautrumą ir atkuriamumą nustatant sidabro sluoksnio augimo fazes.
2. Ištirti aliuminio legiravimo įtaką plonoms sidabro dangoms, vertinant jų optines savybes, paviršiaus morfologiją ir atsparumą jonų sukeltai degradacijai, imituojančiai žemosios žemės orbitos aplinką.
3. Ištirti ir pagerinti selektyviojo lazerinio lydymo būdu pagamintų aktyviai aušinamų veidrodinių struktūrų paviršiaus optinę kokybę, taikant Ag–Al mišrias dangas ir kontroliuojamą poliravimą naudojant skirtingo grūdėtumo abrazyvus.
4. Suprojektuoti, pagaminti ir eksperimentiškai ištirti plokščiąsias chromo pagrindu sudarytas metalo–dielektrines daugiasluoksnes struktūras, pasižyminčias siauru kampiniu ir spektriniu filtravimu dėl Fano tipo rezonansų.

5. Suprojektuoti, pagaminti ir eksperimentiškai ištirti plokščiąsias sidabro pagrindu sudarytas metalo–dielektrines daugiasluoksnes struktūras, skirtas plazmoninio bangolaidžio rezonanso (PWR) ir visiško vidinio atspindžio elipsometrijos (TIRE) jutikliams.

Darbo mokslinis naujumas ir praktinė reikšmė

1. Parodyta, kad augančio sidabro sluoksnio plataus spektro pralaidumo stebėsena (Broadband Monitoring, BBM) leidžia patikimai in-situ nustatyti mažiausią sluoksnio storį, kuriam esant danga tampa tolydi.
2. Nustatyta, kad sidabro sluoksniai su 8 % aliuminio priemaiša pasižymi reikšmingai mažesniu paviršiaus šiurkštumu, išlaikydami gryno sidabro dangoms būdingą aukštą atspindį regimojoje–infraraudonojoje (VIS–IR) spektro srityje.
3. Parodyta, kad selektyviojo lazerinio lydymo, poliravimo ir magnetroninio dulkinimo technologijų derinys leidžia efektyviai gaminti sudėtingos geometrijos aukšto atspindžio metalinius veidrodžius.
4. Pirmą kartą parodyta, kad chromo pagrindu daugiasluoksnėje struktūroje formuojami Fano rezonansai gali būti naudojami kaip platforma pažangiems optiniams filtrams kurti.
5. Pirmą kartą parodyta, kad sidabro pagrindu sudarytos plokščiosios daugiasluoksnės metalo–dielektrinės struktūros palaiko bangolaidines modas galinčias padidinti visiško vidinio atspindžio elipsometrijos (Total Internal Reflection Ellipsometry, TIRE) jautrumą biosensoriniuose taikymuose.

Ginamieji disertacijos teiginiai

1. Optimizuojant skaidraus sidabro sluoksnio storį daugiasluoksnėje dielektrinėje struktūroje galima pasiekti $8{,}5\times10^{-7}$ RIU optinių sensorių jautrumą - iki keturių kartų didesnį už įprastai industrijoje naudojamų aukso dangos biosensorių. Šio sidabro sluoksnio tolygiam nusodinimui ant dielektrinio pagrindo tikslesnis formavimosi procesas gali būti pasiekiamas in-situ optinio stebėjimo būdu, pasirenkant stebimą bangos ilgį esantį arti lokalizuotojo paviršiaus plazmonų rezonanso (LSPR) viršūnės.

2. Didelio atspindžio metaliniai veidrodžiai gali būti efektyviai gaminami selektyviojo lazerinio lydymo būdu suformuojant pagrindo struktūrą, atliekant jo poliravimą ir paviršių padengiant pritaikyta optine danga. Regimosios–infraraudonosios (VIS–IR) šviesos spektro srityje sidabro danga su 8 % aliuminio priemaiša pasižymi optimaliomis savybėmis kosmoso taikymams – didesniu atsparumu 20 keV H^- jonų bombardavimui iki 1,8 × 10^{16} cm^{-2} jonų dozės bei mažesniu paviršiaus šiurkštumu iki R_a = 2,3 nm.

Autoriaus ir bendraautorių indėlis

Didžiąją dalį eksperimentinių dangų nusodinimo darbų, matavimų, gautų rezultatų analizės ir jų aprašymo atliko disertacijos autorius.

Darbo vadovas dr. A. Belosludtsev prisidėjo rengiant eksperimentinių tyrimų planą, optimizuojant dangų nusodinimo procesus, taip pat teikė vertingas pastabas, pasiūlymus ir konsultacijas tyrimų vykdymo bei disertacijos rengimo metu.

Publikacijų bendraautoriai prisidėjo prie mokslinių darbų koncepcijos formavimo, rezultatų aptarimo, publikacijų rengimo ir pateikė vertingų pastabų bei įžvalgų.

SANTRAUKA

Disertacija parengta kaip penkių mokslinių straipsnių rinkinys, publikuotas tarptautiniuose recenzuojamuose mokslo žurnaluose. Straipsniuose apibendrinti pagrindiniai tyrimų rezultatai, kurie buvo atliekami doktorantūros studijų metu nuo 2021 m. rugsėjo mėn.

PUBLIKACIJŲ SĄRAŠAS

Mokslinės publikacijos, ***tiesiogiai susijusios*** *su disertacijos tema:*

A. Alexandr Belosludtsev, Anna Sytchkova, Naglis Kyžas, **Ignas Bitinaitis**, Rimantas Simniškis, Ramutis Drazdys, "Ultrathin sputtered silver films protected by ALD alumina: Comparison of in-situ investigation with ex-situ resistance and ellipsometric measurements", Vacuum, Volume 195, 2022, 110669, ISSN 0042-207X, https://doi.org/10.1016/j.vacuum.2021.110669.

B. Alexandr Belosludtsev, **Ignas Bitinaitis**, Julijanas Želudevičius, Vitalij Kovalevskij, Sabereh T. Rastkar, Anna Sytchkova, "Proton resistance of high reflective silver-aluminium mirrors for space applications", Advances in Space Research, 2026, https://doi.org/10.1016/j.asr.2026.06.103
C. **Ignas Bitinaitis**, Karolis Stravinskas, Sergejus Borodinas, Genrik Mordas, Alexandr Belosludtsev "Reflectivity improvement of lightweight active cooled metal mirrors manufactured by additive manufacturing". Optical Materials, Volume 169, 2026, 117570, ISSN 0925-3467. doi: 10.1016/j.optmat.2025.117570.
D. Svitlana Ilchenko, Alexandr Belosludtsev, **Ignas Bitinaitis**, Volodymyr Panasyuk, Volodymyr Taranenko. "Fano-resonant filtering by planar chromium-based multilayer stacks". Optics Letters, 2025, Vol. 50, 7019–7022. doi: 10.1364/OL.569973
E. Tomas Rakickas, **Ignas Bitinaitis**, Victor Reshetnyak, Edita Voitechovič, Alexandr Belosludtsev "Total internal reflection ellipsometry for multilayer plasmon waveguide resonance sensors", Sensors and Actuators B: Chemical, Volume 452, 2026, 139454, ISSN 0925-4005, doi: 10.1016/j.snb.2026.139454.

REZULTATAI IR IŠVADOS

1. Taikant vienas kitą papildančius *in-situ* ir *ex-situ* charakterizavimo metodus buvo sistemiškai ištirti magnetroninio dulkinimo būdu nusodintų sidabro sluoksnių augimo principai. Parodyta, kad plataus spektro pralaidumo stebėsena yra patikimas metodas koalescencijos ir tolydžios dangos formavimosi etapams nustatyti, o perkoliacijos riba pasiekiama ties maždaug 6 nm storio sluoksniu, kai tuo tarpu tolydi sidabro danga susiformuoja ties maždaug 12 nm sluoksnio storiu [A].

2. Elipsometrinė analizė parodė, kad sidabro sluoksnis ant dielektrinių paviršių pradžioje formuojasi ir auga netolygiai per visą sluoksnio storį – perkoliacija pirmiausia prasideda ties paviršiumi ir tik vėliau plinta link pagrindo. Šie rezultatai pagilina supratimą apie itin plonų metalinių sluoksnių formavimąsi ir suteikia praktinių gairių plazmoninių bei rezonansinių optinių struktūrų kūrimui [A].

3. Nustatyta, kad aliuminio priemaišos sidabro dangose keičia jų mikrostruktūrą, mažina paviršiaus šiurkštumą ir didina atsparumą aplinkos poveikiui, kartu išlaikant aukštą optinį atspindį. Sidabro

dangos legiruotos 5–8 % aliuminio, pasižymėjo geriausiu optinių savybių ir atsparumo susidūrimams su protonais deriniu, svarbiu kosminės paskirties optinėms sistemoms [B].

4. Pademonstruota technologinė grandinė, apjungianti selektyvųjį lazerinį lydymą, tikslų poliravimą ir magnetroninį dulkinimą, skirta efektyviam lengvų aktyviai aušinamų veidrodžių gamybai [C].
5. Suprojektuotos, pagamintos ir eksperimentiškai ištirtos plokščiosios chromo pagrindu sudarytos metalo–dielektrinės daugiasluoksnės struktūros, palaikančios Fano tipo rezonansus. Sukurtose struktūrose stebėti siauri Fano tipo rezonansai, pasižymintys itin siauru 0,5 miliradianų kampiniu pločiu ir aukštu kontrastu, atskleidžiantys chromo pagrindu formuojamų daugiasluoksnių struktūrų potencialą pažangių optinių filtrų ir jutiklių kūrimui [D].
6. Parodyta, kad plazmoninių bangolaidinių rezonansų struktūrų ir visiško vidinio atspindžio elipsometrijos derinys leidžia reikšmingai pagerinti optinių sensorių jautrumą. Fiksuoto kampo, visiškojo vidinio atspindžio elipsometriniams (TIRE) matavimams sukurta daugiasluoksnė jutiklio architektūra užtikrino iki 8.5×10^{-7} RIU, t.y. iki keturių kartų didesnį jautrumą nei įprasti aukso pagrindu veikiantys paviršiaus plazmonų rezonanso jutikliai, taip atskleidžiant magnetroninio dulkinimo būdu formuojamų metalo–dielektrinių dangų potencialą naujos kartos optiniuose jutikliuose [E].

CURRICULUM VITAE

Vardas: Ignas
Pavardė: Bitinaitis
Išsilavinimas:

2015 - 2019 Fizikos bakalauras, Vilniaus universitetas

2019 - 2021 Lazerinių technologijų magistras, Vilniaus universitetas

2021 - 2026 Technologijos mokslų srities doktorantūra, Fizinių ir Technologijos Mokslų Centras, Vilniaus Universitetas

Profesinė patirtis:

2014 - 2022 Lietuvos Jaunimo Sklandymo Rinktinė
Pilotas

2014 - Dabar "Fused Trio"; "Eiktubaiktu"; "DDL PLK"
Muzikinių grupių narys, instrumentalistas.

2016; 2018; 2020 VŠĮ Laikaski.lt
Pilotas, projektų dalyvis

2018 - 2021 MB Optola,
Bendraįkūrėjas, vadovas, projektuotojas, inžinierius

2021 - 2025 Fizinių ir technologijos mokslų centras.
technikas, inžinierius, doktorantas, jaunesnysis mokslo darbuotojas, vyresnysis inžinierius

2021 - Dabar MB Femta
Įkūrėjas, vadovas, projektuotojas, inžinierius

2026 - Dabar	VŠĮ Way Ahead *Įkūrėjas, nekomercinių kūrybinių renginių organizatorius*

Mokslinė veikla:

2018	3-jų mėnesių trukmės stažuotė Department of Solid State Sciences, Ghent University, Belgium, atliekant tyrimus “Atomic Layer Deposition of TiO_2 Thin Films for Lithium-Ion Battery Research"
2021	Mokslinio straipsnio bendraautorius: *Alexandr Belosludtsev, Ignas Bitinaitis, Kazimieras Baltrušaitis, Aleksej M. Rodin, "Investigation of the laser cleaning process for IBS grids in optical coating technology". Int J Adv Manuf Technol 114, 2863–2869 (2021). https://doi.org/10.1007/s00170-021-07035-0*
2022	Mokslinio straipsnio bendraautorius: *Alexandr Belosludtsev, Anna Sytchkova, Naglis Kyžas, Ignas Bitinaitis, Rimantas Simniškis, Ramutis Drazdys, "Ultrathin sputtered silver films protected by ALD alumina: Comparison of in-situ investigation with ex-situ resistance and ellipsometric measurements", Vacuum, Volume 195, 2022, 110669, ISSN 0042-207X, https://doi.org/10.1016/j.vacuum.2021.110669.*
2023 - 2024	4,56 mėnesių trukmės stažuotė tarptautiniame H2020-MSCA-RISE-2017 (Marie Skłodowska-Curie Research and Innovation Staff Exchange, Grant agreement No. 778308) projekte SPINMULTIFILM, atliekant Sr_2FeMoO_6 dangos tyrimus. *Rezultatai pristatyti ir publikuoti DOI: 10.1117/12.3029571 Projekto puslapis: http://spinmultifilm.myscispot.eu/project/*

2025 Mokslinio straipsnio bendraautorius:
Svitlana Ilchenko, Alexandr Belosludtsev, Ignas Bitinaitis, Volodymyr Panasyuk, Volodymyr Taranenko. "Fano-resonant filtering by planar chromium-based multilayer stacks". Optics Letters, 2025, Vol. 50, 7019–7022. doi: 10.1364/OL.569973

2026 Mokslinio straipsnio bendraautorius:
Ignas Bitinaitis, Karolis Stravinskas, Sergejus Borodinas, Genrik Mordas, Alexandr Belosludtsev "Reflectivity improvement of lightweight active cooled metal mirrors manufactured by additive manufacturing". Optical Materials, Volume 169, 2026, 117570, ISSN 0925-3467. doi: 10.1016/j.optmat.2025.117570.

2026 Mokslinio straipsnio bendraautorius:
Tomas Rakickas, Ignas Bitinaitis, Victor Reshetnyak, Edita Voitechovič, Alexandr Belosludtsev "Total internal reflection ellipsometry for multilayer plasmon waveguide resonance sensors", Sensors and Actuators B: Chemical, Volume 452, 2026, 139454, ISSN 0925-4005, doi: 10.1016/j.snb.2026.139454.

2026 Mokslinio straipsnio bendraautorius:
Alexandr Belosludtsev, Ignas Bitinaitis, Julijanas Želudevičius, Vitalij Kovalevskij, Sabereh T. Rastkar, Anna Sytchkova, "Proton resistance of high reflective silver-aluminium mirrors for space applications", Advances in Space Research, 2026, https://doi.org/10.1016/j.asr.2026.06.103

Kūrybinė veikla:

2017 DDL PLK - Super Turbo Underground (Remastered)
Albumo UPC: 4772220002190

2020 Dokumentinis filmas „Pakilau skrydžiui"
projekte „Sklandytuvais nuo jūros iki jūros: Lietuva – Ukraina"
https://epika.lrt.lt/dokumentiniai-filmai,266/pakilau-skrydziui,641320

2021 Fused Trio - Cotton Curd Candy
Albumo UPC: 4772145016364

2021 DDL PLK - Prerijų šuo
Albumo UPC: 4772145017934

2023 DDL PLK - Tau
Albumo UPC: 4772220002190

2024 Eiktubaiktu - Solitary
Albumo UPC: 4772220017002

2024 Eiktubaiktu - Industria
Albumo UPC: 4772220023836

2025 Dokumentinis filmas „Sklandytuvais per Europą: Lietuva – Portugalija"
https://epika.lrt.lt/dokumentiniai-filmai,266/sklandytuvais-per-europa-lietuva--portugalija,926702

2025 Eiktubaiktu - For Fox's Sake
Albumo UPC: 4772220033538

PADĖKA

Pirmiausia noriu padėkoti savo seneliui Vincui Bitinaičiui už palaikymą ir patarimus renkantis studijų kryptį ir mokslo etapus. Taip pat šeimai ir artimiems giminaičiams už nenutrūkstantį palaikymą.

Norėčiau padėkoti ir visiems mokytojams, dėstytojams bei kolegoms, mokiusiems mokykloje, universitete ir bendrai gyvenime. Kiekvienas iš Jūsų prisidėjote prie šios disertacijos savo išminties dalimi.

Ypač norėčiau padėkoti moksliniam vadovui dr. Alexandr Belosludtsev už vertingas pastabas, palaikymą ir idėjas. Taip pat esu labai dėkingas kitiems optinių dangų laboratorijos darbuotojams: laboratorijos vadovei dr. Linai Grinevičiūtei, dr. Lukui Ramaliui, dr. Giedriui Abromavičiui, dr. Simui Melnikui, Linai Volosevičienei ir visiems kitiems nepaminėtiems esamiems ir buvusiems kolegoms.

Taip pat dėkoju visiems publikacijų ir pranešimų konferencijose bendraautoriams, prisidėjusiems prie disertacijoje aprašytų mokslinių tyrimų.

UŽRAŠAMS

Vilnius University Press
9 Saulėtekio Ave., Building III, LT-10222 Vilnius
Email: info@leidykla.vu.lt, www.leidykla.vu.lt
bookshop.vu.lt, journals.vu.lt
Print run copies 10